

國立交通大學

電子工程學系 電子研究所碩士班

碩士論文

利用大氣電漿技術沉積不同結晶性硒薄膜於堆疊金屬

前驅層之硒化製程研究

The Investigation on the Selenization of Various
Crystallinity Selenium Films Deposited by APPECVD
on Stacked Metal Precursor

研究生：吳致緯

指導教授：張國明 博士

中華民國一〇一年七月

利用大氣電漿技術沉積不同結晶性硒薄膜於堆疊金屬
前驅層之硒化製程研究

The Investigation on the Selenization of Various
Crystallinity Selenium Films Deposited by APPECVD
on Stacked Metal Precursor

研究生：吳致緯

Student：Chi-Wei Wu

指導教授：張國明 博士

Advisor：Dr. Kow-Ming Chang



Submitted to Department of Electronics Engineering and Institute of
Electronics College of Electrical and Computer Engineering
National Chiao Tung University
in Partial Fulfillment of the Requirements
for the Degree of Master
in
Electronics Engineering
July 2012
Hsinchu, Taiwan

中華民國一〇一年七月

利用大氣電漿技術沉積不同結晶性硒薄膜於堆疊金屬前驅層之硒化製程研究

學生:吳致緯

指導教授:張國明 博士

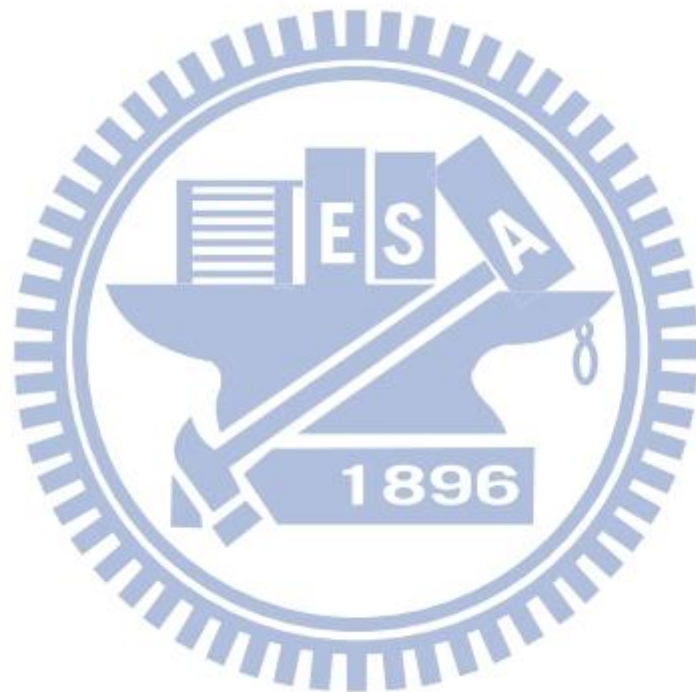
國立交通大學電子工程學系

電子研究所碩士班

摘要

本論文利用大氣電漿輔助化學氣相沉積法去成長硒膜於銅銦鎳前驅層上，大氣電漿輔助化學氣相沉積是屬於非真空系統，且有似濺鍍技術的大面積鍍膜能力，硒的原料利用率相較於共蒸鍍系統有較好的表現。另外在本篇論文中利用快速高溫處理製程進行硒化，將原來硒/銦/銅鎳的前驅層化合成黃銅礦結構的銅銦鎳硒薄膜，其優點為製程快速且可減少 In_2Se 之損耗。我們將研究不同的電漿瓦數和基板溫度對硒膜表面形貌、粗糙度、結構、元素組成的影響，分為退火前和退火後兩階段探討。我們預期利用硒的激發態增加銅銦鎳硒薄膜黃銅礦結構的結晶性，進而改善銅銦鎳硒太陽能電池的效率。接著我們將完成太陽能電池，其結構為鋁電極/氧化銦錫/氧化鋅/硫化鎘/銅銦鎳硒/鈾背電極/鈉鹼玻璃，元件面積為 0.48 平方公分利用並 I-V 曲線量測系統、太陽光模擬系統和外部量子效應量測元件電性。量測結果為基板未加溫下，沒加電漿的元件其轉換效率為 4.694%，有加電漿的元件最高轉換效率為 5.031%；加電漿 50W 情況下，基板未加溫轉換效率為 2.266%，基板溫度為 125°C 之元件轉換效率為 6.103%，此元件填充因子為 0.428、開路電壓 0.41V、短路電流 34.815 mA/cm²。

我們的研究成功利用大氣電漿輔助化學氣相沉積法沉積不同結晶性之硒膜於金屬前驅物並熱退火後形成銅銦鎵硒薄膜，最後製成太陽能電池。電漿的效應為提升銅銦鎵硒薄膜的結晶性，基板溫度則提高銅銦鎵硒薄膜的能隙，進而改善元件的效率，且降低成本。



The Investigation on the Selenization of Various Crystallinity Selenium Films Deposited by APPECVD on Stacked Metal Precursor

Student : Chi-Wei Wu

Advisor : Dr. Kow-Ming Chang

Department of Electronics Engineering and Institute of
Electronics National Chiao Tung University, Hsinchu, Taiwan

Abstract

In this paper, we used the APPECVD system to deposit the selenium films on the Mo/SLG substrate. The APPECVD is a non-vacuum system and has the similar ability of large area of sputtering. And it has smaller amount of Se material which can be used than co-evaporation system does.

In this work, we presented the RTP process as selenization process, which can decrease depletion of In_2Se and is able to accelerate fabrication. We investigated the plasma power and substrate temperature for affecting surface morphology, roughness, structure and composition during the time before and after selenization. We were expecting the degree of crystalline chalcopyrite structure of CIGS films could be improved by radical Se and then so is conversion efficiency of device. Afterwards, we completed solar cell, and its structure is composed by Al/ITO/ZnO/CdS/CIGS/Mo/SLG, which area is 0.48 cm^2 . The electric

properties of CIGS solar cell were measured by I-V curve measurement system with Solar Spectral Irradiance: AM1.5G and extra quantum efficiency. The highest conversion efficiencies of solar cell device without plasma and with plasma are respectively 4.694% and 5.031% at the substrate temperature is 45°C. The conversion efficiency of solar cell device with plasma while power is 50W is 2.266% at the substrate temperature is 45°C. The conversion efficiency of solar cell device with plasma while power is 50W is 6.103% at the substrate temperature is 125°C, which FF=0.428, V_{oc} =0.41V and J_{sc} =34.815 mA/cm². In our final study, we completed to deposit selenium thin films of different crystallization on stacked metal precursor and form chalcopyrite structure of Cu(In,Ga)Se₂ thin films. Consequently, Cu(In,Ga)Se₂ thin films enabled us to fabricate the solar cell device. The effect of plasma enhances the crystallization of chalcopyrite structure of Cu(In,Ga)Se₂ thin films. The effect of substrate temperature raised the band gap of Cu(In,Ga)Se₂ thin films. According to the above-mentioned, those two effects can improve the conversion efficiency of solar cell device and reduce the costs by APPECVD.

誌謝

於本人碩士求學時間中，我首先要感謝指導老師張國明教授，讓我在研究和平常的做人處世上都獲益良多。除此之外，感謝鄧一中教授、吳建宏教授及張加強經理在口試中，對我的論文研究有進一步的探討和指教，讓我的想法可以更加廣泛。

其次感謝實驗室學長們的熱心指導，尤其是何柏慶、黃菘宏、張庭嘉、劉育成學長，在我的研究上提供了許多寶貴的意見，讓我可以順利的進行自己的實驗研究。另外也要感謝工業技術研究院(ITRI)、國家奈米元件實驗室(NDL)與國立交通大學奈米中心(NFC)提供良好的研究機台和實驗環境，讓我們能心無旁騖的做好自己的實驗；且也要感謝林哲蔚先生、張智翔先生、何惟梅小姐、吳宗達先生、姚潔宜小姐和沈奕伶小姐等人的協助下，讓我可以順利的進行並完成實驗的研究。

接著，我要感謝實驗室的同學黃柏文在我研究有問題的時候可以一起討論，並且提供適切的意見來幫助我，還有同組的學弟吳誌恩，盡他所能幫助之力幫助我，才得以完成此論文。

最後，我要特別感謝家人對我的幫助和支持，讓我可以順利的完成碩士學位。

Contents

Abstract (Chinese)	i
Abstract (English)	iii
Acknowledgement	vi
Table Captions	vi
Figure Captions	vii
Chapter 1 Introduction	1
1.1 Forward	1
1.2 Solar Cell	3
1.3 Cu(In,Ga)Se ₂ Films.....	7
1.4 Growth Methods of Cu(In,Ga)Se ₂ Films	10
1.5 Motivation.....	11
Chapter 2 Literature Reviews	21
2.1 The Material Properties of Selenium	21
2.2 The Effect of Plasma Selenium.....	22
2.3 Prepared to Cu(In,Ga)Se ₂ Absorber Layer	24
2.4 Atmospheric Pressure Plasma System	29
Chapter 3 Experiments	40
3.1 Experimental Procedures	40
3.2 Experimental Equipment and Parameters	43
3.3 Characterization Analysis and Measurement Equipment	45
Chapter 4 Result and Discussion	56
4.1 Optimize the Fabrication Parameters	57
4.2 Investigation of Selenium Films on CIG layer Before Selenization.....	59
4.3 Investigation of Cu(In,Ga)Se ₂ Films After Selenization	62
Chapter 5 Conclusions	93
Chapter 6 Future works	95
References	96

Table Captions

Table 1-1 Selected Properties of CuInSe_2	20
Table 1-2 The Most Important Intrinsic Defects for Device-Quality CuInSe_2	20
Table 2-1 The Properties of Selenium.	37
Table 2-2 Amorphous and Crystalline Selenium.....	38
Table 2-3 Density of Charge Species in the Plasma Discharge.....	39
Table 3-1 Optimize the Fabrication Parameters for APPECVD.	55
Table 3-2 Parameters of Selenium Film by APPECVD.	55
Table 4-1 Deposition selenium films on the glass without plasma prepared with different Se source temperature (0W 10SLM 550torr).	86
Table 4-2 Deposition selenium films on the glass without plasma prepared with different main gas flow rate (0W 335°C 550torr).	86
Table 4-3 Deposition selenium films on the glass without plasma prepared with different background pressure (0W 335°C 10SLM).	87
Table 4-4 Deposition selenium films on the glass with plasma prepared with different Se source temperature (50W 20SLM 150torr).	87
Table 4-5 Deposition selenium films on the glass with plasma prepared with different main gas flow rate (50W 355°C 150torr).	88
Table 4-6 Deposition selenium films on the glass without plasma prepared with different background pressure (50W 355°C 10SLM).	88
Table 4-7 Deposition selenium films on the glass without plasma prepared with different plasma power (355°C 10SLM 150torr).	89
Table 4-8 Thickness and RMS roughness of deposited selenium on the CIG precursor layer by APPECVD prepared with different plasma power.....	89

Table 4-9 Thickness and RMS roughness of deposited selenium on the CIG precursor layer by APPECVD prepared with different substrate temperature.....	90
Table 4-10 Thickness of CIGS/MoSe ₂ /Mo/Glass sample and RMS roughness of CIGS thin films prepared with different plasma power.	90
Table 4-11 EDS results for atomic composition of the selenium thin films prepared with different plasma power.....	91
Table 4-12 Thickness of CIGS/MoSe ₂ /Mo/Glass sample and RMS roughness of CIGS films prepared with different substrate temperature.....	91
Table 4-13 EDS results for atomic composition of the selenium thin films prepared with different substrate temperature. III : elements of group III.	92
Table 4-14 Photovoltaic characteristics of CIGS-based solar cells including six devices fabricated with varied plasma power and substrate temperature. V_{oc} : open-circuit voltage, J_{sc} : short-circuit current, FF: fill factor, R_{shunt} : shunt resistance and R_{series} : series resistance.....	92

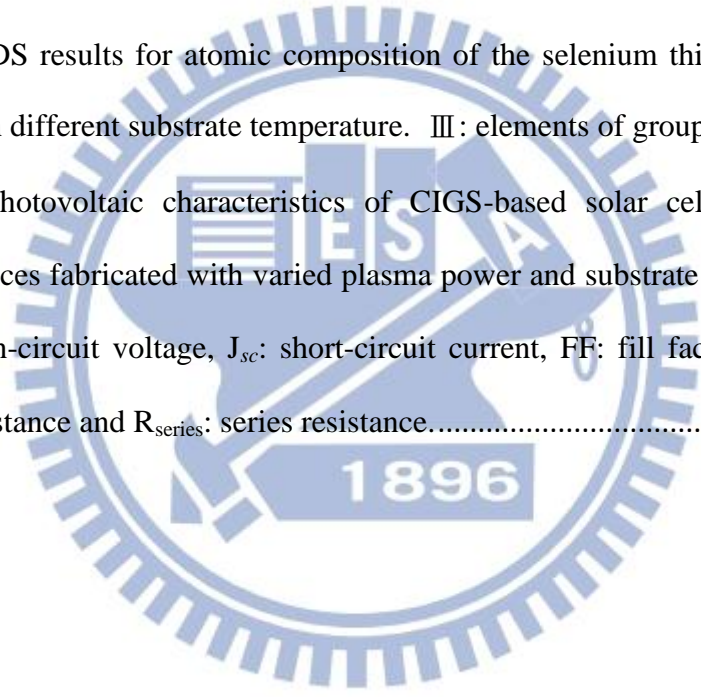


Figure Captions

Figure 1-1 Major PV country markets (GigaWatts).	14
Figure 1-2 Energy Band Diagram of a P-N Junction under Illumination.....	14
Figure 1-3 I-V Characteristics under Dark and Illumination.....	15
Figure 1-4 Inverted I-V Curve Showing Maximum Power Rectangle.	15
Figure 1-5 Shockley-Queisser Limits.	16
Figure 1-6 Absorption Coefficient versus Wavelength of Incident Light.	16
Figure 1-7 The Unit Cell of the Chalcopyrite Lattice Structure.	17
Figure 1-8 Ternary Phase Diagram of the Cu–In–Se System.....	17
Figure 1-9 Pseudobinary Cut $\text{Cu}_2\text{Se-In}_2\text{Se}_3$ of Ternary Phase Diagram.....	18
Figure 1-10 Vacuum Processes for Cu(In,Ga)Se_2	18
Figure 1-11 Non-Vacuum Processes for Cu(In,Ga)Se_2	19
Figure 1-12 Dielectric-Barrier Discharge Linear Plasma Source.....	19
Figure 2-1 Schematic Diagram of Co-evaporation System.	33
Figure 2-2 Schematic Diagram of RF Sputtering System.	33
Figure 2-3 Schematic Diagram of Electro-Deposition System.....	34
Figure 2-4 Schematic Illustration of the Arc Plasma.	34
Figure 2-5 Schematic Illustration of the AP Plasma Jet structures.	35
Figure 2-6 Schematic the Principle of Corona Discharge.....	35
Figure 2-7 Schematic the Principle of Dielectric Barrier Discharge.	36
Figure 3-1 Schematic Illustration of Optimize the Fabrication Parameters.	40
Figure 3-2 Schematic Illustration of Investigation	41
Figure 3-3 Schematic Illustration of Investigation of Device Characterization.	42
Figure 3-4 Schematic Illustration of Se Film Prepared with APPECVD.	51
Figure 3-5 Schematic Illustration of Movable Mechanism of APPECVD.....	51

Figure 3-6 The Temperature Curve of RTP Process.	52
Figure 3-7 Schematic Illustration of SEM Instrument.....	52
Figure 3-8 Schematic Illustration of AFM instrument.	53
Figure 3-9 Schematic Illustration of XRD Instrument.	53
Figure 3-10 Schematic Illustration of PL Instrument.	54
Figure 3-12 Schematic Illustration of EQE Instrument.	54
Figure 4-1 SEM cross-section images of deposited In/Cu ₃ Ga film on the Mo/SLG by sputtering.....	68
Figure 4-2 GIXRD spectrum of deposited In/Cu ₃ Ga on the Mo/SLG by sputtering..	68
Figure 4-3 SEM top-view images of deposited selenium on the CIG precursor layer by APPECVD prepared with different plasma power (a) without plasma (b) 50W (c) 60W (d) 70W.....	69
Figure 4-4 AFM images of deposited selenium on the CIG precursor layer by APPECVD prepared with different plasma power (a) without plasma (b) 50W (c) 60W (d) 70W.	70
Figure 4-5 GIXRD spectrum of deposited selenium on the CIG precursor layer by APPECVD prepared with different plasma power (a) without plasma (b) 50W (c) 60W (d) 70W.	71
Figure 4-6 SEM top-view images of selenium film of different substrate temperatures (a) 45°C (b) 85°C (c) 125°C.	71
Figure 4-7 AFM images of deposited selenium on the CIG precursor layer by APPECVD prepared with different substrate temperature (a) 45°C (b) 85°C (c) 125°C.....	72
Figure 4-8 GIXRD spectrum of deposited selenium on the CIG precursor layer by APPECVD prepared with different substrate temperature (a) 45°C (b)	

85°C (c) 125°C.....	73
Figure 4-9 SEM cross-section images of CIGS thin films prepared with different plasma power (a) without plasma (b) 50W (c) 60W (d) 70W.....	74
Figure 4-10 SEM top-view images of CIGS thin films prepared with different plasma power (a) without plasma (b) 50W (c) 60W (d) 70W. (The part of right half was 10K magnification images; the part of left half was 30K magnification images).....	75
Figure 4-11 AFM images of CIGS thin films prepared with different plasma power (a) without plasma (b) 50W (c) 60W (d) 70W.....	76
Figure 4-12 GIXRD spectrum of CIGS thin films prepared with different plasma power (a) without plasma (b) 50W (c) 60W (d) 70W.....	77
Figure 4-13 Variation of the peak position (2θ) for (112) peak of CIGS thin films with different plasma power.....	77
Figure 4-14 Variation of the FWHM for (112) peak of CIGS thin films with different plasma power.....	78
Figure 4-15 SEM cross-section images of CIGS thin films prepared with different substrate temperature (a) 45°C (b) 85°C (c) 125°C.....	78
Figure 4-16 SEM top-view images of CIGS thin films prepared with different substrate temperature (a) 45°C (b) 85°C (c) 125°C. (The part of right half was 10K magnification images; the part of left half was 30K magnification images).....	79
Figure 4-17 AFM images of CIGS thin films prepared with different substrate temperature (a) 45°C (b) 85°C (c) 125°C.....	80
Figure 4-18 GIXRD spectrum of CIGS thin films prepared with different substrate temperature (a) 45°C (b) 85°C (c) 125°C.....	81

Figure 4-19 Variation of the peak position (2θ) for (112) peak of CIGS thin films with different substrate temperature.....	81
Figure 4-20 Variation of the FWHM for (112) peak of CIGS thin films with different substrate temperature.	82
Figure 4-21 Depth analysis of Auger Electron Spectroscopy (AES) prepared with different substrate temperature (a) 45°C (b) 85°C (c) 125°C.....	83
Figure 4-22 I-V curve measurement of the Cu(In,Ga)Se ₂ solar cells on the AM1.5G solar simulator prepared with different plasma power (a) without plasma (b) 50W (c) 60W (d) 70W.....	84
Figure 4-23 Extra quantum efficiency measurement of the Cu(In,Ga)Se ₂ solar cells prepared with different plasma power (a) without plasma (b) 50W (c) 60W (d) 70W.....	84
Figure 4-24 I-V curve measurement of the Cu(In,Ga)Se ₂ solar cells on the AM1.5G solar simulator prepared with different substrate temperature (a) 45°C (b) 85°C (c) 125°C.....	85
Figure 4-25 Extra quantum efficiency measurement of the Cu(In,Ga)Se ₂ solar cells prepared with different substrate temperature (a) 45°C (b) 85°C (c) 125°C.....	85

Chapter 1

Introduction

1.1 Forward

Fossil fuels have been used as a fuel source for hundreds of years. Fossil fuels were also used to make a wide variety of products including plastic which, like the automobile, has become a key component of modern society. It estimated human-produced energy came from burning fossil fuels was 86% in 2004. The burning of fossil fuels produces around 6.3 billion metric tonnes per year of carbon dioxide (CO₂), a greenhouse gas. It is estimated that natural processes of the Earth can only absorb about half of that amount, resulting in a net increase of 3.2 billion tonnes of atmospheric carbon dioxide per year which many scientists believe leads to global warming. In addition, we consume more and more each year, and many scientists warned about the possibility of running out of fossil fuels. It was important for many countries in the world to develop alternative energy and especially solar cell was the most potential. Solar power is the way which is reproducible environmental protection for electrical energy generator. Besides, it could not produce greenhouse gas in the procedure of electrical energy generator without environmental contamination. And solar energy is silent, unlike noisy generators that are the standard in most homes and businesses, and the lack of moving parts provides an almost maintenance free system. So the advantages of using solar power are numerous. According to Lux Research Industry/Market

Research estimated the percentage higher than 10%, which is solar power in the power supply of the world. Moreover, Global deployment of solar photo-voltaic increased by 40% in 2011, with 27.5 GW of projects installed in 12 months, according to a new report from NPD Solarbuzz as show in Figure 1-1. Last year's strong installation figures prove how quickly the technology can be deployed compared to large, centralized forms of generation.

The development of the solar cell stems from the work of the French physicist Antoine-César Becquerel in 1839. Becquerel discovered the photovoltaic effect while experimenting with a solid electrode in an electrolyte solution; he observed that voltage developed when light fell upon the electrode. About 50 years later, Charles Fritts constructed the first true solar cells using junctions formed by coating the semiconductor selenium with an ultrathin, nearly transparent layer of gold. The energy-conversion efficiencies of Fritts's devices were less than 1%. These early solar cells, however, still had energy-conversion efficiencies of less than 1%. In 1954, three other American researchers, GL Pearson, Daryl Chapin, and Calvin Fuller, demonstrated a silicon solar cell capable of 6-percent energy-conversion efficiency when used in direct sunlight. Until 1970, the silicon solar cell was employed to generate electricity in the earth, which was the mature technology so far.

1.2 Solar Cell

1.2.1 Theory of Solar Cell

A solar cell is a device used to convert solar energy into electricity. In its simplest form, a solar cell is basically a p-n junction diode which is in turn formed by bringing a n-type semiconductor in contact with a p-type semiconductor. Contacts that can be either transparent or metallic are made to the semiconductors. Thus a solar cell is essentially a four layer device on a suitable substrate. When a semiconductor absorbs light with energy greater than its band-gap, electron-hole pairs are generated. The excess electron-hole pairs generated by the absorption of light are swept by the electric field present in the depletion region. The excess electron-hole pairs would recombine with defect in the depletion region. So the current of solar cell was directly proportional to the carrier lifetimes. In order to achieve high carrier lifetimes, the absorber needs to have low defect densities as well as moderate doping. Higher doping in the bulk results in the reduction of carrier lifetime through recombination. On the other hand, the electric field in the depletion region is directly proportional to the doping concentration. So an optimum value of doping had to be chosen to achieve high enough electric fields with sufficient carrier lifetimes.

This process was shown in Figure 1-2 which shows the energy diagram of a solar cell under illumination. E_c and E_v were the band conduction and valence band edges respectively and ϕ_0 is the built-in potential in the dark. The dotted lines represent the respective positions under illumination. The photo-generated excess charge produced a

voltage across the external circuit. This voltage is termed as the open circuit voltage of the solar cell.

1.2.2 Current-Voltage Characteristics of Solar Cell

The current-voltage characteristics of solar cell were shown in Figure 1-3. In this figure had two curves which were dark and under illumination. Since the solar cell was a P-N junction diode, its behavior in the dark was governed by the diode equation.

$$I = I_0 \left(e^{\frac{qV}{nKT}} - 1 \right) \quad (1-1)$$

The total current of a solar cell under illumination was given by

$$I = I_0 \left(e^{\frac{qV}{nKT}} - 1 \right) - I_L \quad (1-2)$$

, where I was the total current, I_0 was the reverse saturation current and I_L was the light generated current. Short circuit current I_{sc} was defined as the current flowing in the circuit when the load was shorted. The voltage developed by a solar cell with an infinite load, it call the open circuit voltage V_{oc} . The function of V_{oc} relative to I_{sc} and I_0 can be represented by

$$V_{oc} = \frac{nKT}{q} \left(\ln \left(1 + \frac{I_{sc}}{I_0} \right) \right) \quad (1-3)$$

, where K is the Boltzmann's constant, n is the diode quality factor and T is the absolute temperature. n and I_0 can be obtained from dark I-V curves. The reciprocal of the slope of the $\ln(I)$ vs V curve gives the value of A and the y intercept gives J_0 . The value of n usually lies between 1 and 2. The highest values of V_{oc} are obtained when I_0 is small. This normally corresponds to a value of 1 for n . The V_{oc} cannot be increased by

increasing n as an increase in n leads to an increase in I_0 thus V_{oc} decreasing. In fact, the popular I-V curve was an inverted I-V curve of a solar cell in the 4-th quadrant, which showed in the Figure 1-4. The maximum power rectangular was show in the Figure 1-4. The I-V curve had a maximum power point (P_m), which was the product of voltage V_m and I_m . The fill factor (FF) of the I-V curve was defined by

$$FF = \frac{V_m * I_m}{V_{oc} * I_{sc}} \quad (1-4)$$

The photovoltaic conversion efficiency is defined as a measure of amount of light energy that was converted into electrical energy and was given by

$$\eta = \frac{P_m}{P_{in}} = \frac{FF * V_{oc} * I_{sc}}{P_{in}} \quad (1-5)$$

, where P_m was the area of maximum power rectangle and P_{in} was the incident light power.

1.2.3 Material of Solar Cell

Different materials display different efficiencies and have different costs. Materials for efficient solar cells must have characteristics matched to the spectrum of available light. Some cells are designed to efficiently convert wavelengths of solar light that reach the Earth surface. However, some solar cells are optimized for light absorption beyond Earth's atmosphere as well. Light absorbing materials can often be used in multiple physical configurations to take advantage of different light absorption and charge separation mechanisms. Different materials of solar cell absorber had the different limit of photovoltaic conversion efficiency. Because of the Shockley-Queisser limit for the theoretical

maximum efficiency of a solar cell, which show in the Figure 1-5 [1]. According to the Figure 1-6, the different material of solar cell had different absorption coefficient versus wavelength of incident light. Materials of solar cell represented respectively three categories, which was Crystalline Silicon solar cell, Thin-Film solar cell and Organic solar cell.

The technology of crystalline silicon solar cells more mature and photovoltaic conversion efficiency higher than other categories of solar cell. But the material cost of silicon solar cells was also high, as silicon was an indirect band-gap semiconductor and hence a large thickness was needed to efficiently absorb the incident sunlight. Since the thickness of the cell was larger, higher material purity was required to ensure the collection of the generated carriers and avoid recombination process [2]. This had led the silicon to exchange other category materials which are cost effective.

Thin film semiconductors based PV technology should have lower costs, as the material cost is significantly reduced, as the films are only a few microns thick. Large area coatings were also possible at high throughput and low costs. Cells can also be fabricated on low cost substrates or on flexible, light-weight substrates depending on the application. In addition, thin films compound semiconductors also support a wide variety of inexpensive processing techniques like evaporation, sputtering, electro-deposition, CVD and CSS to name a few [3]. Thus the cost of thin films solar cells was reduced further in relation to crystalline silicon solar cells. The major problem associated with the thin film technology was that their conversion efficiencies were lower as compared to crystalline silicon. Thin film semiconductors were generally polycrystalline in nature. This means that grain boundaries are inherent in

these materials lead to increase recombination rates of the generated carriers leading to lower efficiencies. Adhesion of films to the substrate, thickness variations, defects and module stability were the other issues of concern in regard to the thin film solar cells. The most promising thin film technologies were those based on amorphous silicon (a-Si), Cadmium Telluride (CdTe) and Copper Indium Gallium Selenide (CIGS). Laboratory area cells have shown efficiencies greater than 18% for Cu(In,Ga)Se₂ [4][5] and 16% for CdTe [6]. However, the presence of Cd in both these technologies and the presence of Se in CIGS is a source of concern.

Organic solar cells are a relatively novel technology, yet hold the promise of a substantial price reduction (over thin-film silicon) and a faster return on investment. These cells can be processed from solution, hence the possibility of a simple roll-to-roll printing process, leading to inexpensive, large scale production. Energy conversion efficiencies achieved to date using conductive polymers are low compared to inorganic materials. However, it has improved quickly in the last few years and the highest NREL (National Renewable Energy Laboratory) certified efficiency has reached 8.3% for the Konarka Power Plastic [7]. In addition, these cells could be beneficial for some applications where mechanical flexibility and disposability are important.

1.3 Cu(In,Ga)Se₂ Films

In this essay, we choose the Cu(In,Ga)Se₂ to be absorber layer material of the solar cell. Because of the chalcopyrite CIGS compound

was a direct band-gap material and had absorption coefficient higher than 10^5 cm^{-1} . The CIGS absorber layer had many intrinsic material properties, which was tunable band-gap and thermal and chemical stability, lead CIGS to be one of the most promising absorber materials for thin film solar cells. The best CIGS thin film solar cell had reached a confirmed conversion efficiency of about 20% [8] Soda lime glass replaced ceramic or borosilicate glass substrates. Initially, this change was made for the lower costs of the soda lime glass and its good thermal expansion match to CuInSe_2 . However, it soon became clear that an increase in device performance and processing tolerance resulted primarily from the beneficial in-diffusion of sodium from the glass.

1.3.1 Material Properties

The crystal structure of CIS/CIGS is a tetragonal chalcopyrite structure [9]. This is a diamond-like structure similar to sphalerite structure but with an ordered substitution of the group I (Cu) and group III (In or Ga) elements on the group II (Zn) sites of sphalerite. This gives a tetragonal unit cell depicted in Figure 1-7 with a ratio of the tetragonal lattice parameters c/a close to 2 (see Table 1-1). The deviation from $c/a = 2$ is called the tetragonal distortion and stems from different strengths of the Cu–Se and the In–Se or Ga–Se bonds. The performance of CuInSe_2 solar cells is limited by a comparatively lower V_{oc} due to its small band-gap. And then CuInSe_2 can be alloyed in any proportion with CuGaSe_2 , thus forming Cu(In,Ga)Se_2 . Therefore, the band-gap of CIGS is continuously adjustable from 1.01eV for pure CuInSe_2 to 1.68eV for pure

CuGaSe₂ for the purpose of increasing the V_{oc}. The band gap for the composition Cu(In_{1-x},Ga_x)Se₂ is given by

$$E_g = 1.011 + 0.664x - 0.249x(1 - x) \quad (1-6)$$

The band gap of high conversion efficiency is about 1.2eV. And then the defect of lattice is higher due to the Ga concentration is too high when E_g is great than 1.3eV.

1.3.2 Phase diagram of CuInSe₂

The possible phases in the Cu-In-Se system are indicated in the ternary phase diagram show in Figure 1-8. Chalcopyrite CuInSe₂ is located on this line as well as a number of phases called ordered defect compounds (ODC), because they have a lattice structure described by the chalcopyrite structure with an ordered insertion of intrinsic defects. A detail of the Cu₂Se–In₂Se₃ tie-line near CuInSe₂ is described by the pseudobinary phase diagram show in Figure 1-9. Here α-phase is the chalcopyrite CuInSe₂, δ-phase is a high-temperature (HT) phase with the zinc blende structure, and β-phase is an ODC phase (CuIn₃Se₅). The Cu₂Se phase is similar to the β-phase and exists at room-temperature or high-temperature. The most relevant phase for application in solar cells is the α-phase. As shown the Figure 1-12, the range of α-phase is from 24-24.5 at % Cu at RT. At higher temperature (500 °C-550°C), the range of α-phase is from 22-24.5 at % Cu and wider than room temperature.

1.3.3 Impurities and Defects Phase

The chalcopyrite phase field is increased by the addition of Ga or Na [15]. By substitution of 20-30% of In by Ga, the α-phase region is

widened and the band gap of the CIGS layer is adjusted. The ratio of Ga/(Ga+In) is important for the solar cell performance. The optimal ratio is approximately 0.3 [9]. The effect of Na is consistent with the experimental observations of increased compositional range in which single phase chalcopyrite exists and increased conductivity [16][17].

If the material is Cu-poor and annealed in high Se-vapor pressure, which produce the P-type CIGS. But in Se saturation, Se atoms re-evaporate from the film, producing Se vacancies, which act as compensating donors. The dominant accept for p-type conduction is the Cu vacancy. If the material is Cu-rich and annealed in the insufficient Se-vapor, which produce the N-type CIGS. The dominant donor for n-type conduction is the Se vacancy. Defects in CIGS loom large because of the huge number of possible intrinsic defects playing an important role for the photovoltaic performance. The defects that are considered most important in device-quality material are presented in Table 1-2. The defect pair $2V_{Cu}^- + In_{Cu}^{2+}$ is an important characteristic in the CIGS film, which is low formation energy, stability and compensate the effect of non-stoichiometry. Even though the CIGS film is non-stoichiometry, the conversion efficiency still is high. The unusual stability of the defect pair $2V_{Cu}^- + In_{Cu}^{2+}$ leads to the formation of the ODC. Aperiodic spatial repetition of this pair gives ODC's [18].

1.4 Growth Methods of Cu(In,Ga)Se₂ Films

The preparation of Cu(In,Ga)Se₂-based solar cells starts with the deposition of the absorber material on a Mo-coated glass substrate. There were a large variety of approaches to be employed for CIGS-based

absorber layer fabrication, such as co-evaporation [19], RF sputtering [20], molecular beam epitaxy (MBE) [21], metal organic chemical vapor deposition (MOCVD) [22], spray pyrolysis [23] and electro-deposition [24], paste coating [25], particle deposition [26]. The major categories were co-evaporation process and selenization of precursor materials process in these methods of deposition Cu(In,Ga)Se_2 film. The co-evaporation process included two stage process [27] and three stage process [28], which were a vacuum technology and show in Figure 1-10. The other methods (RF-sputtering, MBE, MOCVD, spray pyrolysis, electro-deposition, paste coating and particle) used to deposition precursor materials of selenization process, which were vacuum and non-vacuum technology show in Figure 1-11. And then selenization process could be classified in H_2Se , elemental Se atmosphere and stacked elemental layer, which was diffusion of Cu and Se into $(\text{In,Ga})_2\text{Se}_3$ precursors films.

1.5 Motivation

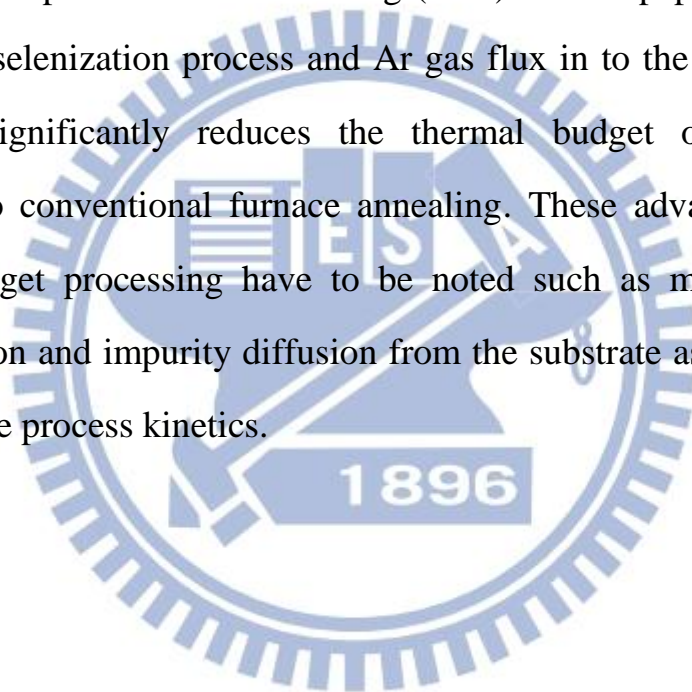
In the above mentioned, the three step co-evaporation technique has reached a confirmed photovoltaic energy conversion efficiency of about 20% [28]. This technique is limited to small area cells as evaporation from elemental sources was not suitable for large area coatings as composition uniformity cannot be maintained. And then co-evaporation technique has been the large amount of Se material used. These reason results in this technique had high cost compare to another technique. In this essay, we use the selenization of stacks of metals and compound

precursors for fabricated the large-area CIGS absorber layer. On the other hand, sputtering is widely known to be a technique easily scalable processes which are required for low-cost, large-area thin films solar cell production.

The selenization of sputtered Cu-In-Ga precursors using H₂Se vapor has been proven to be a suitable method for the industrial production of Cu(In,Ga)₂Se (CIGS)-based devices with the low cost. This technique has good control of the film growth, and result in CIGS based device of 16.2% [30]. One critical point is the use of high toxic H₂Se, which is problematic in terms of economic and ecological aspects. So some papers begin to research the elemental Se vapor as an alternative over the past few years [31-35]. Therefore, we choice the Se vapor as the source of deposition Se layer. And then we will use the Atmosphere Pressure Plasma Enhance Chemical Vapor Deposition (APPECVD) to assist in depositing cap Se layer. The APPECVD system uses the Dielectric-Barrier Discharge (DBD) linear plasma source show in Figure 1-12. Therefore, this technique has an ability of deposition large area and develops fabrication of roll to roll in the future. We used high voltage to dissociate selenium molecule, and molecule group become smaller than before. This system not only get the smaller molecule group but also produce the Se radical when the Se vapor through the atmosphere pressure plasma. We can deposit the dense Se film on the CIG precursor layer due to the smaller molecule group in atmosphere pressure plasma system. And then the Se radical will assist the deposition selenium films to improve dense and roughness. Additionally, the plasma could

successfully dissociate the selenium vapor, and cause to amorphous selenium films on the glass and Mo/glass. We expected the degree of crystalline chalcopyrite structure of CIGS films was improved by radical Se and then improved conversion efficiency of device. Simultaneously, if the substrate temperature was high, we could expect the selenium films to crystalize oriented (101).

The selenization system has two categories include close-space furnace and Rapid Thermal Processing (RTP). In this paper, we will use the RTP to selenization process and Ar gas flux in to the chamber. This technique significantly reduces the thermal budget of the sample compared to conventional furnace annealing. These advantages of low thermal budget processing have to be noted such as minimization of inter-diffusion and impurity diffusion from the substrate as well as better control of the process kinetics.



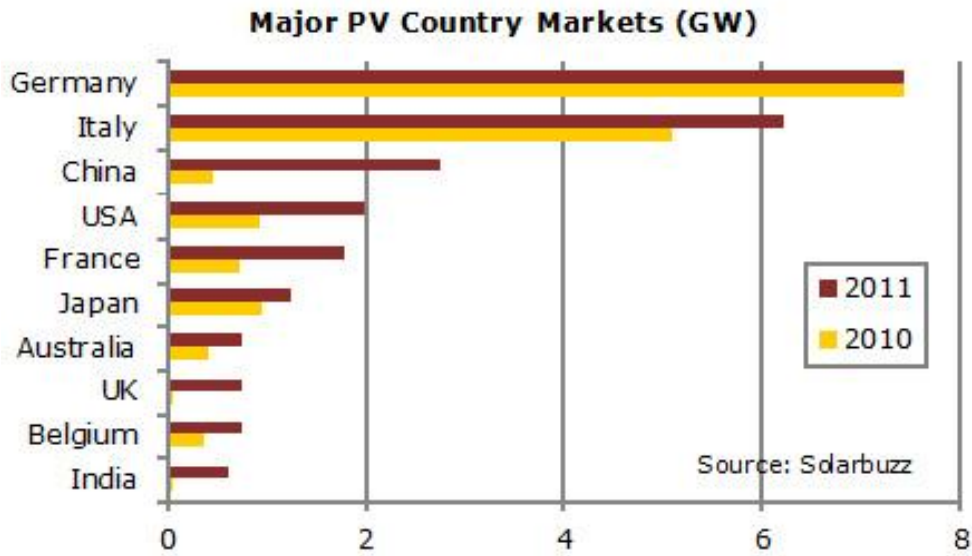


Figure 1-1 Major PV country markets (GigaWatts).

Source: NPD Solarbuzz 2012 Marketbuzz.

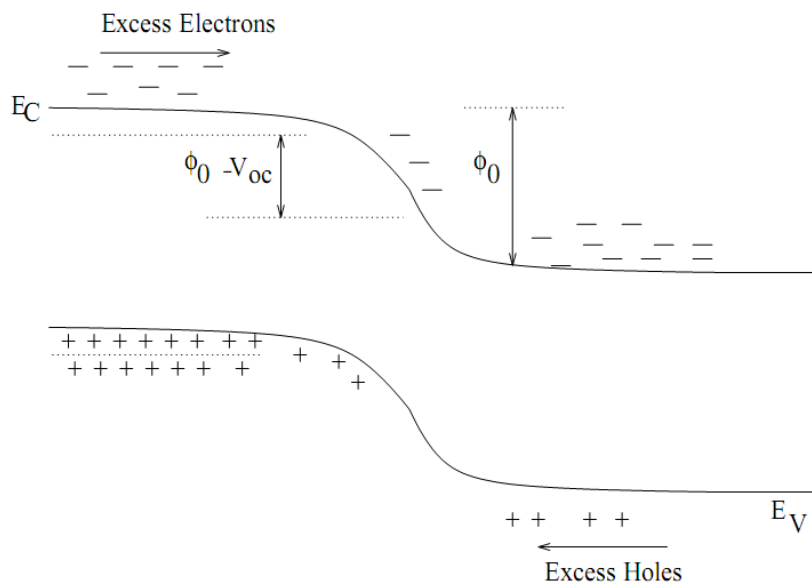


Figure 1-2 Energy Band Diagram of a P-N Junction under Illumination.

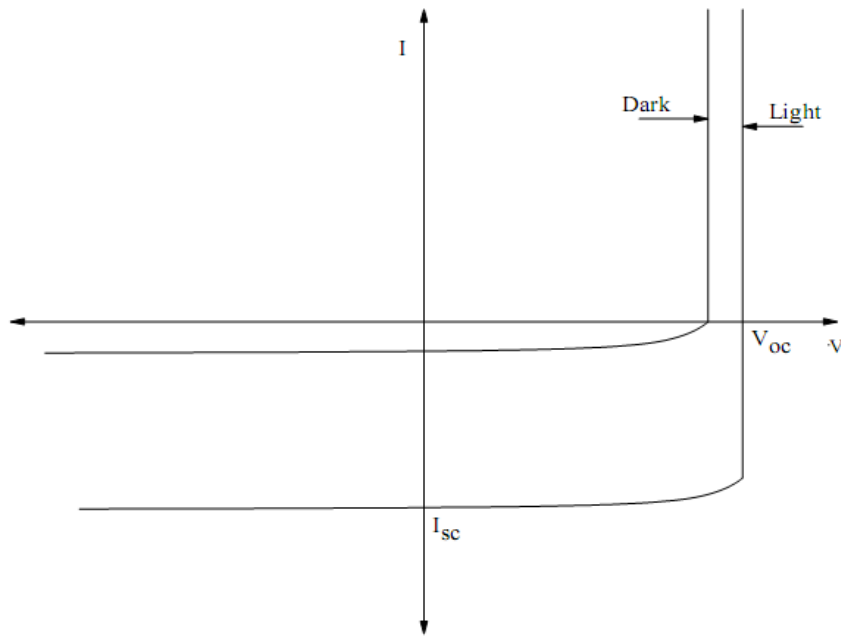


Figure 1-3 I-V Characteristics under Dark and Illumination.

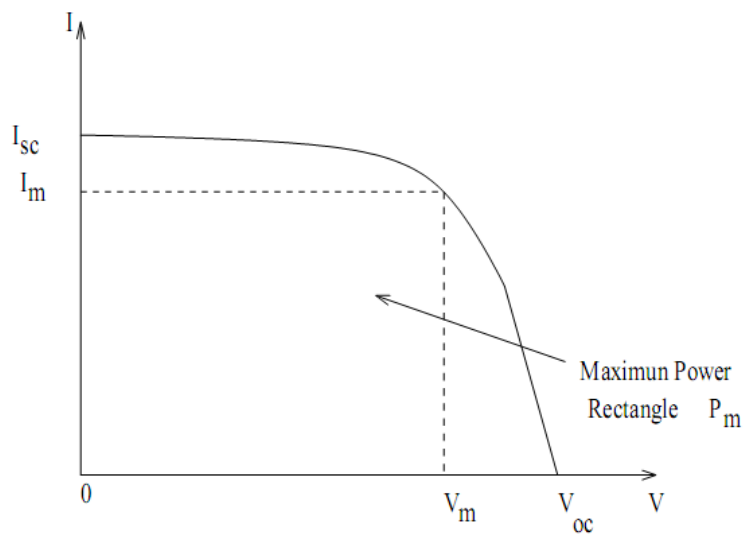


Figure 1-4 Inverted I-V Curve Showing Maximum Power Rectangle.

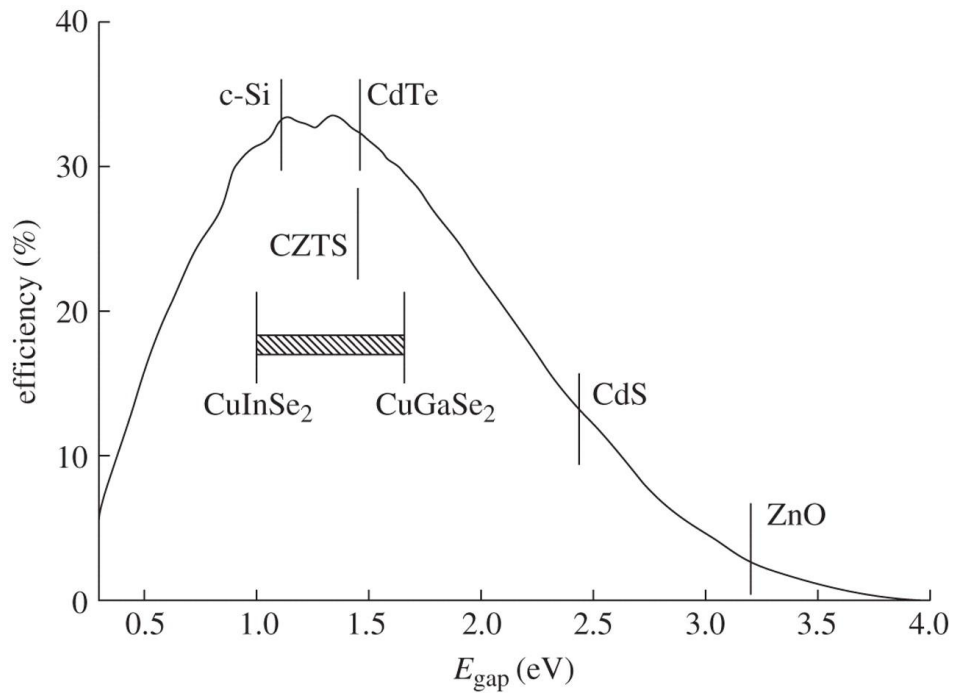


Figure 1-5 Shockley-Queisser Limits.

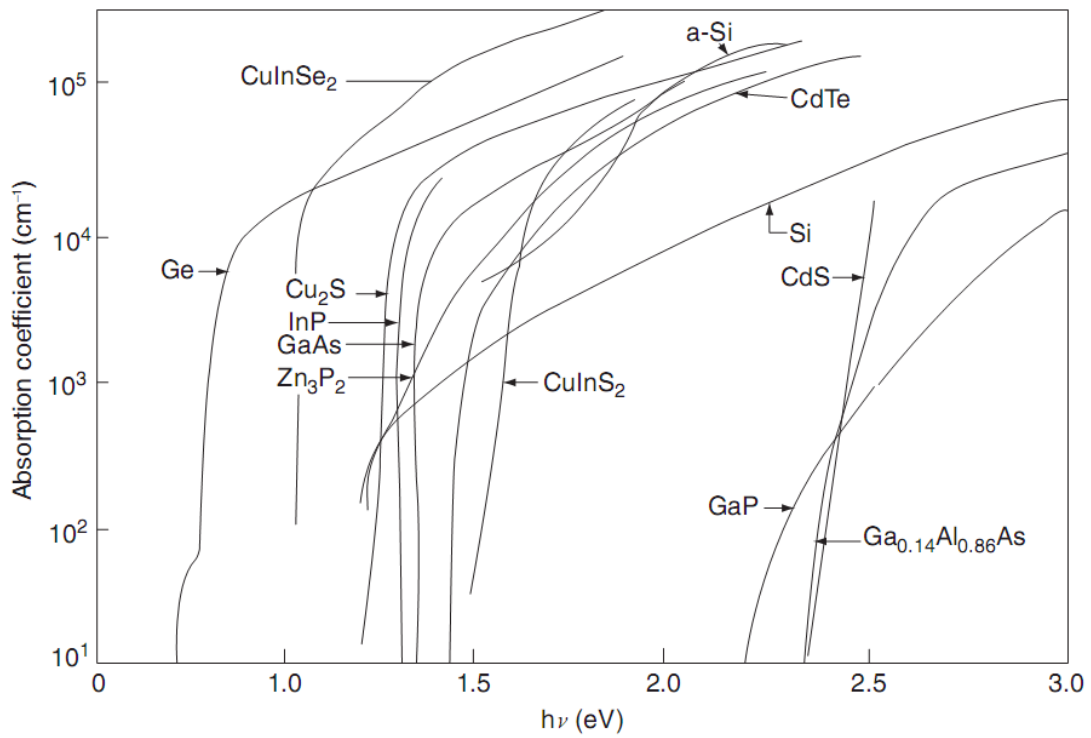


Figure 1-6 Absorption Coefficient versus Wavelength of Incident Light.[36]

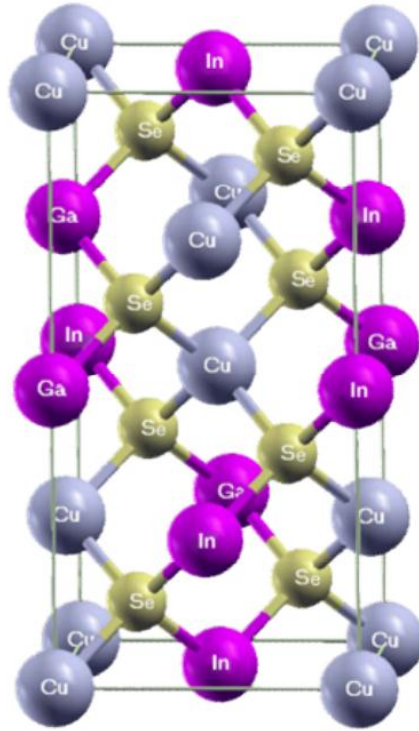


Figure 1-7 The Unit Cell of the Chalcopyrite Lattice Structure.[10]

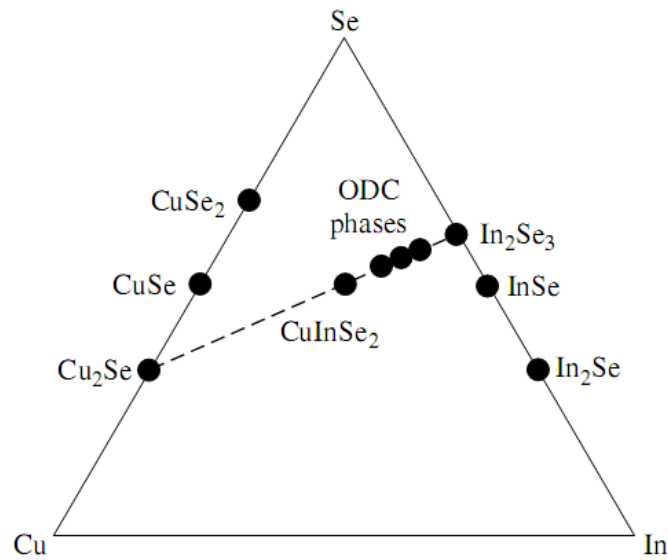


Figure 1-8 Ternary Phase Diagram of the Cu–In–Se System.[36]

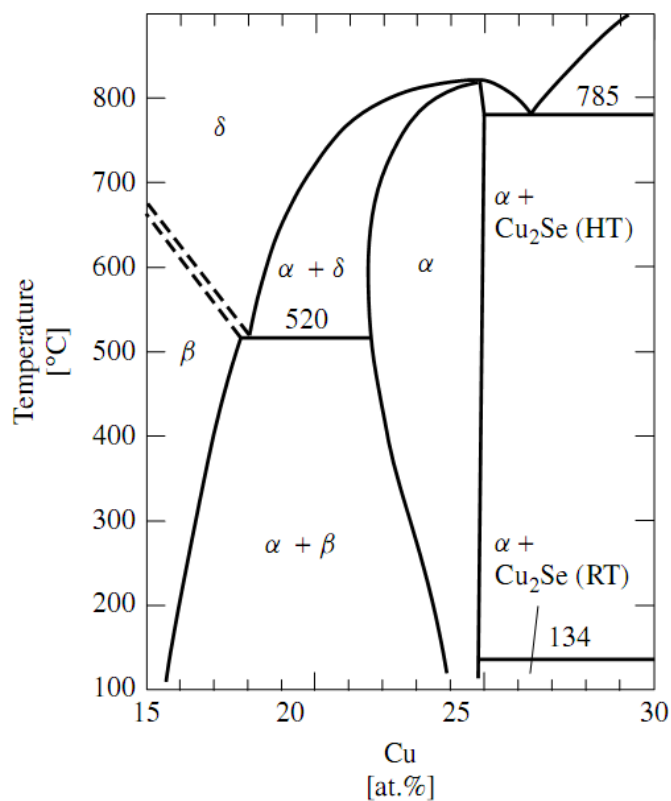


Figure 1-9 Pseudobinary Cut $\text{Cu}_2\text{Se}-\text{In}_2\text{Se}_3$ of Ternary Phase Diagram.[36]

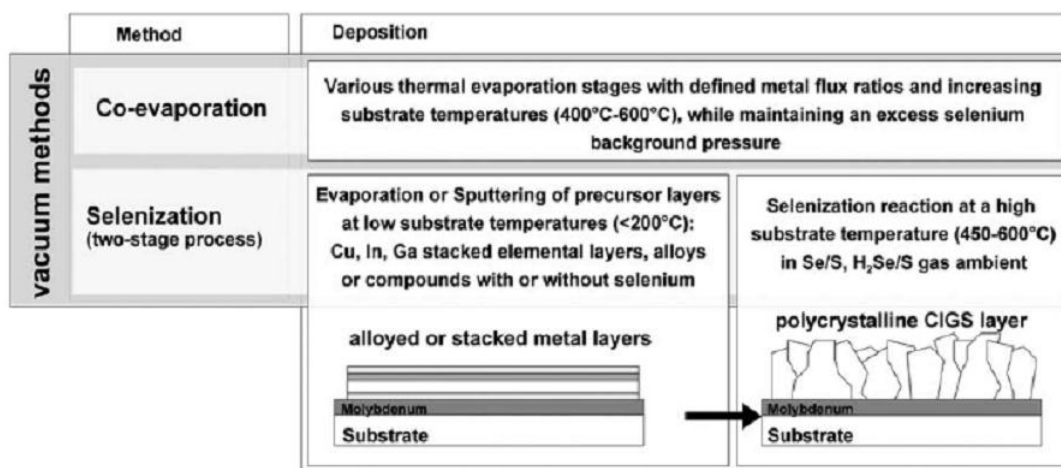


Figure 1-10 Vacuum Processes for $\text{Cu}(\text{In,Ga})\text{Se}_2$. [29]

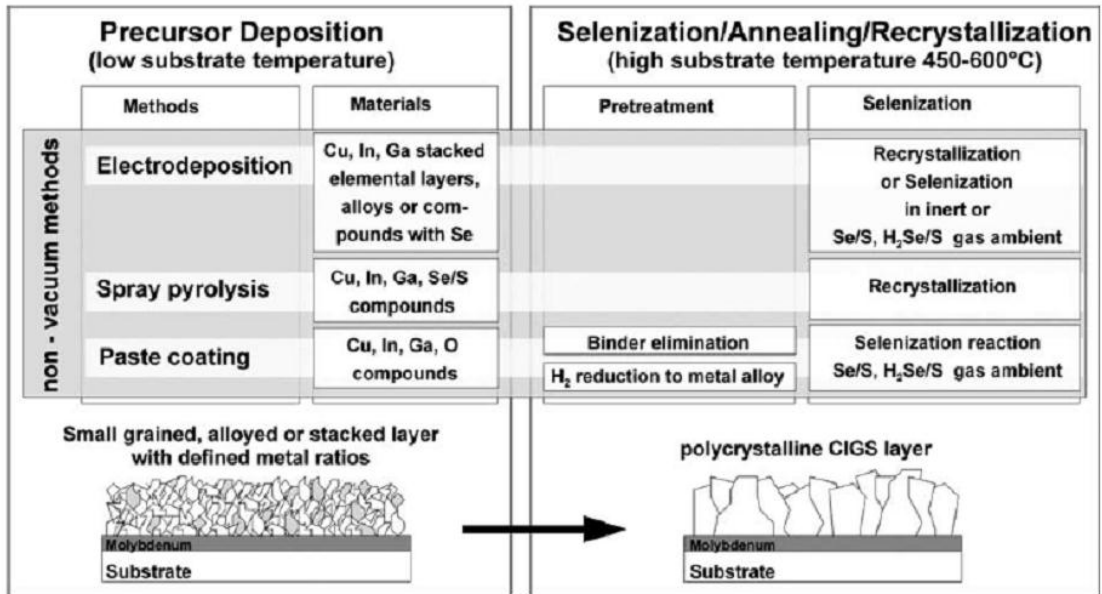


Figure 1-11 Non-Vacuum Processes for Cu(In,Ga)Se₂. [29]

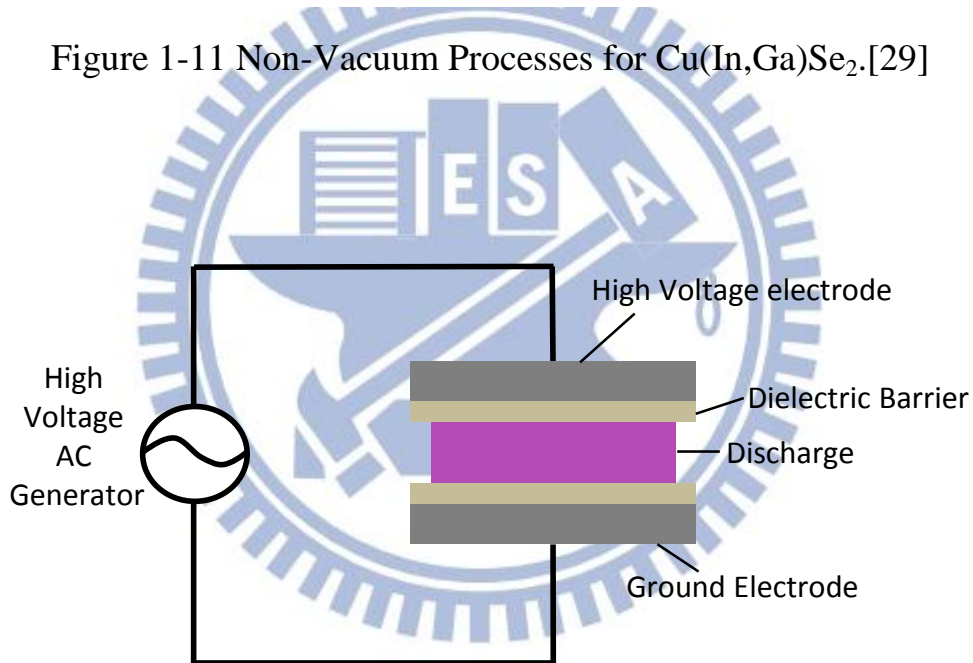


Figure 1-12 Dielectric-Barrier Discharge Linear Plasma Source.

Table 1-1 Selected Properties of CuInSe₂. [11-14]

Property		Value
Lattice constant (Å)	a	5.78
	c	11.62
Density (g/cm ³)		5.75
Melting temperature(°C)		986
Thermal expansion Coefficients at 273 K	(a axis)	8.32*10 ⁻⁶
	(c axis)	7.89*10 ⁻⁶
Thermal conductivity at 273 K		0.086
Dielectric constant	Low frequency	13.6±2.4
	High frequency	8.1±1.4
Effective mass	Electrons	0.09
	Holes(heavy)	0.71
	Holes(light)	0.092
Energy gap(eV)		1.02
Energy gap temperature coefficient (eV/K)		-2*10 ⁻⁴

Table 1-2 The Most Important Intrinsic Defects for Device-Quality CuInSe₂.

Native Point Defect	Electrical Activity
Cu _i , Se _{Cu} , In _{Se}	Single donor
V _{Se} , In _{Cu}	Double donor
In _I	Triple donor
V _{Cu} , Se _{In} , Cu _{Se}	Single acceptor
Se _i , Cu _{In}	Double acceptor
V _{In}	Triple acceptor

Chapter 2

Literature Reviews

2.1 The Material Properties of Selenium

Selenium is a semiconductor with the property of conducting electricity better in the light than in the dark, and is used in photocells. So the absorber layer of CIS/CIGS solar cell will use selenium element to combine quaternary compound. The basic properties of selenium are show in the Table 2-1. The amorphous selenium has two allotropic forms including black and red. The black amorphous selenium is citreous and is formed by rapid cooling of liquid selenium. The red amorphous selenium is colloidal and is formed in reduction reactions. The crystalline selenium has several allotropic forms due to the difference of crystalline structure. The stable form at room temperature is gray and the structure is hexagonal. This crystalline selenium is the densest and similar metallic in appearance. Crystalline red selenium exists in two monoclinic forms obtained by evaporation of carbon disulfide extracts of amorphous red selenium. The α -monoclinic form has a unit cell formed of four puckered Se_8 ring molecules. The β -monoclinic form is also made up of puckered Se_8 rings. The amorphous forms and both monoclinic crystalline forms transform to hexagonal forms gray selenium by heat. The saturated vapor pressure is given

$$\log P = 7.2355 - 5010.7/T \quad (2-1)$$

, where T is absolute temperature (K) and P is saturated vapor pressure (kPa) [37]. The primary species are $\text{Se}_n(2 < n < 8)$ in the selenium vapor at

below 900°C. Above mentioned data is arranged show in Table 2-2.

2.2 The Effect of Plasma Selenium

In 1994, S. T. Laskshimikumar and A. C. Rastogi use plasma to assisted two stage selenization process for the preparation of selenide semiconductor thin films using elemental selenium vapor. In this paper, the elemental selenium was used to produce the Selenium vapor. The reactivity of the selenium itself was enhanced by creating ionized selenium species in the vicinity of the metal precursor using RF radiation for the preparation of selenide semiconductor films. The Se_2 and Se of the Se vapor were created by the interaction with the RF radiation, which was the highly reactive element. Using this process, the semiconducting selenide films became highly crystalline and oriented at modest reaction temperature (250°C) even with short reaction time (2-5 min). In contrast, the crystalline without plasma treatment was smaller than with plasma treatment at higher reaction temperature (350°C-400°C) and with longer reaction time (20-30 min) [38].

In 2005, I. Repins, C. Wolden and H. Ullal used plasma-assisted co-evaporation of S and Se for wide band gap chalcopyrite photovoltaic. In this paper, the Se molecular species (Se_n , $2 < n < 8$) were converted to atomic species by low-pressure inductively-coupled plasma (ICP). The Gibbs energy of formation at 300K of Se atomic species was higher than Se molecular. So the atomic species required less energy to exceed the barrier of the formation of intermediate. In traditional fabrication of high-quality CIGS films like co-evaporation process required high

substrate temperatures ($>500^{\circ}\text{C}$), limiting the selection of substrate material. Therefore, this process expected to reduce the substrate temperature in the deposition films process and substrate material had more choices such as foil or stainless steel. This paper demonstrated with plasma activation the film was converted to the CIS chalcopyrite and no secondary phases were observed with substrate temperature $T_s=320^{\circ}\text{C}$ [39].

In 2007, Shogo Ishizuka, etc, report on the growth of CIGS films using a RF-cracked Se-radical beam source. The ICP plasma dissociated Se vapor to smaller Se-radical which was high reactivity. High reactivity of active Se-radical species created the modification of the kinetics of film growth, enhances migration during growth and improved the ability of In-Ga interdiffusion. The above factors led to CIGS film changed for higher dense, smoother surfaces and larger grain size than without RF-cracked Se-radical beam source. Though the film quality was significant improvement, but the photovoltaic performance was no significant influence. The energy conversion efficiency of solar cell was reached 17.5%. The radical source growth CIGS film has been to reduce the substrate temperature and increase the utilization of selenium material [40].

In 2011, Shogo Ishizuka, etc, then they announced another focus of using a RF-plasma cracked Se-radical beam source. Radical-Se grown CIGS solar cells showed some different properties of Evaporation-Se grown CIGS solar cells. The conversion efficiencies of solar cells be enhance by the RF-plasma cracked Se-radical beam source due to

increase open circuit voltage and fill factor, though simultaneously decreased the short circuit current density. The sodium content of the CIGS film by radical selenium treatment was higher and the sodium expected to inhibit element interdiffusion. Therefore, film growth slows down created beneficial selenium diffusion in the CIGS film. After this process CIGS film has a better quality and caused to improve the open-circuit voltage and fill factor of the CIGS solar cell. The reason of decrease short-circuit current was the smooth surface morphology which created reduction of light trapping [41].

2.3 Prepared to Cu(In,Ga)Se₂ Absorber Layer

A wide variety of thin-film deposition methods has been used to deposit Cu(InGa)Se₂ thin films. In this paper, we categorize them in co-evaporation and sequential processes (selenization). And then the selenization processes include elemental Se atmosphere and stacked elemental layer. Following the exposition will discuss them in detail.

2.3.1 Co-evaporation Process

The co-evaporation process is the vacuum technique. The setup is show in Figure 2-1. The system has four Knudsen type MBE cells that allow an optimal control of the deposition speed ($1-5\text{\AA}/\text{s}$) for every material and on the thickness for the deposited film ($0.5-4\mu\text{m}$). The base pressure in the vacuum chamber is carried out reaches a value of 10^{-6} Torr. This technique should have high purity material Cu (Kurt Lesker, 99.999%), Ga (Alfa Aesar, 99.9999%). Se (Kurt Lesker, 99.999%) and In (Kurt Lesker, 99.999%). Source temperatures of every material are:

$T_{so}(Cu)=1300-1400^{\circ}C$, $T_{so}(In) = 1000-1100^{\circ}C$, $T_{so}(Ga) = 1150-1250^{\circ}C$ and $T_{so}(Se) = 300-350^{\circ}C$. The process requires a substrate temperature between $300^{\circ}C$ and $550^{\circ}C$ for a certain time during film growth.

The fabrication procedure of three step co-evaporation process has several species. The popular species is NREL three-step co-evaporation and conversion efficiency as high as 19.5% [42]. At first In, Ga and Se are evaporated with different rates and deposited as $(In,Ga)_2Se_3$ at $300^{\circ}C$ on the substrate. Afterwards Cu and Se are evaporated and deposited on the substrate at elevated temperatures. At last In, Ga, and Se are evaporated again. The inverted three-stage process leads to smoother film morphology and high efficiency solar cells.

The generally properties of co-evaporation process are described following:

- (1) Highest conversion efficiency of device.
- (2) In expensive raw materials.
- (3) Demonstrated in production is easier than other technique.
- (4) The process control is difficult due to the substrate temperature is difference at different procedure.
- (5) Material utilization is disappointing, because the most material is coating on the chamber.
- (6) The cost per unit cell is high due to the material utilization is bad and maintain the vacuum system.
- (7) The area of solar cell device is limited by evaporation length. Because the chamber become large in order to make large area of solar cell device.

2.3.2 Prepare Precursor Layer by Sputtering

In order to grow precursor layer the schematic diagram of RF sputter system is shown in Figure 2-2. After evacuation of chamber to 1×10^{-6} Torr, pure Ar is introduced into chamber to sputter target and maintain pressure of 1×10^{-2} Torr. The purity Ar with flow rate of 6-15 sccm is applied. Prior to deposition of thin films, pre-sputtering is done for 10 min to clean contamination under working pressure of 3×10^{-2} Pa.

The sputtering technique is much the same and the only thing that difference of the target. In recent years the research studies in this technique that change many target or stack element for the purpose of get higher conversion efficiency.

The Cu-In-Ga ternary sputtering target was manufactured by turning a ternary-alloyed ingot cast from a molten alloy melted by a vacuum arc-refining furnace. The source materials of the ingot had a pre-determined composition of high-purity (≥ 99.999 at %) constituents, Cu, In, and Ga, at 50, 35, and 15 at%, respectively. Use the RF-sputtering to deposit Cu-In-Ga layer on the Mo/glass. Then, a Se film was deposited by vacuum evaporation onto the Cu-In-Ga precursor layer (without intentional heating) at a background pressure of 104 Pa. The glass/Mo/Cu-In-Ga/Se samples were firstly placed in a rapid thermal annealing. The RTA temperature first step is continue 1-10 min at low temperature (100°C), then selenization process was carried out at high temperature ($\geq 450^\circ\text{C}$) [43].

In the first step, two types of precursor structures were employed: (1) a CuInGa/Mo single layer and (2) a CuGa/CuInGa/Mo layer. In the first

type of structure (1), a 650 nm thick film of CuInGa/Mo precursors was deposited by DC magnetron sputtering of a $\text{Cu}_{0.9}\text{In}_{0.75}\text{Ga}_{0.25}$ ternary target onto Mo-coated soda-lime glass substrates. In the second type of structure (2), an additional 85-nm thick CuGa film was sputtered on top of the CuInGa/Mo structure using $\text{Cu}_{0.7}\text{Ga}_{0.3}$ target. In the second step, the above mentioned metallic precursors were selenized using a Se vapor in a quartz tube furnace. The temperature of selenization process was 500°C for 20 min in order to form the p-type CuInGaSe_2 chalcopyrite structure [44].

The generally properties of sputtering process are described following:

- (1) The process control is easy.
- (2) Have high materials utilization due to the diffusion length of sputtering system is smaller than co-evaporation.
- (3) This technique easily scalable to large-area manufacturing processes and more uniform than other technique for the large-area manufacturing process.
- (4) High production rates.
- (5) The conversion efficiency of CIGS solar cells by sputtering have remained low as compared to co-evaporation

2.3.3 Prepare Precursor Layer by Electro-Deposition

In recent years, there are many new technological developments to make the large area of CIGS solar cells. Electro-deposition has the potential to develop into the manufacturing technology of large area.

CIGS films were prepared adopting co-electro-deposition of the four elements of Cu, In, Ga and Se. The potentiostatic technique with a conventional three-electrode configuration was used, where the reference electrode was a saturated calomel electrode (SCE), the counter electrode was Pt mesh and the working electrode was a Mo-coated soda-lime glass substrate. The electro-deposition bath consisted of CuCl_2 , GaCl_3 , InCl_3 , H_2SeO_3 and 1.0 M Na-citrate. To obtain ideal CIGS thin films, InCl_3 and GaCl_3 in sufficient quantity were added to the chemical bath to adjust the final composition of CIGS near to ideal stoichiometry. The pH of the chemical bath was adjusted to be 1.5 by adding drops of concentrated HCl. The selenization of the films was carried out in a tubular furnace. CIGS thin films were annealed at 550°C in selenium atmosphere for 1 h. To prevent Se atom of CIGS thin films escaping, excessive selenium powder as a selenium source instead of high toxic H_2Se gas was added during the heat treatment [45].

The generally properties of electro-deposition process are described following:

- (1) The process control is easy.
- (2) Have high materials utilization due to electro-deposition use solution to deposition thin film.
- (3) This technique easily scalable to large-area manufacturing processes.
- (4) High production rate due to high deposition speed.
- (5) The ability of uniform and adhesion need to be improved.
- (6) The conversion efficiency of CIGS solar cells remained low.

2.4 Atmospheric pressure plasma system

2.4.1 Arc Plasma

The operation of arc plasma is similar to an arc-welding machine, where an electrical arc is struck between two electrodes. The high energy of arc creates high temperatures ranging from 3000°C to 7000°C. The plasma is highly ionized gas which is enclosed in a chamber. The waste material is fed into the chamber and the intense heat of the plasma break down organic molecules into their elemental atoms. In the strict control of the process, these atoms recombine into harmless gases, such as carbon dioxide. Solids such as glass and metals are melted to form materials, similar to hardened lava, in which toxic metals are encapsulated. There is no burning or incineration and no formation of ash with plasma arc technology. There are two main types of plasma arc processes: plasma arc melter and plasma torch.

Plasma arc melters have very high destruction efficiency. They are very robust; they can treat any waste with minimal or no pretreatment; and they produce a stable waste form. The arc melter uses carbon electrodes to strike an arc in a bath of molten slag. The consumable 28 carbon electrodes are continuously inserted into the chamber, eliminating the need to shut down for electrode replacement or maintenance. The high temperatures produced by the arc convert the organic waste into light organics and primary elements.

Combustible gas is cleaned in the off-gas system and oxidized to CO₂ and H₂O in ceramic bed oxidizers. Due to the use of electrical heating in the absence of free oxygen, the potential for air pollution is low. The

inorganic portion of the waste is retained in a stable, leach-resistant slag.

In plasma torch systems, an arc is struck between a copper electrode and either a bath of molten slag or another electrode of opposite polarity. Plasma torch systems have very high destruction efficiency with plasma arc systems; they are very robust; and they can treat any waste or medium with minimal or no pre-treatment. The inorganic portion of the waste is retained in a stable, leach-resistant slag. The air pollution control system is larger than for the plasma arc system, due to the need to stabilize torch gas.

2.4.2 Atmospheric Pressure Plasma Jet

Atmospheric pressure plasma jet is meaning that operating at atmospheric pressure and it is non-thermal glow discharge plasma system. The non-thermal plasma generates highly reactive ions, electrons and free radicals. The reactive species are directed onto a surface where the desired chemistry occurs. However the overall gas temperature remains quite cold, but the electrons are quite hot, typically 50-300°C.

2.4.3 Corona Discharge

A corona is a process by which a current develops between two high-potential electrodes in air, by ionizing that fluid to create a plasma around one electrode, and by using the ions generated in plasma processes as the charge carriers to the other electrode.

Corona discharge usually involves two asymmetric electrodes, one highly curved such as the tip of a needle or a narrow wire, and another

one of low curvature such as a plate or the ground. The high curvature assures a high potential gradient around one electrode, for the generation of the plasma.

Coronas may be positive, or negative. This is calculated by the polarity of the voltage on the high curvature electrode. If the curved electrode is positive associated to the flat electrode, it will have a positive corona, and vice versa. The physics of positive and negative coronas are obviously different. This asymmetry structure is a result of the great difference in mass between electrons and positively charged ions, and so only the electron having the ability to undergo a significant degree of ionizing inelastic collision at common temperatures and pressures.

2.4.4 Dielectric Barrier Discharge (DBD)

Dielectric barrier discharges involve a specific class of high voltage, ac, gaseous discharges that typically operate in the near atmospheric pressure range. Their defining feature is the presence of dielectric layers that make it impossible for charges generated in the gas to reach the conducting electrode surfaces. With each half cycle of the driving oscillation, the voltage applied across the gas exceeds that required for breakdown, and the formation of narrow discharge filaments initiates the conduction of electrons toward the more positive electrode. As charge accumulates on the dielectric layer at the end of each filament, the voltage drop across the filament is reduced until it falls below the discharge sustaining level, therefore the discharge is quenched. The low charge mobility on the dielectric not only contributes to this self-arresting

of filaments but also limits the lateral region over which the gap voltage is diminished, thereby allowing parallel filaments to form in close proximity to one another. Thus, the entire gas filled space between parallel electrodes can become, on average, uniformly covered by transient discharge filaments, each roughly 0.1mm in diameter and lasting only about 10ns.

The DBD's unique combination of non-equilibrium and quasi-continuous behavior has provided the basis for a broad range of applications and fundamental studies. Its use in industrial ozone reactors has generated interest in optimizing conditions for specific chemical reactions. To this end, experimental DBD studies have explored different gas mixtures, electrical characteristics, and geometries. Related work has focused on maximizing the ultraviolet radiation from excimer molecules produced in DBD's. Several researchers have modeled single filament dynamics in order to account for the many reactions involving electrons, ions, neutral atoms, and photons. These efforts have been moderately successful in explaining and predicting the chemical and radiative properties of various DBD systems. On another research effort, it has been seen that the transverse spatial distribution of discharge filaments in 2D, parallel plate DBD's can take the form of stable, large-scale patterns reminiscent of those associated with magnetic domains. These patterns have been modeled with some success using methods that apply generally to pattern formation in nonlinear dynamical systems. Thus, the dynamical interactions between filaments, as well as the chemical and electronic interactions within filaments have proven interesting.

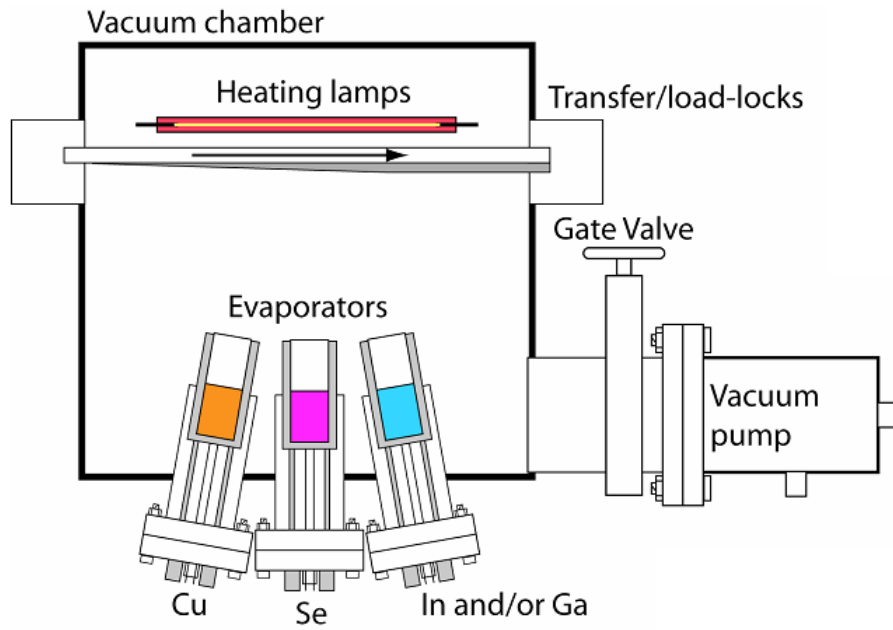


Figure 2-1 Schematic Diagram of Co-evaporation System.[46]

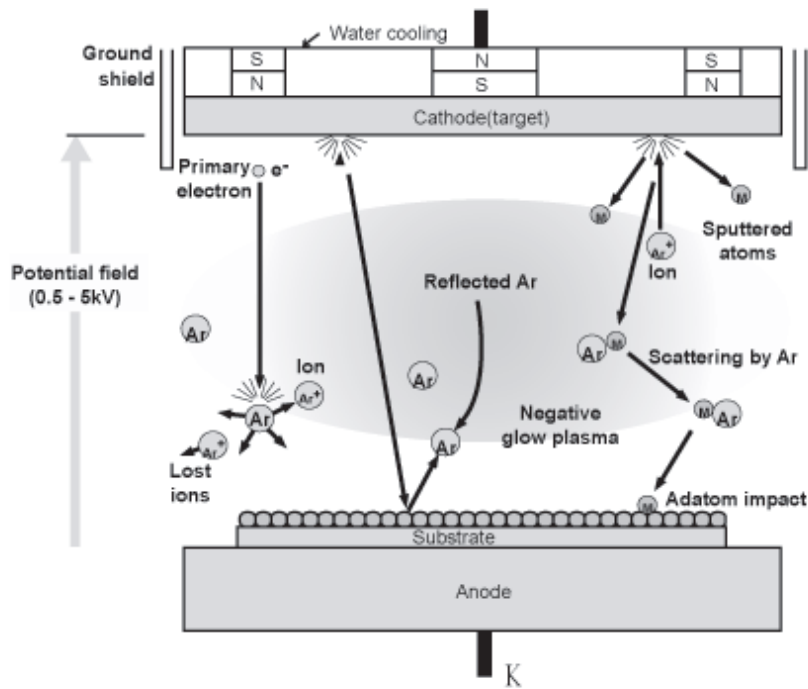


Figure 2-2 Schematic Diagram of RF Sputtering System.[47]

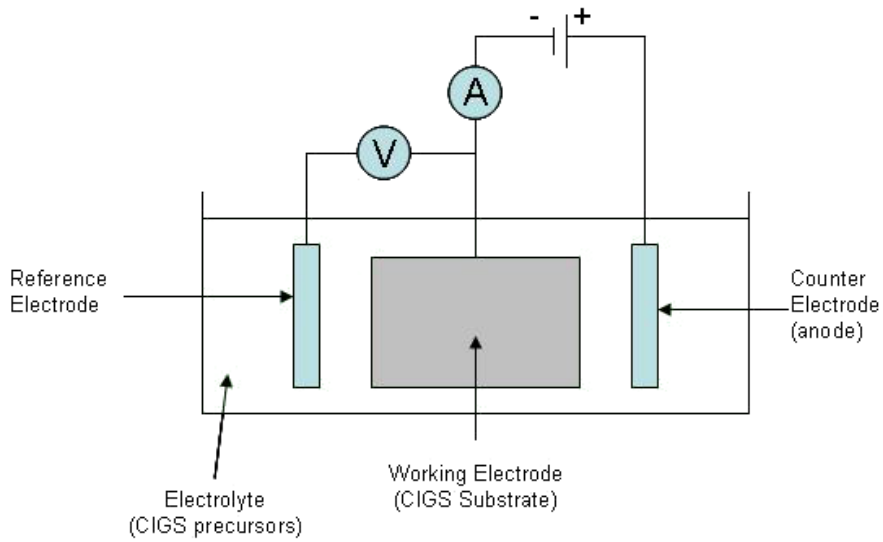


Figure 2-3 Schematic Diagram of Electro-Deposition System.[48]

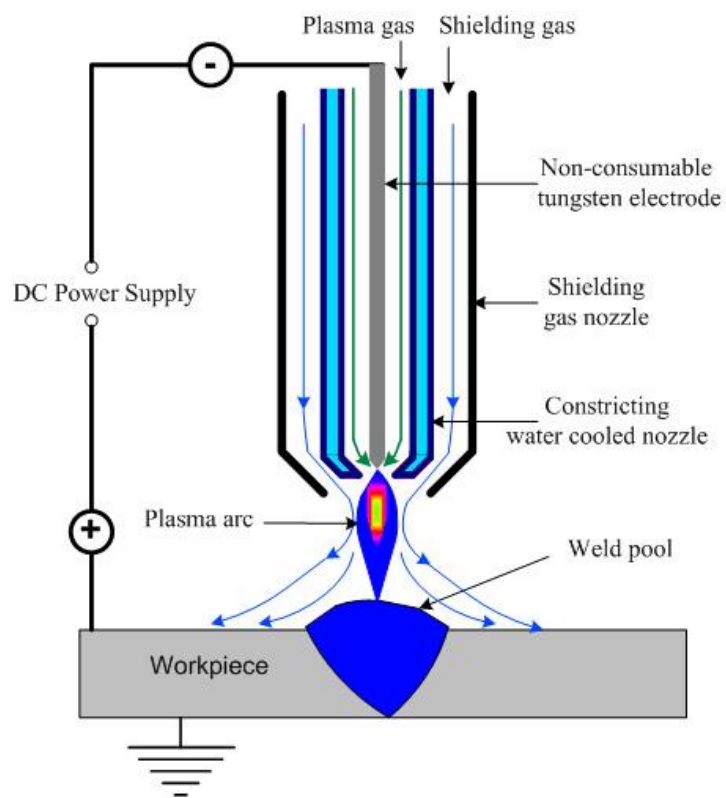


Figure 2-4 Schematic Illustration of the Arc Plasma.[49]

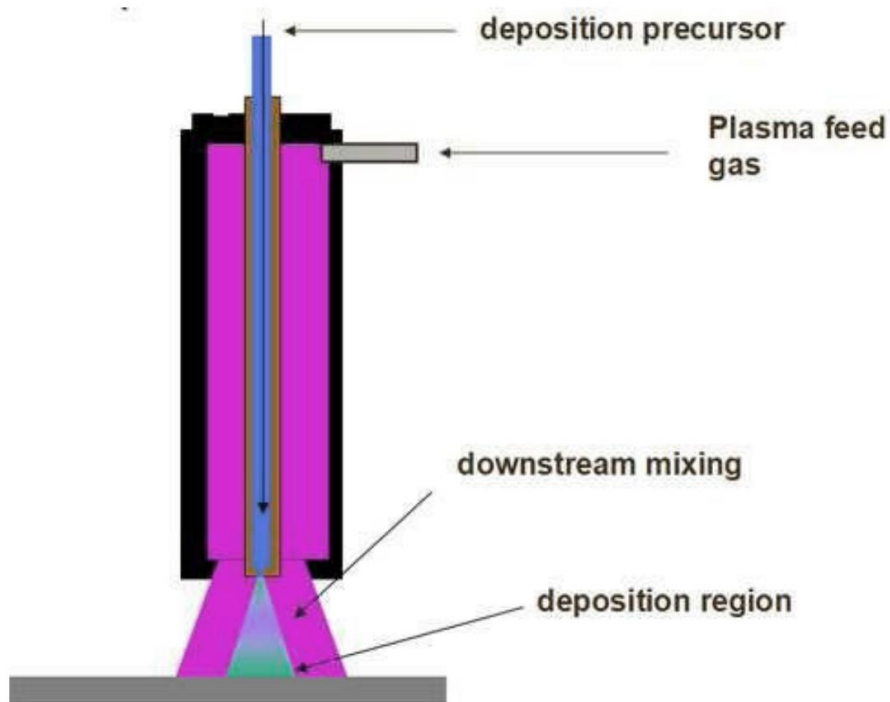


Figure 2-5 Schematic Illustration of the AP Plasma Jet structures.[50]

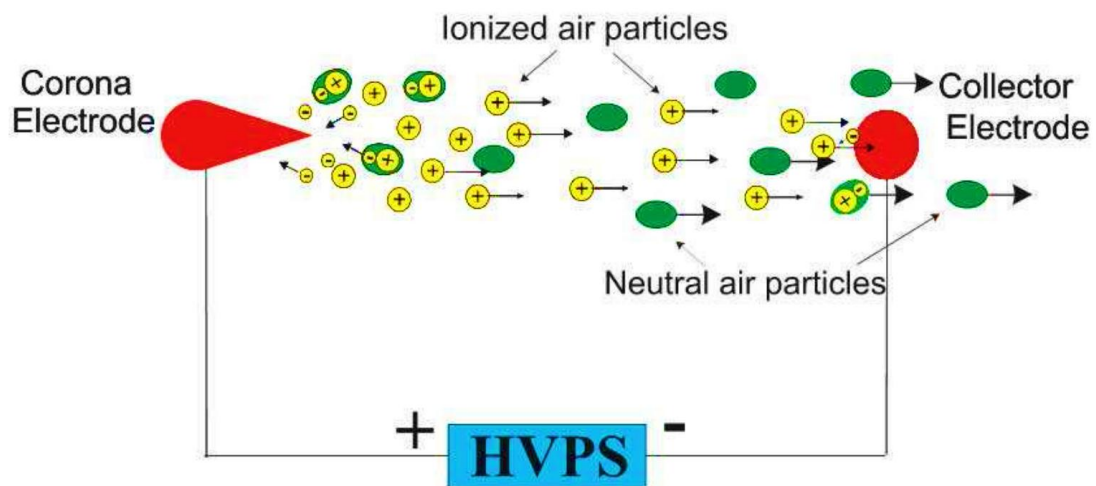


Figure 2-6 Schematic the Principle of Corona Discharge.[51]

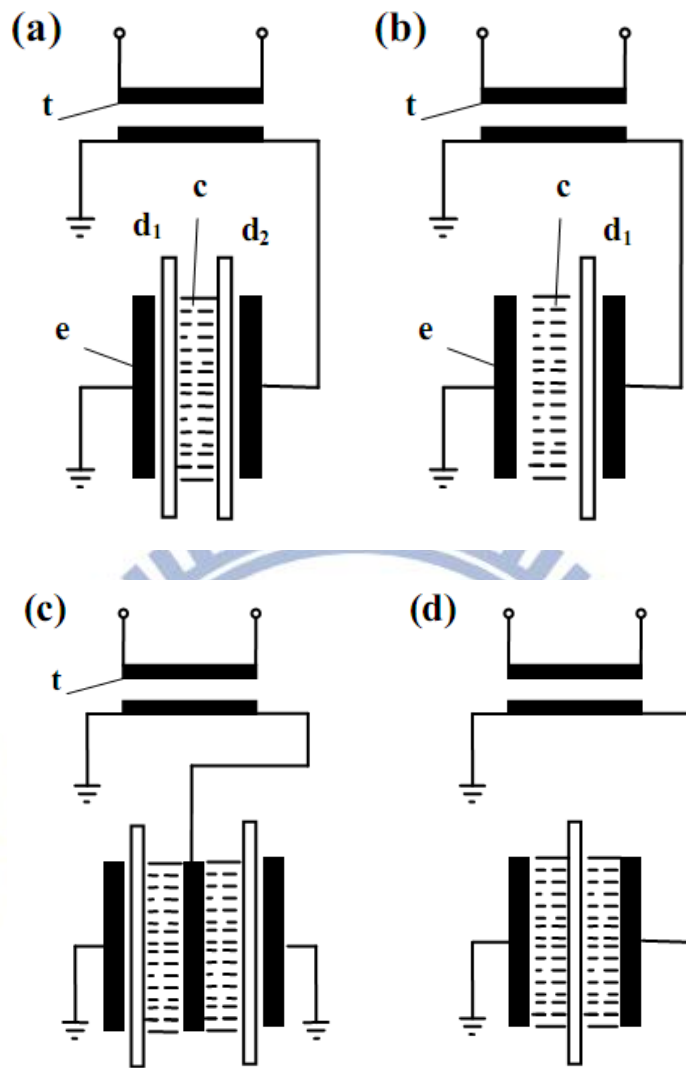


Figure 2-7 Schematic the Principle of Dielectric Barrier Discharge.[52]

Table 2-1 The Properties of Selenium.

Physic Properties	
Atomic Number	34
Atomic Mass	78.96
Melting Point	220°C
Boiling Point	685°C
Oxidation States	-2 、 0 、 +2 、 +4 、 +6
Electron affinity	194.97 KJ/mol (2 eV)
Dissociation of the selenium dimer	88 kcal/mol (3.81eV)
Vapor Pressure (Pa)	
$T_{se}=335^{\circ}\text{C}$	98.67
$T_{se}=355^{\circ}\text{C}$	180.58
Ionization Energy (eV)	
1 st	9.75
2 nd	21.2
3 rd	30.82
Density (g/cm ³)	
Hexagonal at 298K	4.819
Monoclinic	4.4
Liquid at 490K	4.05
Vitreous	4.285

Table 2-2 Amorphous and Crystalline Selenium.



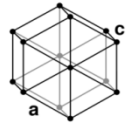

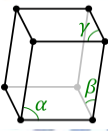
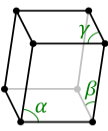
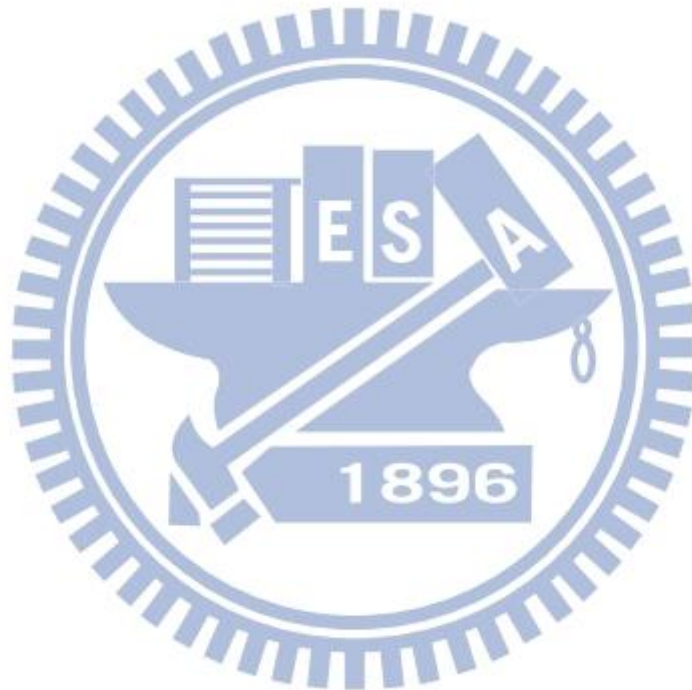
Form	Structure	Appearance	Characteristic
Amorphous Selenium	Amorphous	Vitreous and Black 	Rapid cooling of liquid selenium
		Colloidal and Red 	Reduction reactions
Crystalline Selenium	Hexagonal a = 0.4366 nm c = 0.4954 nm 	Grey and Similar Metal 	The electrical conductivity of illumination greater than dark
	α - Monoclinic a=0.9054nm b=0.9083nm c=1.1060nm 	Red	Four puckered Se ₈ ring molecules
	β - Monoclinic a=1.285nm b=0.807nm c=0.931 nm 	Red	Four puckered Se ₈ ring molecules

Table 2-3 Density of Charge Species in the Plasma Discharge.

Source	Plasma Density (cm ⁻³)
Low Pressure Discharge	10 ⁸ -10 ¹³
Arc and Plasma Torch	10 ¹⁶ -10 ¹⁹
Corona Discharge	10 ⁹ -10 ¹³
Dielectric Barrier Discharge	10 ¹² -10 ¹⁵
Capacitive Discharge	10 ¹¹ -10 ¹²



Chapter 3

Experiments

3.1 Experimental Procedures

3.1.1 Optimize the Fabrication Parameters

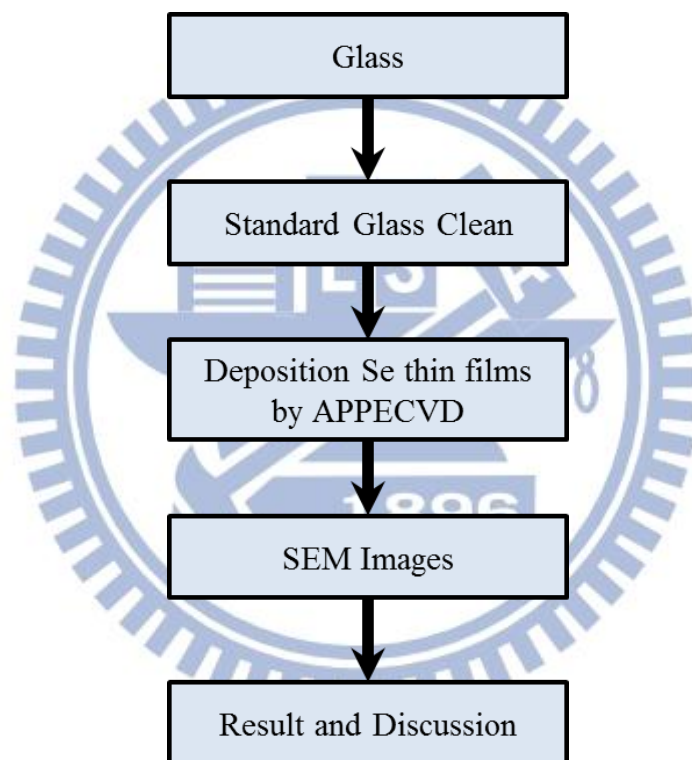


Figure 3-1 Schematic Illustration of Optimize the Fabrication Parameters.

3.1.2 Investigation of Selenium Films by APPECVD

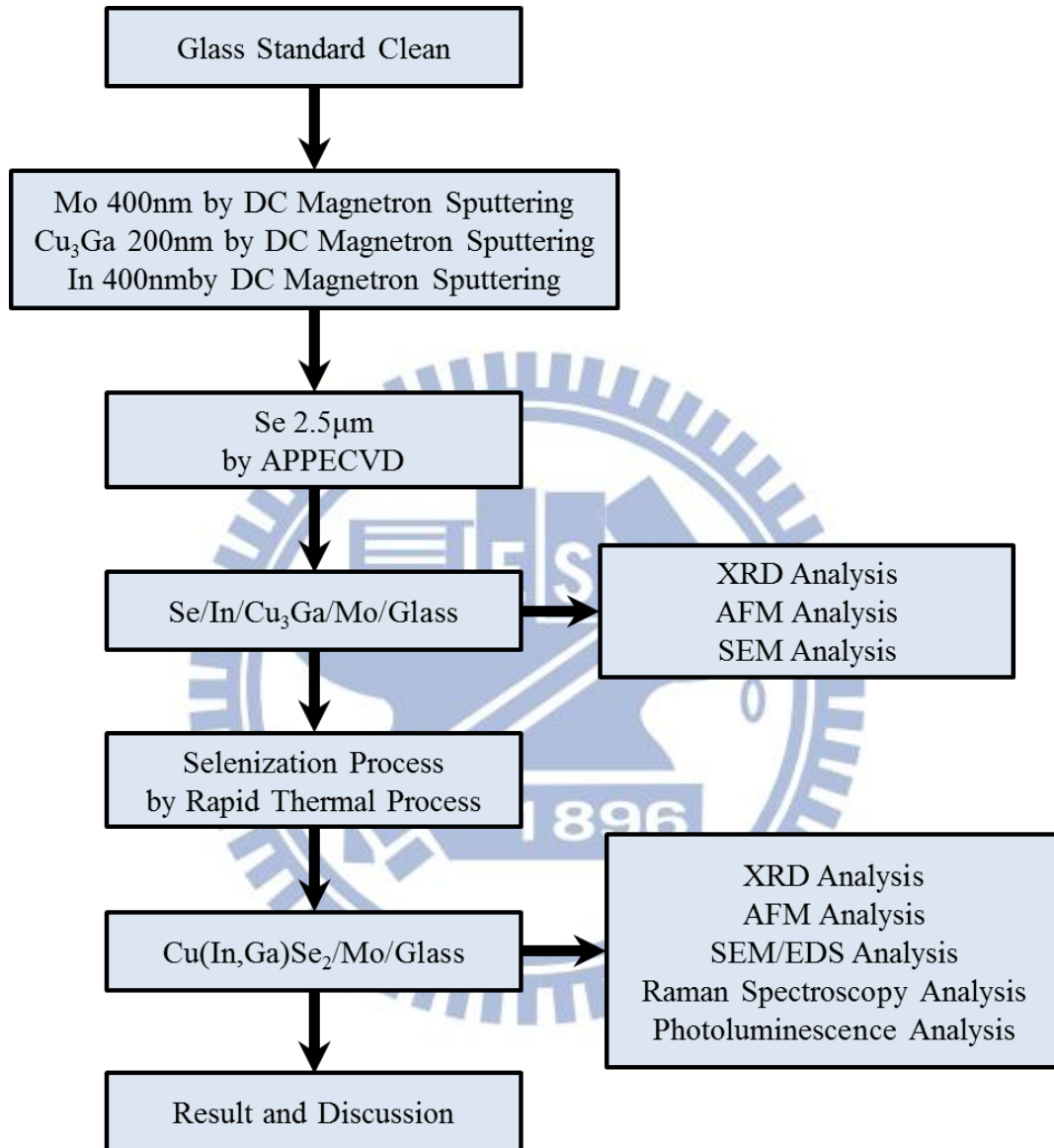


Figure 3-2 Schematic Illustration of Investigation of Selenium Films by APPECVD.

3.1.3 Investigation of Device Characterization

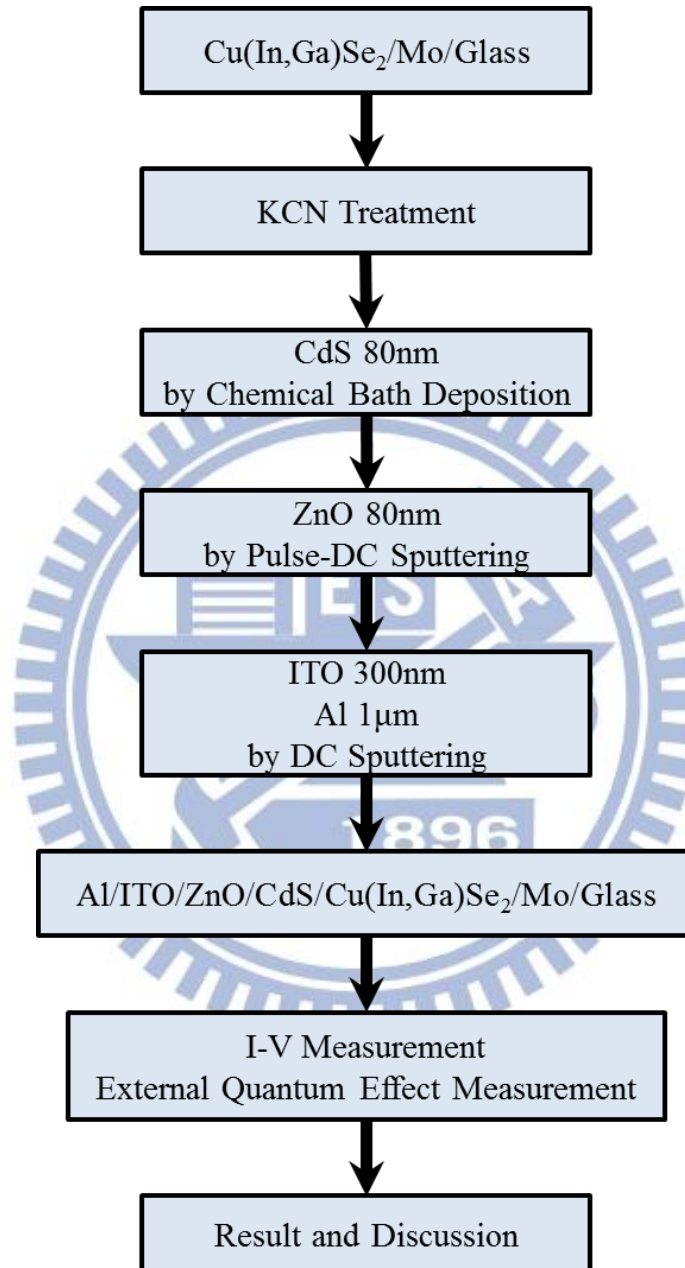


Figure 3-3 Schematic Illustration of Investigation of Device Characterization.

3.2 Experimental Equipment and Parameters

3.2.1 Experimental Equipment

The equipment of amorphous pressure plasma chemical vapor deposition is shown in Figure 3-4. This technique uses the element Se vapor to deposit Se film. The source of selenium vapor is selenium pellet heated by the heater to higher than 220°C and the selenium vapor fills the quartz holder. The equipment uses Argon gas as the carrier gas and the main gas, and carries the Se vapor to pass through the electrode of applied high voltage. Therefore, the plasma will dissociate the ring structures of Se_n , where n varies from $2 < n < 8$, and become the Se element. And then the Se element is carried by the carrier gas to deposit on the substrate. A gap is between the quartz holder and the substrate, which affects the quality and deposition rate of the selenium film. The substrate temperature can be controlled by the hot plate in order to benefit the deposition of the film. In this equipment, the substrate is immovable, but the quartz holder and electrode are movable. The scan area is shown in Figure 3-5, which is $10 \times \Delta x \text{ cm}^2$, where Δx is the moving distance of the quartz holder.

3.2.2 Experimental Parameters

The standard glass clean procedure is as follows:

- (1) Ultrasonic clean in Acetone 10min
- (2) Ultrasonic clean in Isopropanol 10min
- (3) Ultrasonic clean in DI water 10min
- (4) Nitrogen Drying

The APPECVD systems have lots of parameters including power, substrate temperature, gap distance, scan times, scan speed, carrier gas flow rate, background pressure, selenium temperature. The experimental of optimize the fabrication parameters in order to find the optimal fabrication parameters for the APPECVD system. Use change the different parameters, i.e. selenium temperature, carrier gas flow rate, background, power, to investigate quality, surface roughness and deposition rate of selenium film on the glass. The parameters are show in Table 3-1.

The parameters of investigation of selenium films by APPECVD are show in Table 3-2. Use change the different plasma power and substrate temperature to investigate quality, surface roughness, crystalline, adhesion of selenium film on the CIG recourse layer. In this essay, the Se/In/CuGa/Mo/Glass samples will sequentially run the selenization in 550°C by the RTP process, the temperature curve of RTP process was show in Figure 3-6. And then investigate quality, surface roughness, crystalline, compound, composition of Cu(In,Ga)Se₂ film on coated-Mo glass. The cell completions of Al/ITO/ZnO/CdS/CIGS grown on Mo-coated substrate follow by the standard process. The current density-voltage (J-V) measurement was performed under the standard AM1.5G spectrum for 100mW/cm² irradiance at room temperature. The optical loss mechanism of the device can measure by external quantum effect (EQE).

3.3 Characterization Analysis and Measurement Equipment

3.3.1 Scanning Electron Microscopy (SEM)

SEM stands for scanning electron microscope. The SEM is a microscope that substitute electron for light to form an image. Scanning electron microscopes have developed new areas of study in the medical and physical science communities since their development in the 1950. SEM uses a focused beam of high energy electrons to generate a variety of signals at the surface of solid samples. The signals that derive from electron and sample interactions reveal information about the sample including external morphology, chemical composition, and crystalline structure and orientation of materials making up the sample. The researchers can inspect a much larger variety of samples by SEM.

Accelerated electrons carry significant amounts of kinetic energy in the SEM. When the incident electrons are decelerated in the solid sample, this energy is dissipated as a variety of signals produced by electron and sample interactions. These signals include secondary electrons, backscattered electrons, diffracted backscattered electrons, photons and heat. Secondary electron and backscattered electrons are commonly used for imaging samples. Secondary electrons are most valuable for showing morphology and topography on samples and backscattered electrons are most valuable for illustrating contrasts in composition in multiphase sample. X-ray generation is produced by inelastic collisions of the incident electrons with electrons in discrete orbital of atoms in the sample. X-rays are fixed wavelength as the excited electrons return to lower energy states. Thus, characteristic X-rays are produced for each element

in a mineral that is excited by the electron beam. SEM analysis is considered to be non-destructive; that is, X-rays generated by electron interactions do not lead to volume loss of the sample, so it is possible to analyze the same materials repeatedly.

The SEM has many advantages over traditional microscopes. We describe it following:

- (1) It has large depth of field, which allows more of a specimen to be in focus at one time.
- (2) SEM has much higher resolution so closely spaced specimens can be magnified much higher levels.
- (3) Researcher has more control in the degree of magnification, because of the SEM uses electromagnets rather than lenses.

3.3.2 Atomic Force Microscopy (AFM)

Atomic force microscopy is a manner of measuring surface morphology on a scale from angstroms to 100 microns. The technique involves imaging a sample through the use of a probe or tip, with a radius of 20 nm. The tip is held several nanometers above the surface using a feedback mechanism that measures surface tip interactions. Variations in tip height are recorded while the tip is scanned repeatedly across the sample, producing a topographic image of the surface.

In addition to basic AFM, the instrument in the Microscopy Suite is capable of producing images in a number of other modes, including tapping, magnetic force, electrical force and pulsed force. In tapping mode, the tip is oscillated above the sample surface, and data may be

collected from interactions with surface morphology, stiffness and adhesion. This result in an expanded number of image contrast methods compared to basic AFM. Magnetic force mode imaging utilizes a magnetic tip to enable the visualization of magnetic domains on the sample. In electrical force mode imaging a charged tip is used to locate and record variations in surface charge. In pulsed force mode, the sample is oscillated beneath the tip, and a series of pseudo force distance curves are generated. This permits the separation of sample topography, stiffness, and adhesion values, producing three independent images, or three individual sets of data, simultaneously.

3.3.3 X-Ray Diffraction (XRD)

X-ray diffraction (XRD) is one of the most important techniques for qualitative and quantitative analysis of crystalline compounds. The XRD technique provides information includes types and nature of crystalline phase present structural makeup of phase, degree of crystallinity, amount of amorphous content which microstrain and size and orientation of crystallites.

When a sample is irradiated with a parallel beam of monochromatic X-ray, the atomic lattice of the sample acts as a three dimensional diffraction grating causing the X-ray beam to be diffracted to specific angles. The diffraction pattern that includes position (angles) and intensities of the diffracted beam that provides several types of information about the sample which are discussed below:

Angles are used to calculate the interplanar atomic spacing

(d-spacing). Because every crystalline material will give a characteristic diffraction pattern and can act as a unique “fingerprint”, the position “d” and intensity “I” information are used to identify the type of material by comparing them with patterns for over 80,000 data entries in the International Powder Diffraction File (PDF) database. Hence, identification of any crystalline compounds, even in a complex sample by XRD.

The position “d” of diffracted peaks also provides information about how the atoms are arranged within the crystalline compound (unit cell size or lattice parameter). The intensity information is used to assess the type and nature of atoms. Determination of lattice parameter helps understand extent of solid solution (complete or partial substitution of one element for another, as in some alloys) in a sample.

Width of the diffracted peaks is used to determine crystallite size and microstrain in the sample. The “d” and “I” from a phase can also be used to quantitatively estimate the amount of that phase in a multicomponent mixture. As mentioned earlier, XRD can be used not only for qualitative identification but also for quantitative estimation of various crystalline phases. This is one of the important advantages of the X-ray diffraction technique.

3.3.4 Photoluminescence (PL)

Photoluminescence spectroscopy is a contactless, nondestructive method of probing the electronic structure of materials. Light is directed onto a specimen, where it is absorbed and imparts excess energy into the

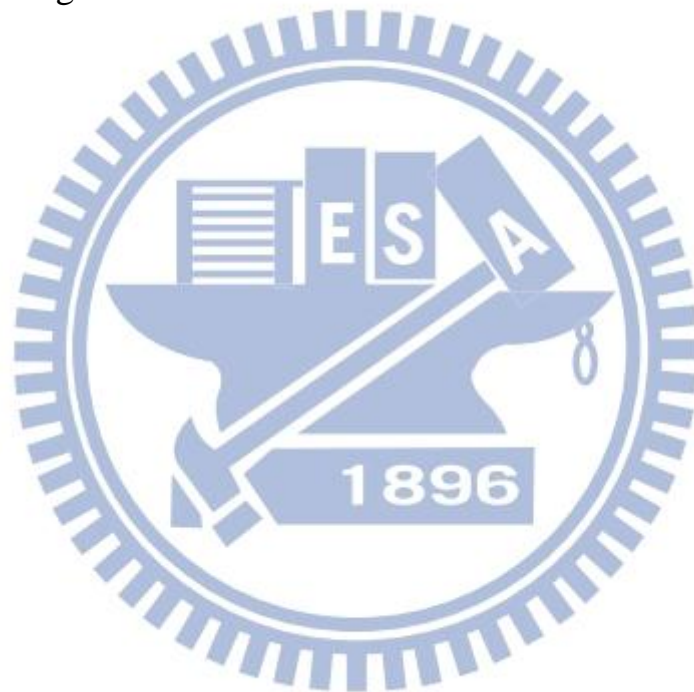
material in a process called photo-excitation. One manner this excess energy can be dissipated by the sample is through the emission of light, or luminescence. In the case of photo-excitation, this luminescence is called photoluminescence. The intensity and spectral content of this photoluminescence is a direct measure of various important material properties.

Photo-excitation causes electrons within the material to move into permissible excited states. When these electrons return to their equilibrium states, the excess energy is released and may include the emission of light or may not. The energy of the emitted light relates to the difference in energy levels between the two electron states involved in the transition between the excited state and the equilibrium state. The quantity of the emitted light is related to the relative contribution of the radiative process.

3.3.5 Extra Quantum Efficiency (EQE)

A solar cell's quantum efficiency value indicates the amount of current that the cell will produce when irradiated by photons of a particular wavelength. If the cell's quantum efficiency is integrated over the whole solar electromagnetic spectrum, one can evaluate the amount of current that the cell will produce when exposed to sunlight. The external quantum efficiency is the ratio of the number of charge carriers collected by the solar cell to the number of photons of a given energy incident photons. The external quantum efficiency therefore depends on both the absorption of light and the collection of charges. Once a photon has been

absorbed and has generated an electron-hole pair, these charges must be separated and collected at the junction. The ideal quantum efficiency graph has a square shape, where the QE value is fairly constant across the entire spectrum of wavelengths measured. The QE for most solar cells is reduced because of the effects of recombination, where charge carriers are not able to move into an external circuit. The quantum efficiency of solar cells can be seen as the absorptive ability of solar cells on a single wavelength of light.



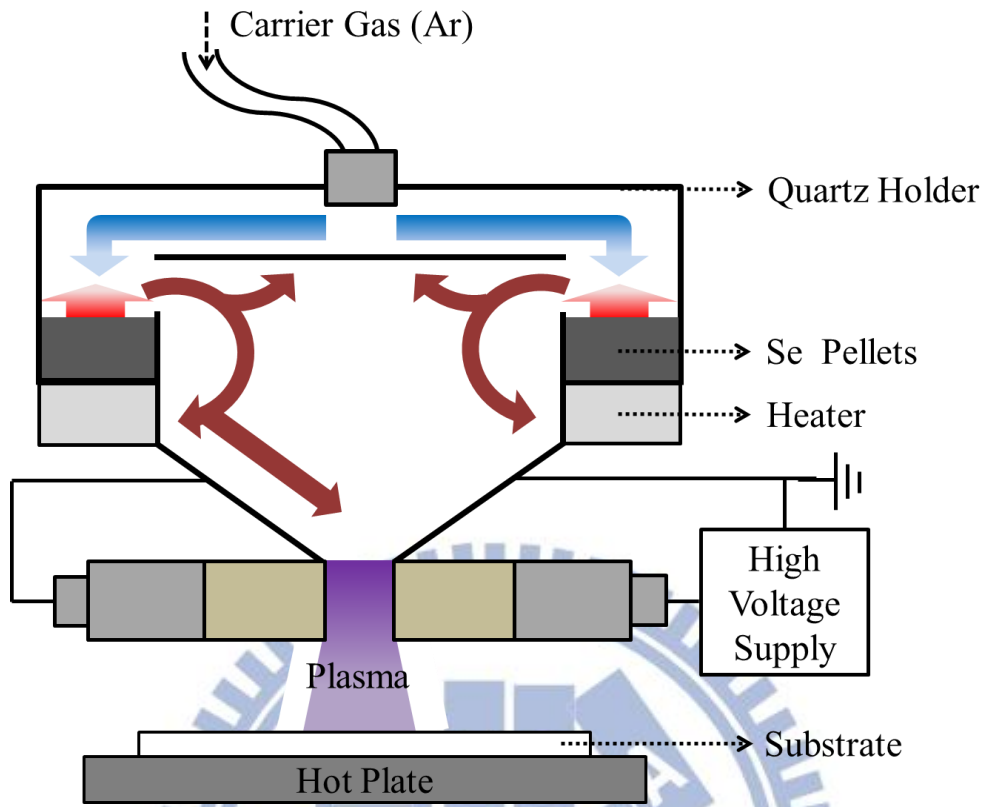


Figure 3-4 Schematic Illustration of Se Film Prepared with APPECVD.

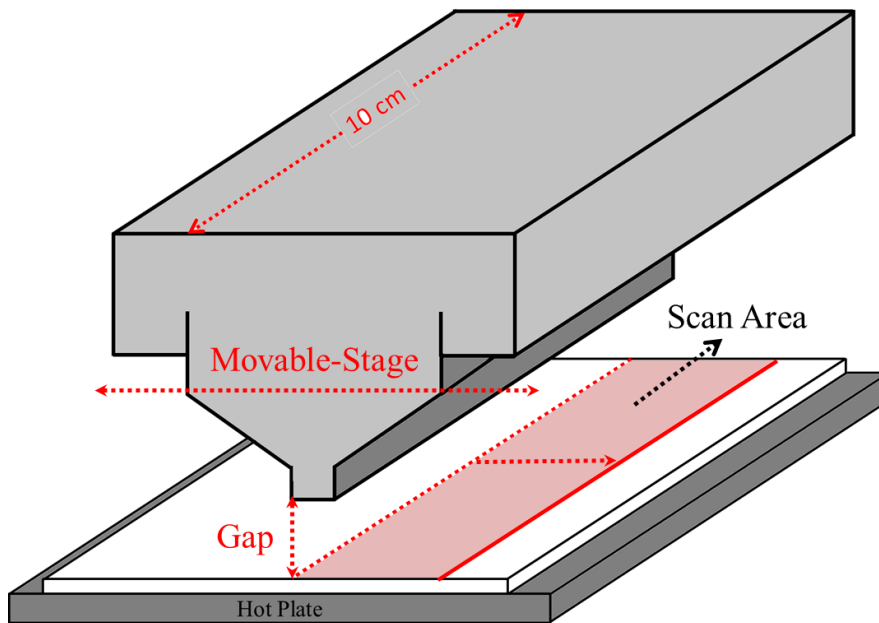


Figure 3-5 Schematic Illustration of Movable Mechanism of APPECVD.

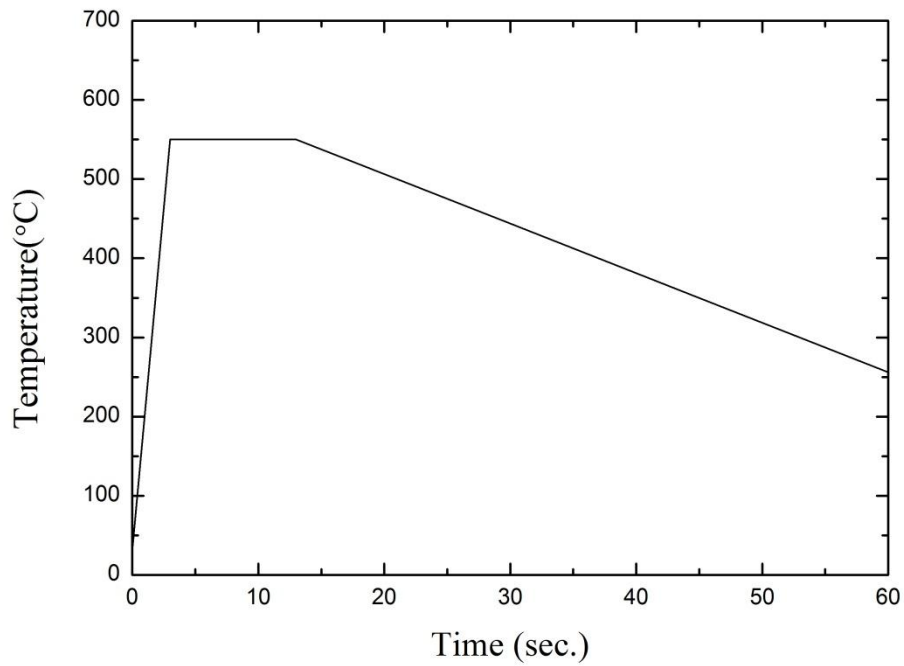


Figure 3-6 The Temperature Curve of RTP Process.

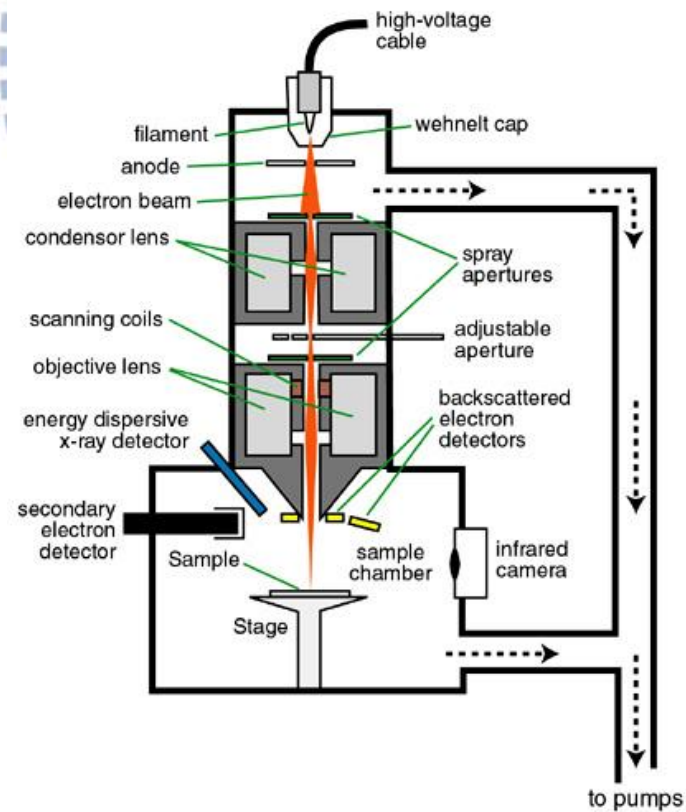


Figure 3-7 Schematic Illustration of SEM Instrument.[55]

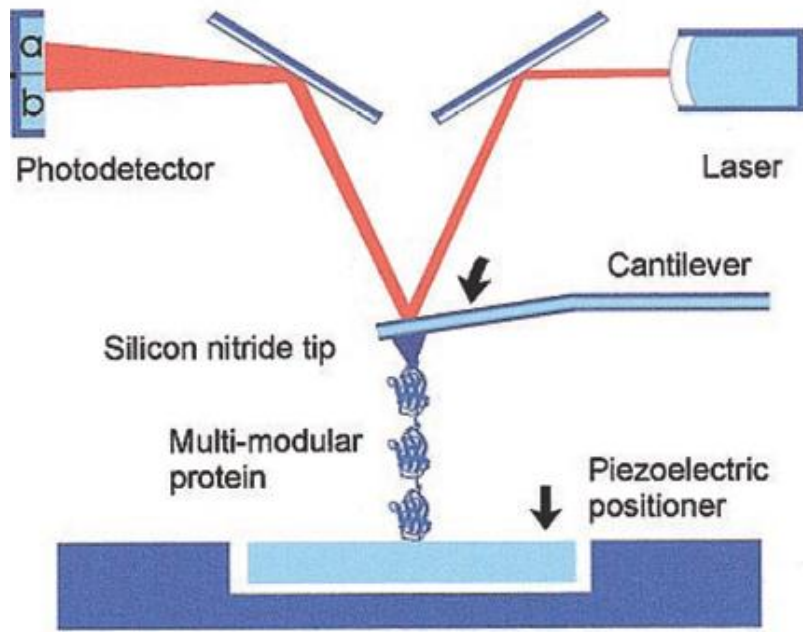


Figure 3-8 Schematic Illustration of AFM instrument.[56]

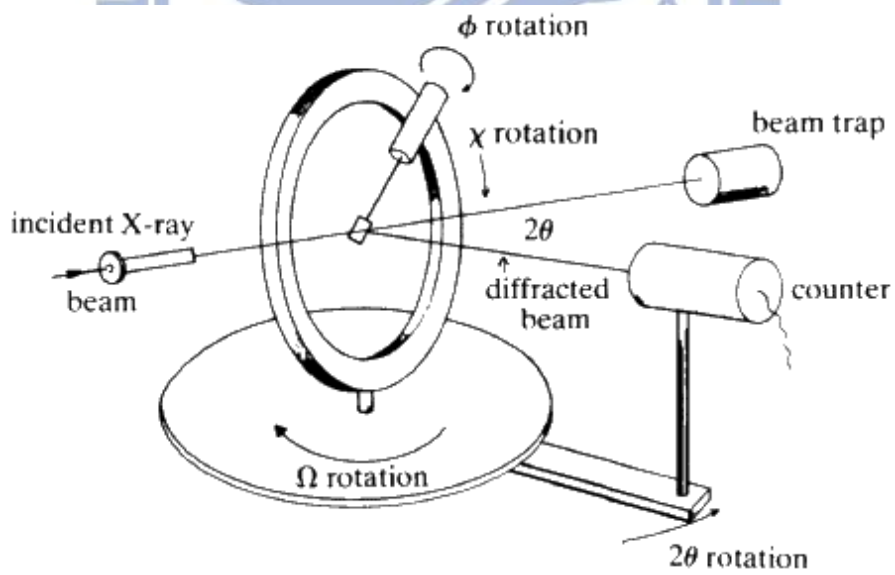


Figure 3-9 Schematic Illustration of XRD Instrument.[57]

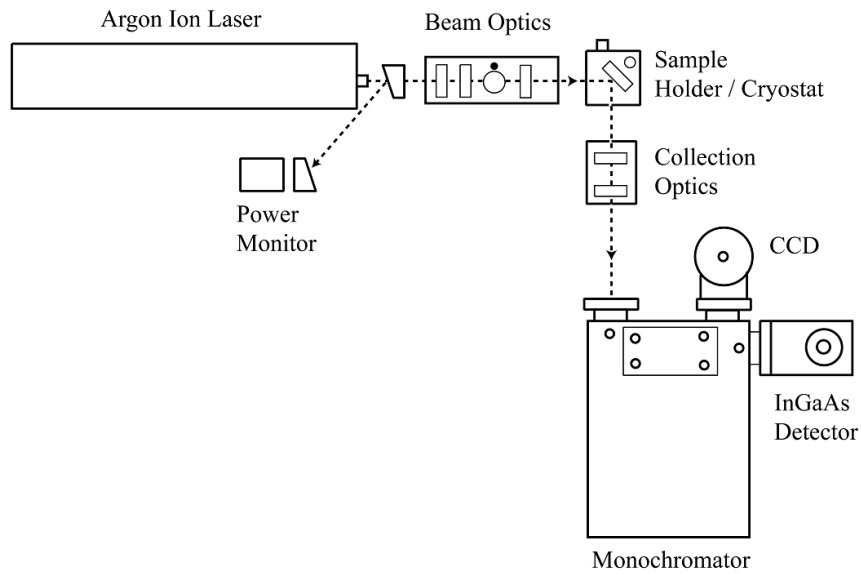


Figure 3-10 Schematic Illustration of PL Instrument.[58]

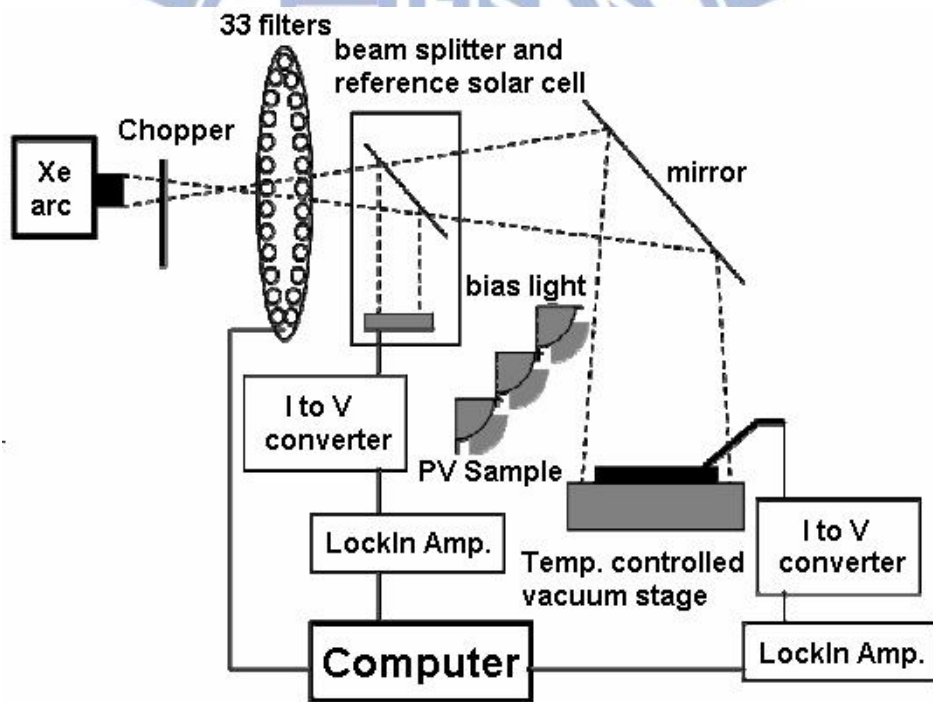


Figure 3-11 Schematic Illustration of EQE Instrument.

Table 3-1 Optimize the Fabrication Parameters for APPECVD.

Parameter	Value		
Power (Watt)	0	50	50, 60, 70
Selenium Temperature(°C)	325, 335, 345	345, 355, 365	355
Carrier Gas Flow Rate (SLM)	10, 15, 20	15, 20, 25	20
Background Pressure (Torr)	150, 350, 550		
Substrate Temperature (°C)	45		
Gap Distance (mm)	5		
Scan Times	50		
Scan Speed (mm/s)	10		

Table 3-2 Parameters of Selenium Film by APPECVD.

Parameter	Value
Power (Watt)	0, 50, 60 and 70
Substrate Temperature (°C)	45, 85 and 125
Gap Distance (mm)	5
	0W: 75
Scan Times	50W: 65
(thickness~2.5µm)	60W: 80
	70W: 100
Scan Speed (mm/s)	10
Carrier Gas Flow Rate (SLM)	20
Background Pressure (Torr)	150
Selenium Temperature (°C)	355

Chapter 4

Result and Discussion

In this chapter, we will discuss and explain the characterizations of selenium films in the different experiment, which include the selenium deposition on the glass, selenium deposition on the CIG precursor layer, and the CIGS films after selenization. The characterization of selenium films on the glass use the SEM to analysis surface morphology and film thickness in order to optimize the fabrication parameters. We use the SEM to analysis surface morphology and films thickness, and XRD to analysis degree of crystalline selenium for the selenium films on the CIG precursor layer. After selenization process, we use the XRD, Raman spectroscopy, Photoluminescence, SEM and AFM to analysis the characterization of CIGS films, which include surface morphology, films thickness, surface roughness, degree of crystalline CIGS chalcopyrite, secondary phase and band gap. Finally, the completion of the CIGS solar cell devices measure the I-V curve and Extra Quantum Efficiency in order to discuss the films quality affect device performance.

4.1 Optimize the Fabrication Parameters

4.1.1 Evaporation Deposition Selenium Films

The evaporation deposition selenium films represent “without plasma”, so we discuss three different parameters, included Se source temperature, main gas flow rate and background pressure in order to find the optimal parameter for this equipment.

The different Se source temperatures are 325°C, 335°C and 345°C, respectively. The Se source temperature is more and higher and the selenium film is more and more thick show in SEM top-view images of Table 4-1 due to increase the vapor pressure of Se. Though the deposition rate is more and higher, but surface become more and more rough show in SEM top view images of Table 4-1. Therefore we choose the befitting Se source temperature (335°C). The different main gas flow rate is 5SLM, 10SLM and 15SLM, respectively. The main gas flow rate is more and higher, the film is more and thinner. Because the main gas flow rate is increase, result in time of selenium molecular deposition on the glass substrate from the APPECVD become short. Additionally, flow rate cannot too small and result in the number of main gas carries selenium molecular to out chamber is decrease. We will decide a befitting main gas flow rate (10SLM); this parameter has a high deposition rate. The above mentioned parameters and results show in the Table 4-2. Finally, we determine the background pressure, based on the amount of the composition of the background such as concentration of oxygen and carbon. Therefore we choose the lowest background pressure (150torr) that has the lowest concentration of oxygen. The above mentioned

parameters and results show in the

Table 4-3.

4.1.2 Plasma Enhance Deposition Selenium Films

We discuss four different parameters, which include Se source temperature, main gas flow rate, background pressure and plasma power in order to find the optimal parameter for this equipment. Additionally the parameter of plasma power is tested the film thickness in order to estimate the film thickness to reach over $2.5\mu\text{m}$ (thickness of selenium film was between three and four fold of thickness of precursor layer by selenization) [59].

The different Se source temperatures were 345°C , 355°C and 365°C , respectively. The Se source temperature is more and higher and the selenium film is more and more thick show in SEM cross-section images of

Table 4-5 due to increase the vapor pressure of Se. Though the deposition rate is more and higher, but surface become more and more rough show in SEM top view images of

Table 4-5. Therefore we choose the befitting Se source temperature (335°C). The different main gas flow rates were 15SLM, 20SLM and 25SLM, respectively. The main gas flow rate is more and higher, and the film is more and thinner. Because the main gas flow rate is increase, result in time of selenium

molecular deposition on the glass substrate from the APPECVD become short and the surface is smoother show in

Table 4-5. Additionally, compare the flow rate 15SLM and 20SLM, we can find the significant rough surface for the flow rate is decrease. Therefore we choose 20SLM to be the flow rate of the optimal parameter. The above mentioned parameters and results are show in

Table 4-6. Finally, we determine the background pressure, based on the amount of the composition of the background such as concentration of oxygen and carbon. Therefore we choose the lowest background pressure (150torr) that has the lowest concentration of oxygen. And then the background pressure is decrease, result in selenium vapor pressure are raised because the melt point is decrease with decrease of background pressure. The above mentioned parameters and results are show in the

Table 4-6.

According to the data of Table 4-7, the plasma power 50W, 60W and 70W will respectively estimate the scan times of over 2.5 μ m. And then the scan times are 65, 80 and 100, respectively. These parameters are used to fabricate the CIGS thin film.

4.2 Investigation of Selenium Films on CIG layer Before Selenization

4.2.1 In/Cu₃Ga/Mo/Glass Precursor Layer

Figure 4-1 shows SEM cross-section images of deposited In/Cu₃Ga film on the Mo/SLG by sputtering. SEM cross-section images can estimate thickness of different stack film, so actual thickness of In, Cu₃Ga and Mo film are 394 nm, 198 nm and 384 nm, respectively. The peak of Cu₃Ga and In are observed the strongest in the spectrum. We can see the

γ 1-phase which is believed to be a $\text{Cu}_9\text{In}_4\text{-Cu}_9\text{Ga}_4$ alloy, which exist after precursor annealing [60-61]. The chemical compositions of the CIG precursor layer are 43.22 at% Cu, 43.22 at% In and 13.46 at% Ga by Energy Dispersive Spectrometer (EDS).

4.2.2 Selenium Films Deposition on CIG precursor Layer

Figure 4-3 shows SEM top view images of different plasma power. Apparently, surface of selenium film are more and smoother due to increased plasma power. The selenium molecules of vapor are dissociated by the plasma, which is the reason of different surface morphology, so the size of selenium molecules change small due to increased plasma power. The selenium films become dense when the plasma power is increase. We use SEM cross-section to confirm thickness of selenium films of different plasma power, these thicknesses will show in Table 4-8 and exceed $2.5\mu\text{m}$. Figure 4-4 shows AFM images of different plasma power and these AFM images can find the surface morphology and measure the RMS roughness. The trend of AFM measurement match with the SEM top view images and RMS roughness show in Table 4-8.

Figure 4-5 shows GIXRD spectrum of the selenium film of different plasma power. The GIXRD spectrum of without plasma find the (100) peak of crystalline selenium (peak position: 23.875°) due to the selenium source temperature as high as 335°C and the distance between heater and substrate is too small. Therefore the surface of selenium film of without plasma can find a little crystalline selenium. We dissociate the selenium vapor by atmosphere plasma and cause to more amorphous selenium film than without plasma, so the GIXRD spectrum with plasma cannot find the

(100) peak of crystalline selenium. When increase the plasma power, the FWHM of (101) peak of crystalline selenium (peak position: 30.14°) is more and higher. The gradually increase plasma power and will lead to increase the probability of plasma arc to substrate, and re-crystallize selenium films.

Figure 4-6 shows SEM top-view images of selenium films of different substrate temperature. Apparently, the selenium films with heating substrate have different surface morphology because the substrate temperature provides enough energy to crystallize. So the crystalline selenium films are more roughness than amorphous selenium films at low temperature (45°C). We use AFM to demonstrate the result of SEM top-view images, show in Figure 4-7. When increase the substrate temperature, the surface RMS roughness will increase, on the other hand produce more crystalline selenium films. The result of SEM and AFM shows in Table 4-9.

Figure 4-8 shows GIXRD spectrum of the selenium film of different substrate temperature. The (101) peak of selenium will increase at high substrate temperature (125°C), and the (100) peak of selenium will decrease with increased substrate temperature [62]. We can compare room temperature with high temperature and find the significantly crystalline selenium.

4.3 Investigation of Cu(In,Ga)Se₂ Films After Selenization

4.3.1 The Interface between CIGS and Mo

Figure 4-9 and Figure 4-15 shows SEM cross-section images of CIGS films of different plasma power and substrate temperature. We can find the MoSe₂ between CIGS absorber layer and Mo from the cross-section images of different parameters. The MoSe₂ layers assist CIGS/Mo to change Ohmic-type contact, which is better than Schottky-type contact of without MoSe₂. The Ohmic-type contact can improve leakage current of solar cell [63]. Additionally, not only improve the electric properties but also improve adhesion strength of CIGS to Mo, because the orientation of MoSe₂ is perpendicular to the Mo surface. Figure 4-12 and Figure 4-18 shows GIXRD spectrum of CIGS thin films of different plasma power and substrate temperature. We can find (100) and (110) peak of MoSe₂, which is perpendicular to the Mo surface. Though, thickness of MoSe₂ layers of different parameters is different, but the orientation of MoSe₂ is more important than its thickness [64].

4.3.2 Cu(In,Ga)Se₂ Films of Different Plasma Power

The sample of without plasma is denser than with plasma and the surface roughness of without plasma is smoother than with plasma in the Figure 4-10. The sample of without plasma has less void and smoother surface because the selenium thin films have some crystallization. The crystalline selenium gets more pre-diffusion time than amorphous selenium because diffusion coefficient of amorphous selenium is far larger than crystalline selenium. Therefore, the element In and Ga

inter-diffusion in the time of pre-diffusion. The surface roughness is decreased with increased plasma power due to crystalline selenium film. We use AFM to measure surface roughness show in the Figure 4-11 and this data can demonstrate above mentioned.

The GIXRD spectrum is show in the Figure 4-12. In the figure, the CGS peak gradually increases with increased the plasma power, which is CGS separable phase, because the sample of without plasma have a little crystalline selenium. These crystalline selenium have more diffusion time cause to more uniform Cu(In,Ga)Se₂ thin films. So the sample of without plasma has less CGS peak than 50W, 60W and 70W show in Figure 4-12. Figure 4-13 shows representative peak position for (112) peak of different plasma power. According to other paper, (112) peak position will increase with increased the Ga concentration (Ga/III). Because the atom radius of indium is larger gallium, so the lattice constants will decrease and increase peak position (2θ) of XRD as incorporation of the gallium element in the indium sites. The (112) peak position is 26.665° for Ga concentration is 0% and 27.769° for Ga concentration is 100%. So the trend of (112) peak position is the same trend of Ga concentration and the Ga concentration of with plasma is smaller than without plasma because consume Ga to generate the CIG separable phase. We use EDS to measure the element composition of CIGS thin films, which are depicted in Table 4-11. The trend of Ga concentration with plasma power is the same GIXRD spectrum. The FWHM for (112) peak of CIGS thin films of plasma power are depicted in Figure 4-14, and the FWHM represent degree of crystallization of CIGS films. From this figure, the FWHM is

decreased with increased the plasma power, but too high plasma power will critically damage the surface. And then we can see the sample of without plasma (0W) is larger than other sample because distort the normal lattice structure of CuInSe_2 as the incorporation of the gallium element in the indium sites. Thickness of CIGS/MoSe₂/Mo/Glass sample and RMS roughness of CIGS thin films are show in Table 4-10.

4.3.3 Cu(In,Ga)Se_2 Films of Different Substrate Temperature

Figure 4-15 shows the SEM cross-section images of different substrate temperature. The CIGS thin film of 85°C has many voids below the CIGS thin film. The voids influence film quality and cause to worst contact to back electrode. The reason may be the intensity of crystalline orientation (100) and (101) of selenium are same strength, cause to mismatch the lattice structure. The SEM top-view images are more and smoother with increased substrate temperature in Figure 4-16 because the crystalline selenium thin films need more time to dissociate. The results of AFM measurement is surface morphology and roughness show in Figure 4-17 and Table 4-12, which match trend of SEM top-view.

The GIXRD spectrum is show in the Figure 4-18. In the figure, the CGS peak gradually decreases with increased the substrate temperature, which is CIG separable phase. The crystalline selenium get more pre-diffusion time than amorphous selenium because diffusion coefficient of amorphous selenium is far larger than crystalline selenium. These crystalline selenium have more diffusion time cause to more uniform Cu(In,Ga)Se_2 thin films. So the CGS peak will disappear at high substrate temperature. Therefore, the Ga concentration of CIGS thin films

gradually increases with increase substrate temperature. Additionally, the (112) peak position of CIGS thin films is more and larger with substrate temperature is more and higher show in Figure 4-19. The element compositions of EDS also appear this trend show in Table 4-13. We use the FWHM of (112) peak to determine the films quality of CIGS show in Figure 4-20. We can find the films quality of CIGS is more and worse with increased substrate temperature. The reason may be the (101) peak of selenium gradually increase with increase substrate temperature.

Figure 4-21 is show the depth analysis of Auger electron spectroscopy which is prepared with different substrate temperature, and we can find the Ga distributed concentration is more uniform with increased substrate temperature. The crystalline selenium thin films can cause to have much pre-diffusion time, so In and Ga element can uniformly diffuse in selenization process. In this figure can find the Se single to penetrate in the raised Mo single, which represent the MoSe_2 layer is observed between Mo layer and Cu(In,Ga)Se_2 . Additionally, the Se single penetrate in the Mo single, which is decreased with increased substrate temperature. The result may be due to different crystallization of selenium thin film on the CIG precursor layer have different diffusion coefficient.

4.3.4 The Electric Properties of Solar Cell Device of Cu(In,Ga)Se_2

Figure 4-22 compares the I-V curve for different plasma power. Obviously, the short-circuit current of plasma power 60W is larger than without plasma and open-circuit voltage has insignificant difference. But the conversion efficiency of plasma power 60W slightly improves

compares to without plasma due to the effect of fill factor. The fill factor will change by the series-resistance and shunt-resistance. The shunt-resistance of without plasma is far larger compare to with plasma power 60W and series-resistance of without plasma insignificant difference compare to with plasma 60W show in Table 4-12. The difference of the shunt-resistance relates to leakage current and leakage current is increased with decreased shunt-resistance. In the Figure 4-23, we can find the quantum efficiency of sample of plasma power 60W is the highest compare to sample of different plasma power. And the short-circuit current of AM1.5G is given by

$$J_{sc,AM1.5g} = \int_{\lambda=0}^{\infty} G_{\lambda}(\lambda)QE(\lambda)d\lambda \quad (4-1)$$

, where G_{λ} is the spectral irradiance according to a reference distribution like the most commonly used AM 1.5. The short-circuit current of AM1.5G can decide a part of short-circuit current. Therefore, this is why the sample of plasma power 60W has the highest short-circuit current because the quality of absorption layer is better than without plasma.

The I-V curve of sample of different substrate temperature show in Figure 4-24. We can find open-circuit voltage, short-circuit current and fill factor at high substrate temperature (125°C) are higher than low substrate temperature. The reason of different open-circuit voltage may be the Ga concentration, and the Ga concentration is increased with increased substrate temperature. The band gap of CIGS absorption layer is increased with increase Ga concentration, which cause to open-circuit voltage is larger. Figure 4-25 shows EQE measurement of the CIGS solar cells prepared with different substrate temperature. Obviously, the

quantum efficiency of high substrate temperature (125°C) is higher than other sample in all region of wavelength. According to the function of (4.1), the short-circuit current is larger than other sample due to the quantum efficiency. Moreover, the quantum efficiency is the lowest among these curves, which substrate temperature is 85°C. This reason is the poor contact between Mo and CIGS absorption because the CIGS films generate many voids in the selenization process. We arrange these data of substrate temperature show in Table 4-14. We can find the conversion efficiency of high substrate temperature is larger compare to other sample. Because the roughness and film uniform of high substrate temperature are better than other sample, and cause to the coverage by buffer layer (CdS) is integral. The buffer layer is deposited on the CIGS absorption layer in order to avoid damaging the CIGS surface and producing the defect, possibly formed by sputtering of ZnO films. So the conversion efficiency may be increased with increased coverage of the buffer layer.

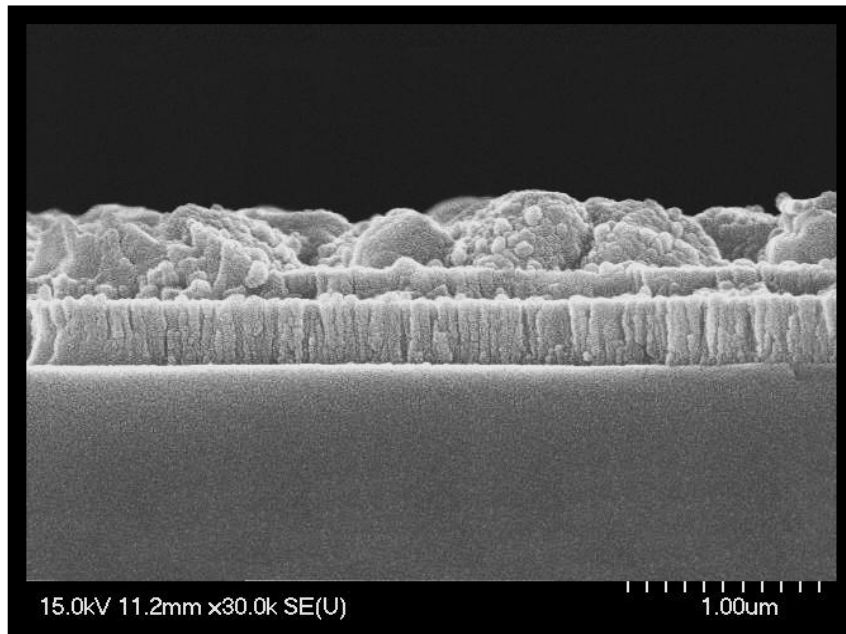


Figure 4-1 SEM cross-section images of deposited In/Cu₃Ga film on the Mo/SLG by sputtering.

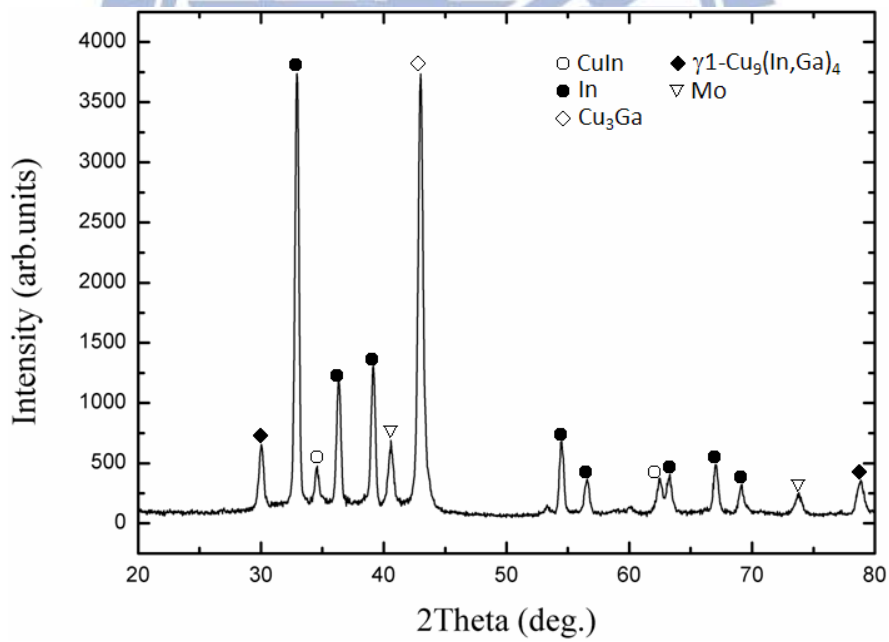


Figure 4-2 GIXRD spectrum of deposited In/Cu₃Ga on the Mo/SLG by sputtering.

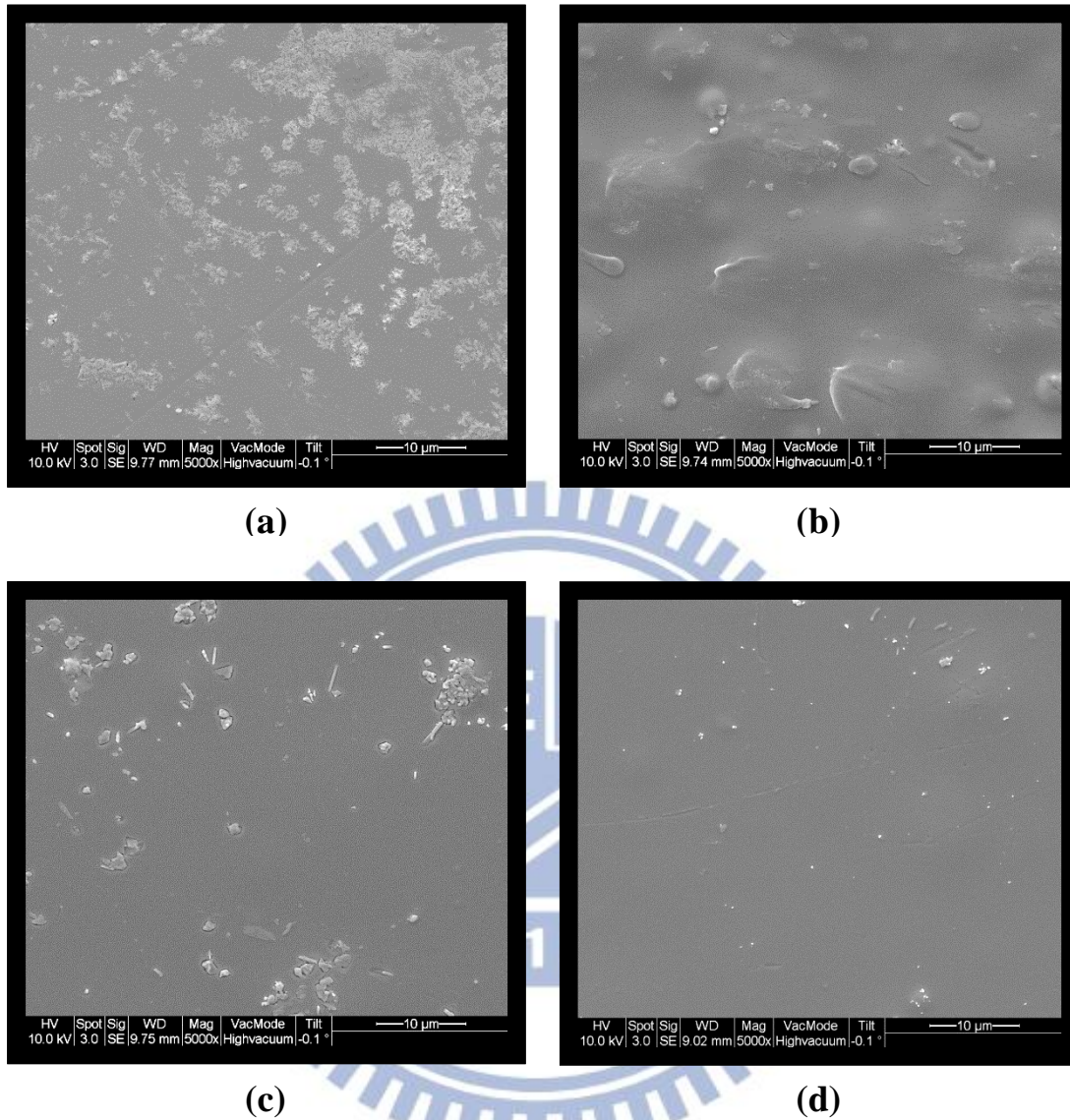


Figure 4-3 SEM top-view images of deposited selenium on the CIG precursor layer by APPECVD prepared with different plasma power (a) without plasma (b) 50W (c) 60W (d) 70W.

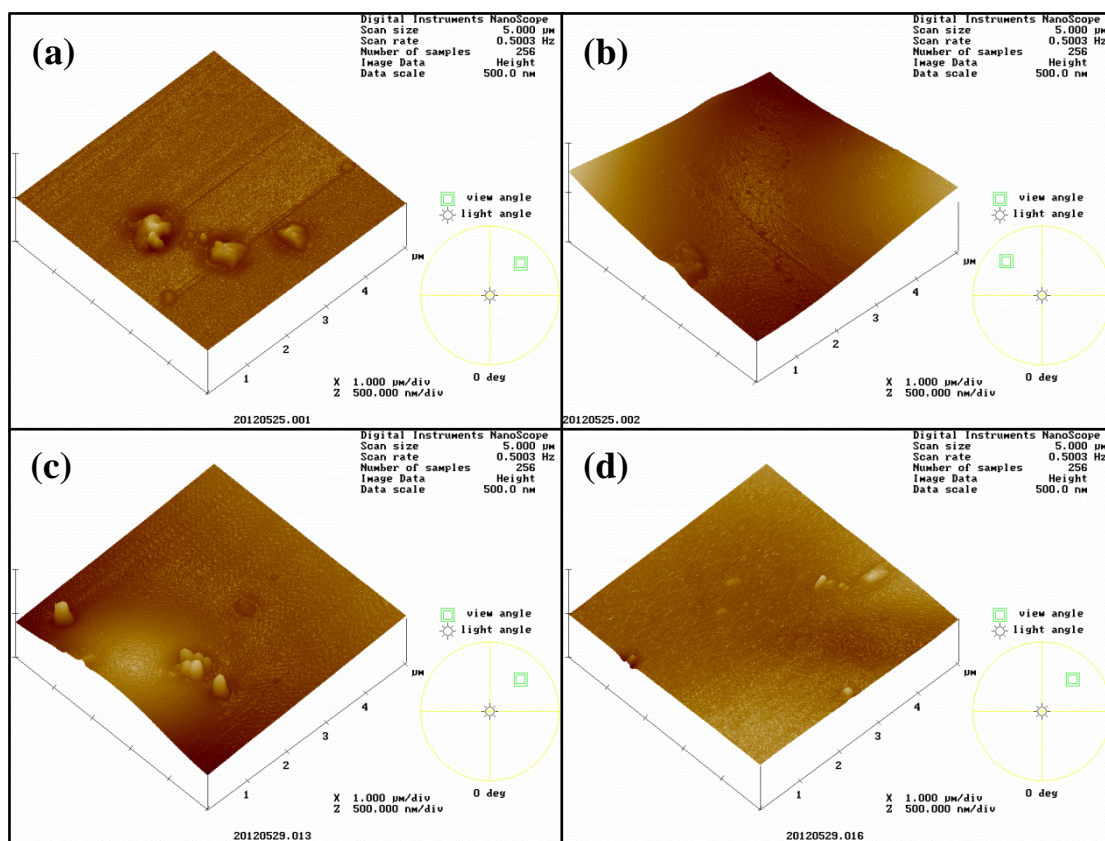


Figure 4-4 AFM images of deposited selenium on the CIG precursor layer by APPECVD prepared with different plasma power (a) without plasma (b) 50W (c) 60W (d) 70W.

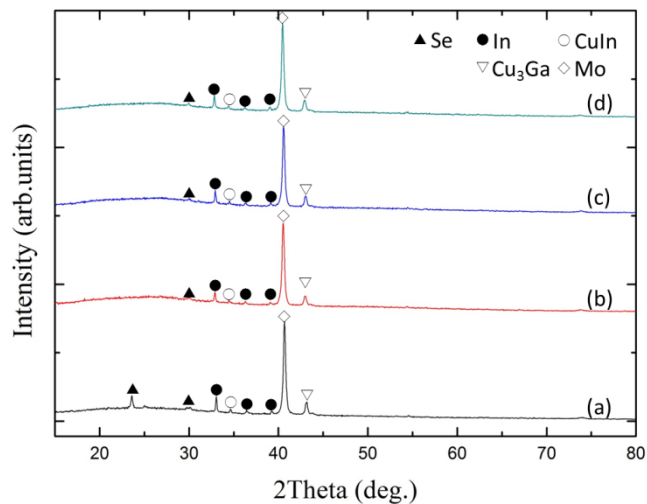


Figure 4-5 GIXRD spectrum of deposited selenium on the CIG precursor layer by APPECVD prepared with different plasma power (a) without plasma (b) 50W (c) 60W (d) 70W.

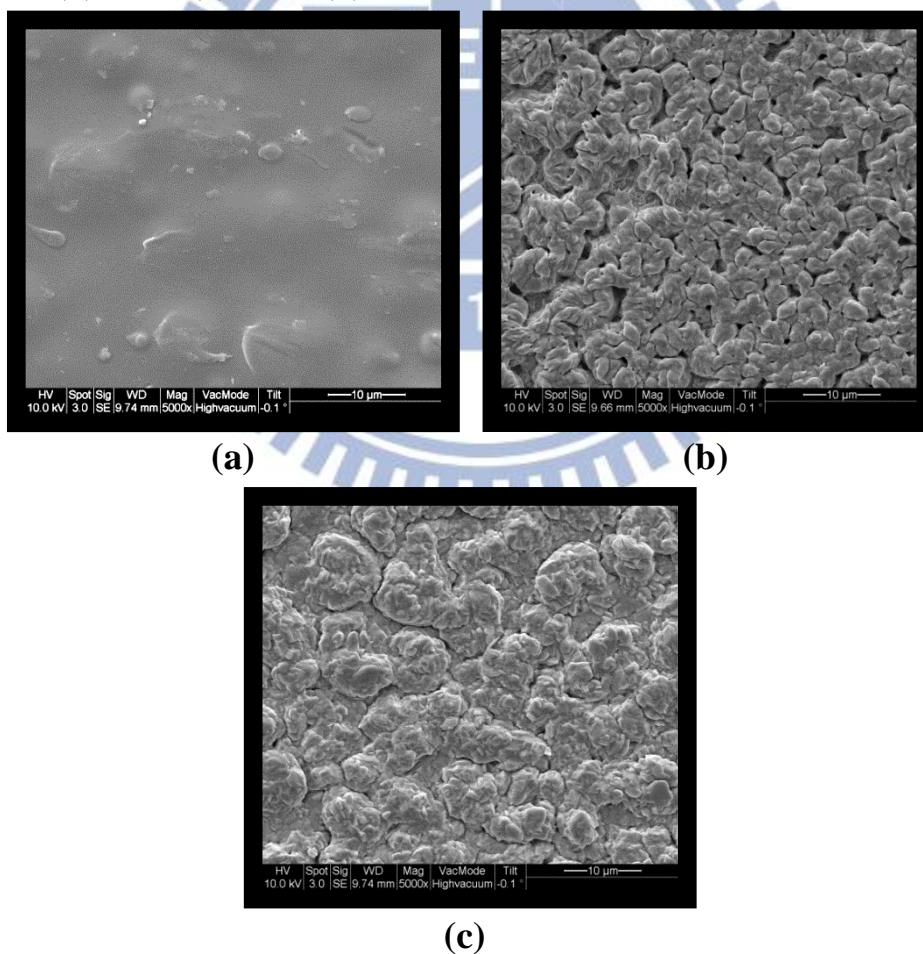


Figure 4-6 SEM top-view images of selenium film of different substrate temperatures (a) 45°C (b) 85°C (c) 125°C.

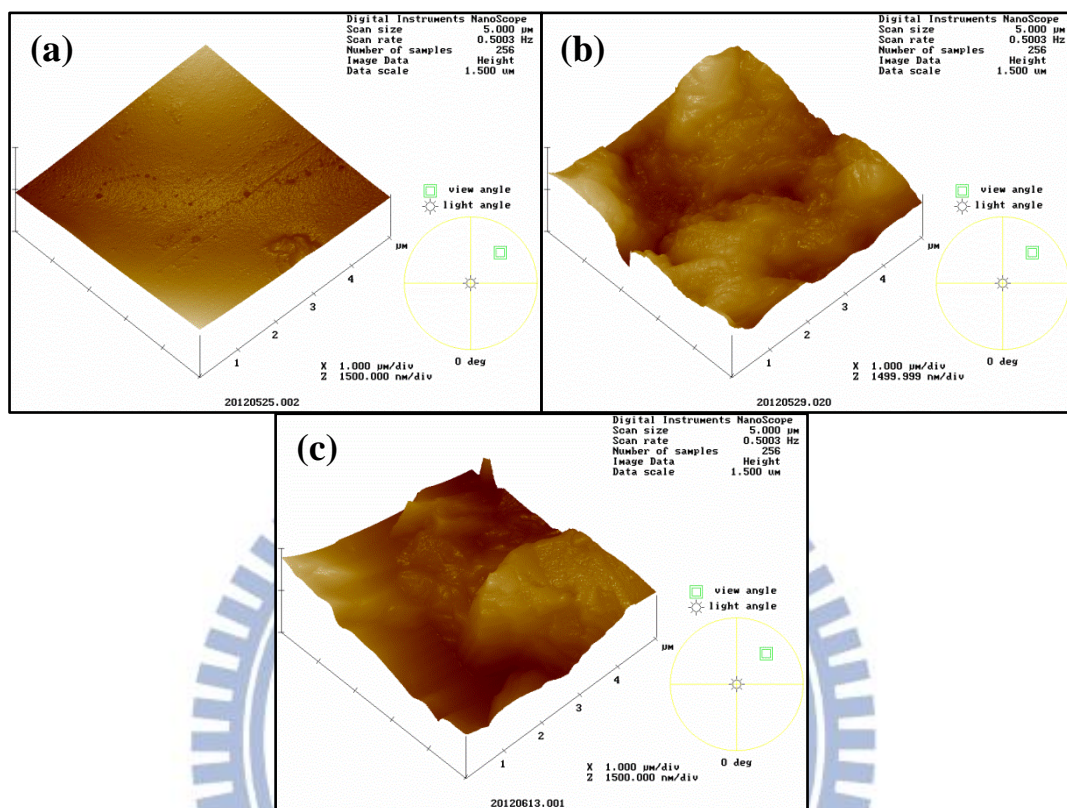


Figure 4-7 AFM images of deposited selenium on the CIG precursor layer by APPECVD prepared with different substrate temperature (a) 45°C (b) 85°C (c) 125°C.

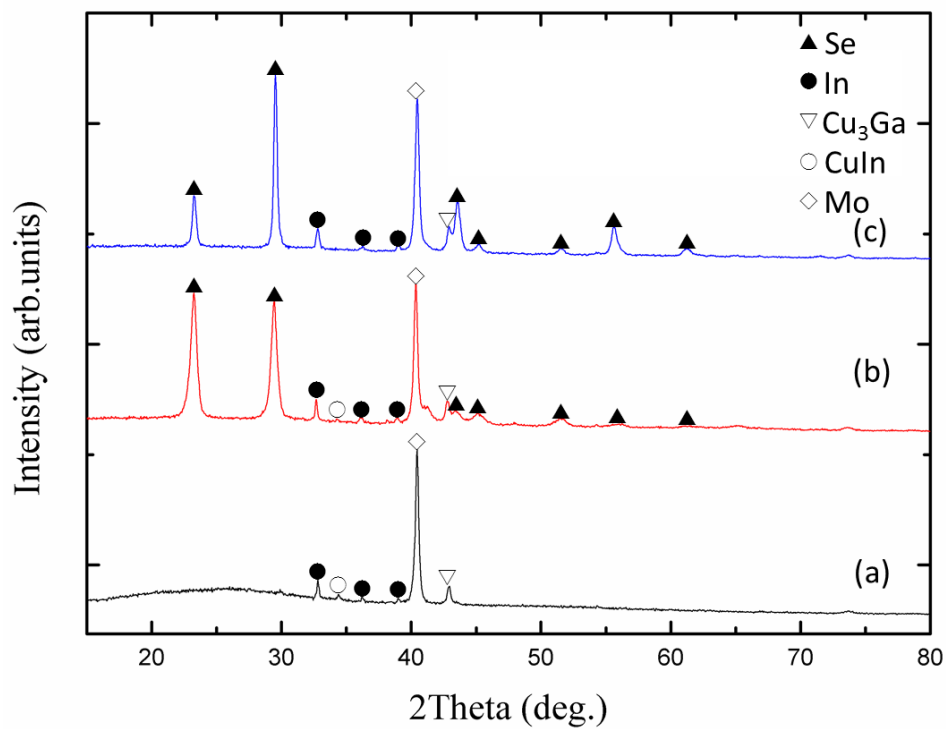


Figure 4-8 GIXRD spectrum of deposited selenium on the CIG precursor layer by APPECVD prepared with different substrate temperature (a) 45°C (b) 85°C (c) 125°C.

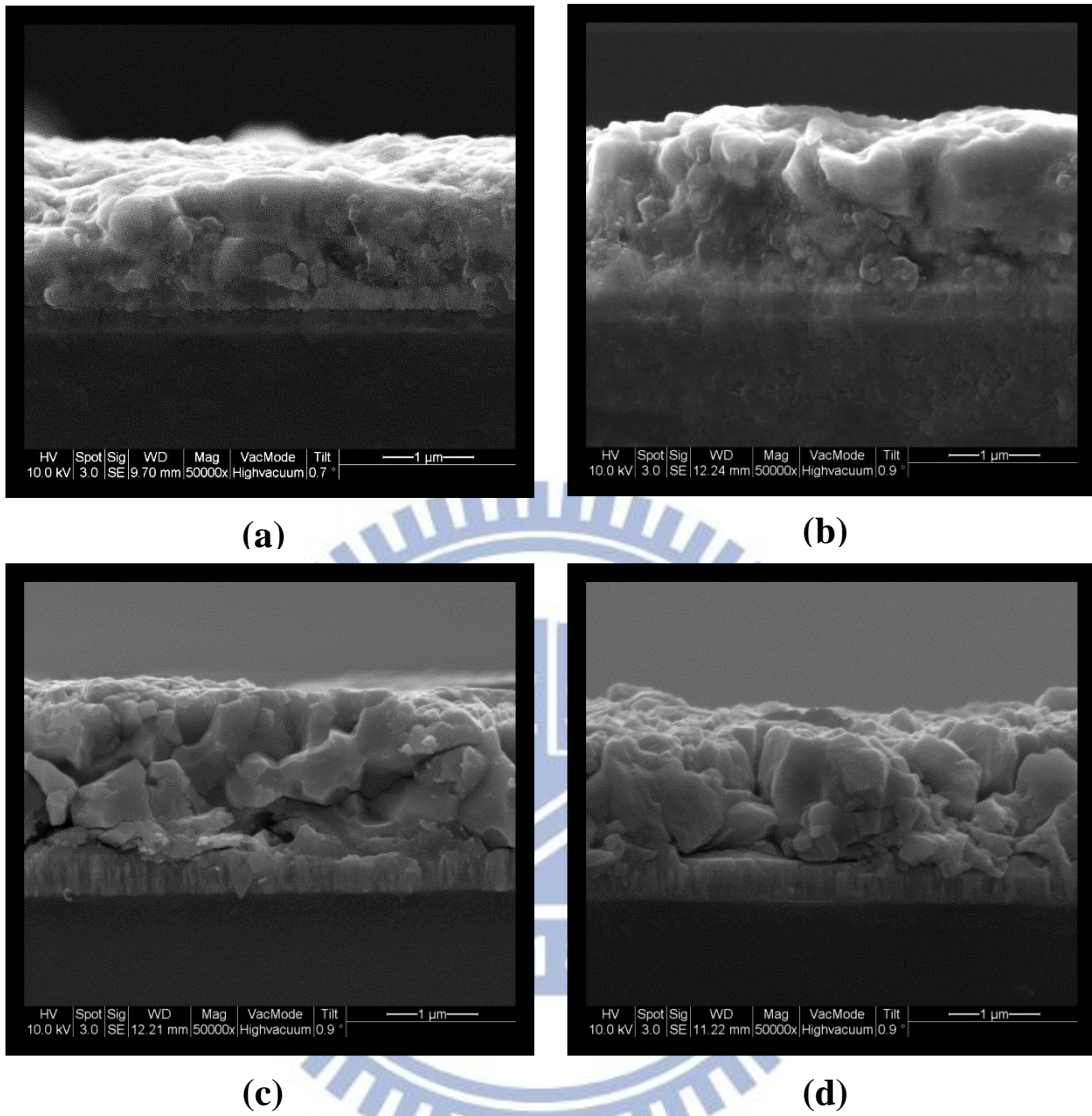


Figure 4-9 SEM cross-section images of CIGS thin films prepared with different plasma power (a) without plasma (b) 50W (c) 60W (d) 70W.

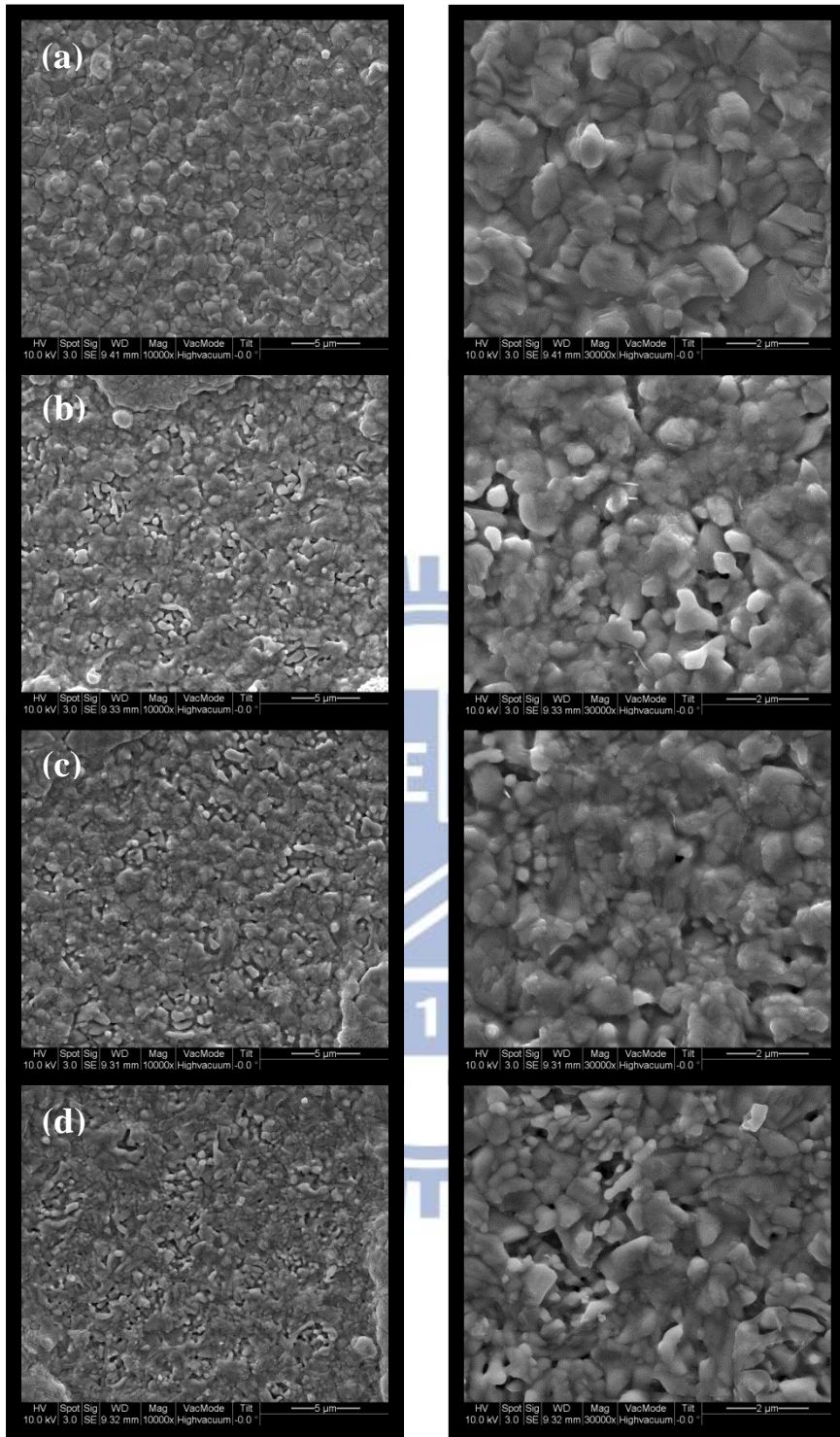


Figure 4-10 SEM top-view images of CIGS thin films prepared with different plasma power (a) without plasma (b) 50W (c) 60W (d) 70W. (The part of right half was 10K magnification images; the part of left half was 30K magnification images)

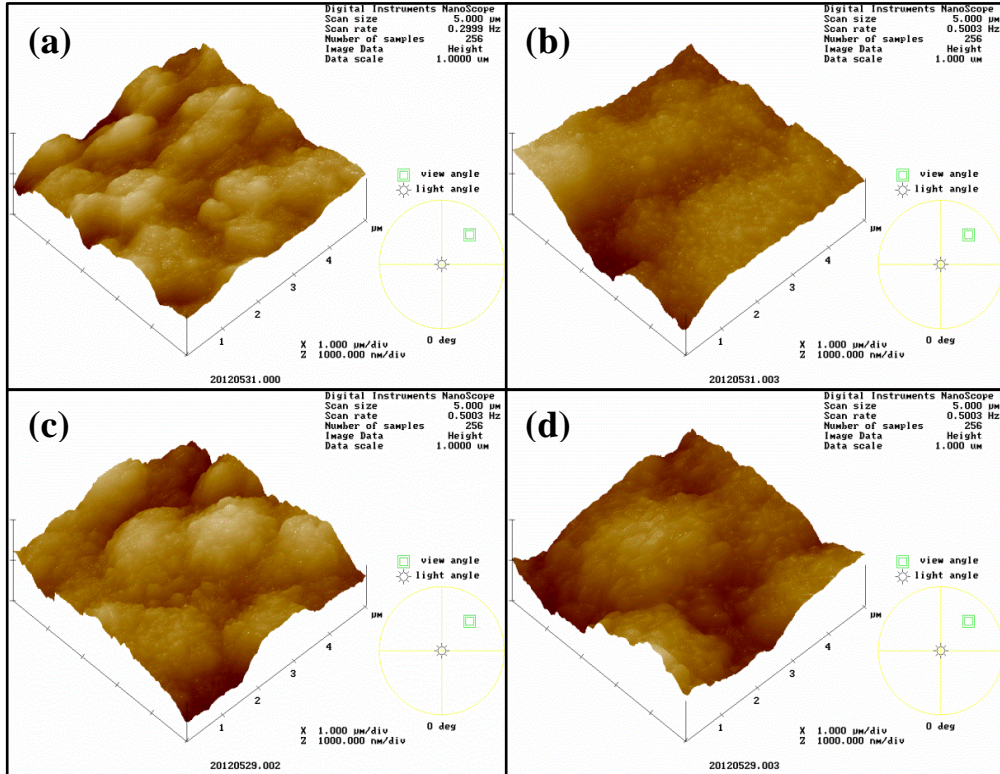


Figure 4-11 AFM images of CIGS thin films prepared with different plasma power (a) without plasma (b) 50W (c) 60W (d) 70W.

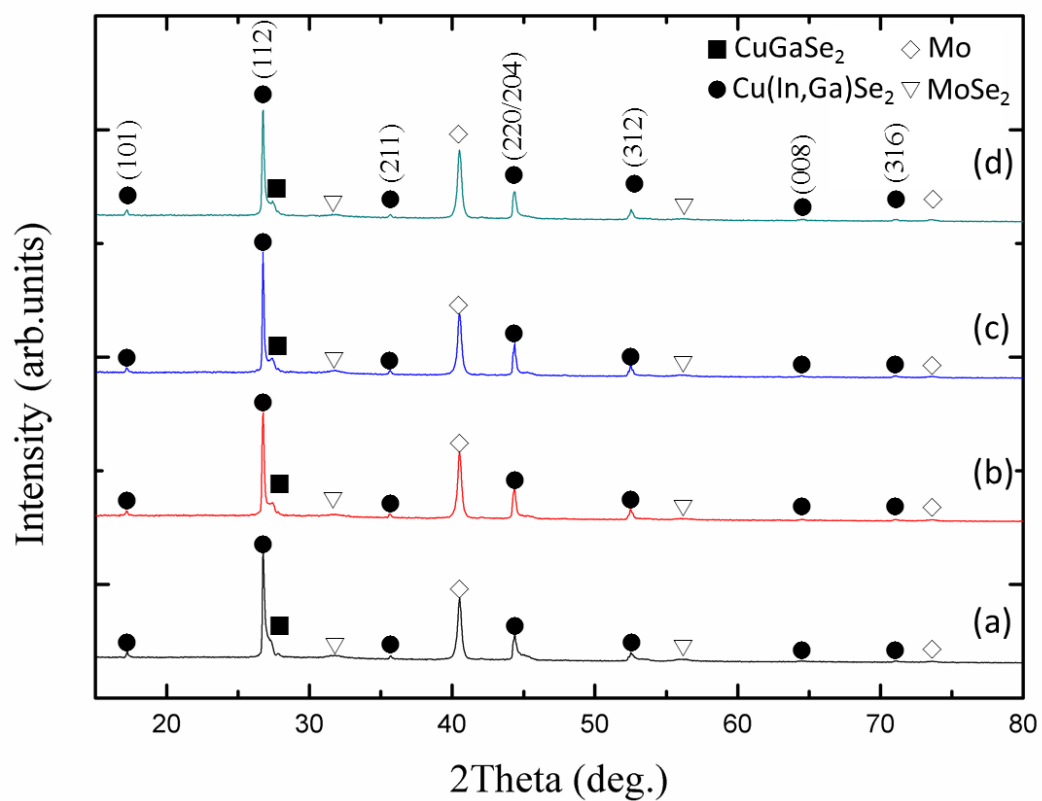


Figure 4-12 GIXRD spectrum of CIGS thin films prepared with different plasma power (a) without plasma (b) 50W (c) 60W (d) 70W.

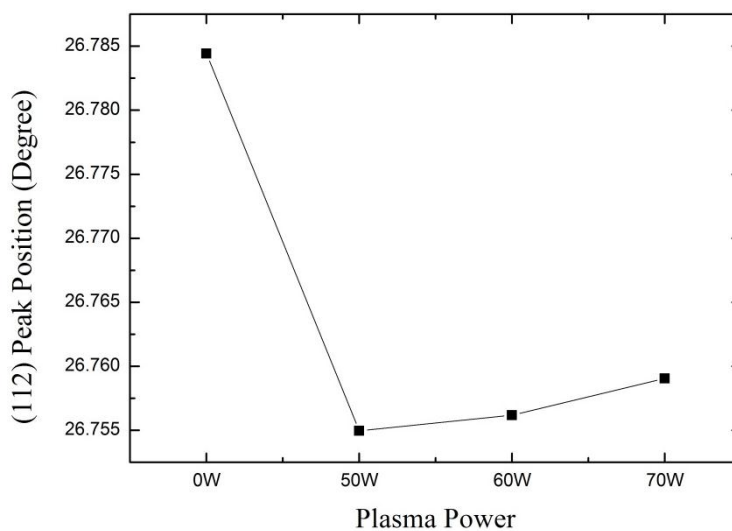


Figure 4-13 Variation of the peak position (2θ) for (112) peak of CIGS thin films with different plasma power.

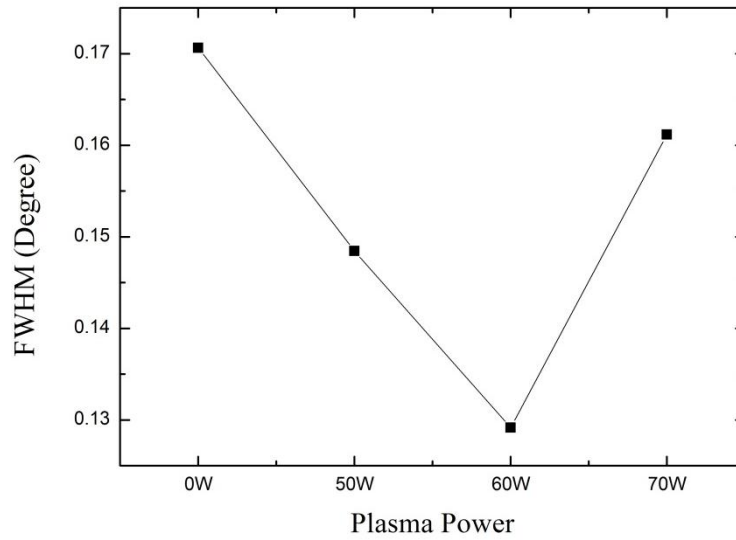


Figure 4-14 Variation of the FWHM for (112) peak of CIGS thin films with different plasma power.

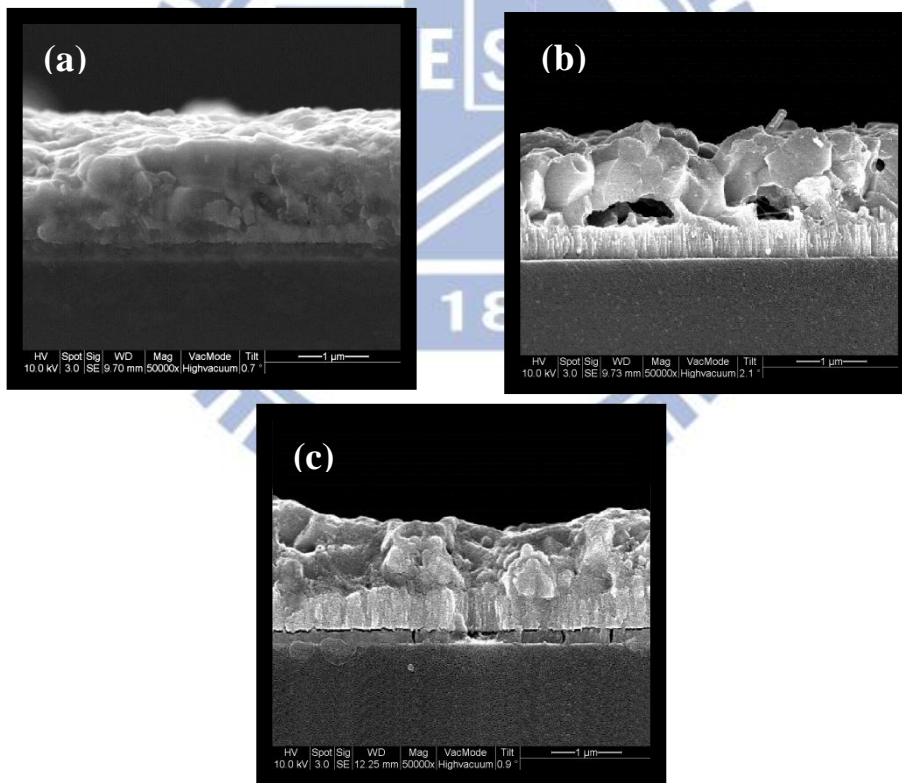


Figure 4-15 SEM cross-section images of CIGS thin films prepared with different substrate temperature (a) 45°C (b) 85°C (c) 125°C.

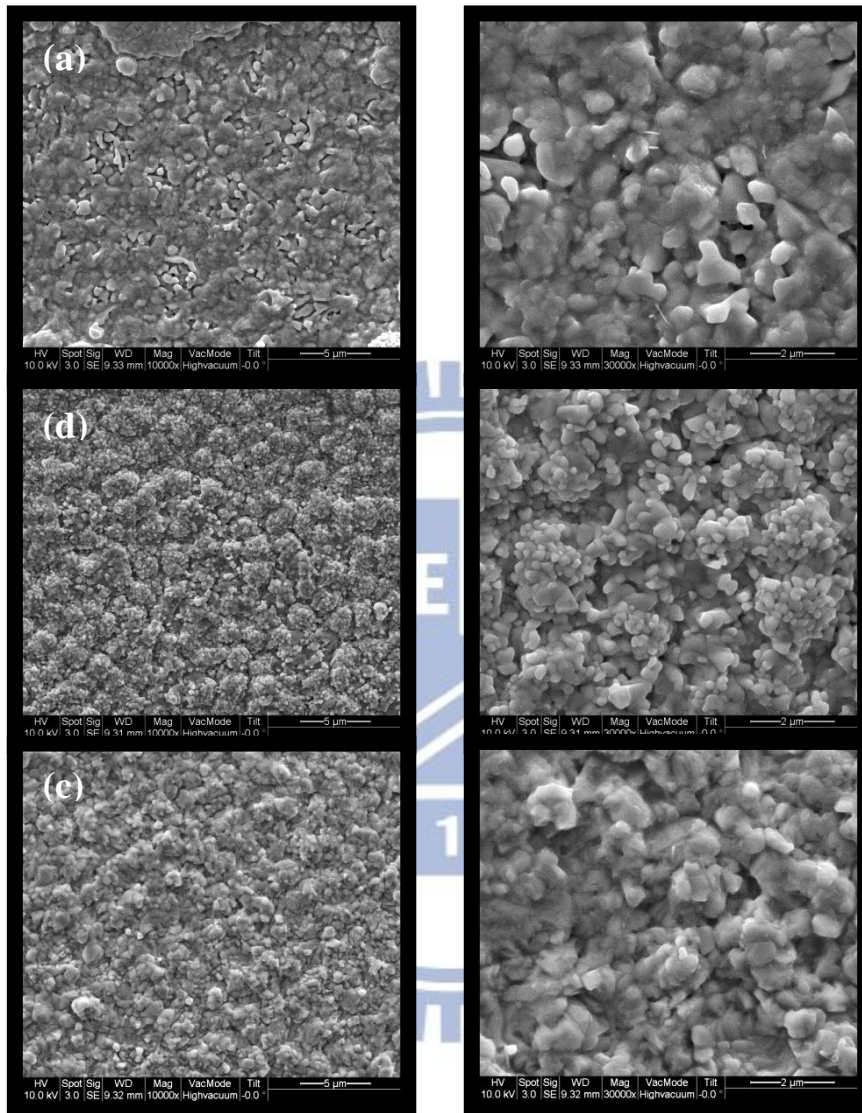


Figure 4-16 SEM top-view images of CIGS thin films prepared with different substrate temperature (a) 45°C (b) 85°C (c) 125°C. (The part of right half was 10K magnification images; the part of left half was 30K magnification images)

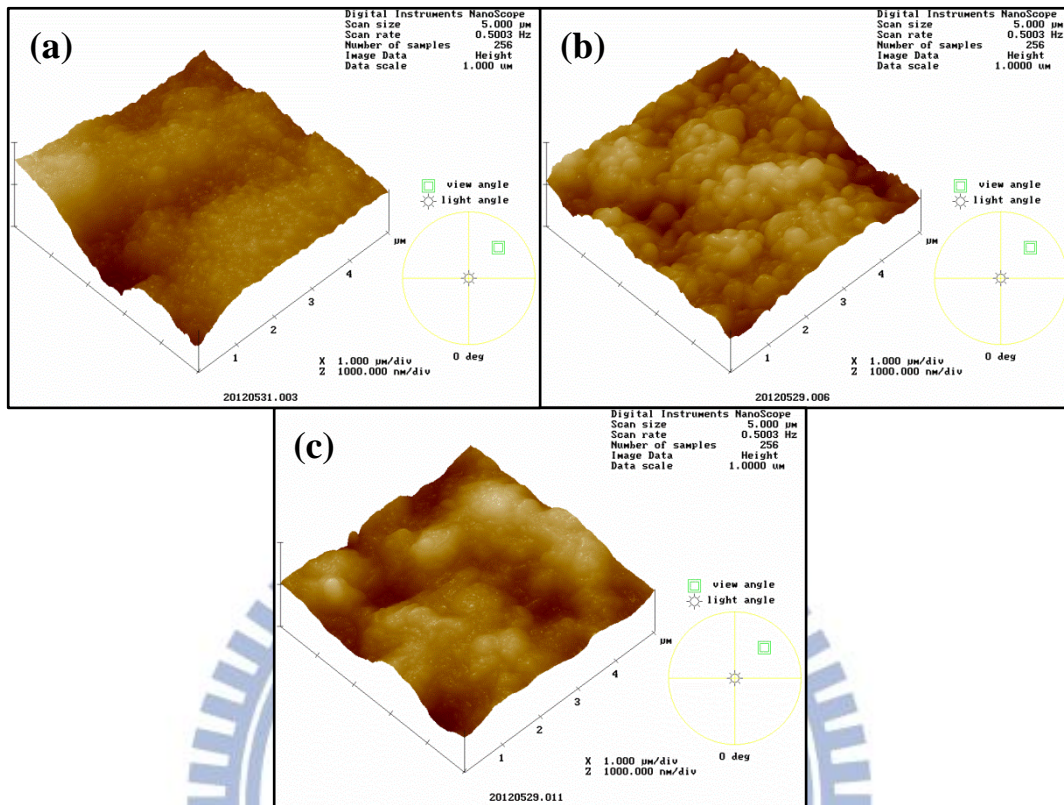


Figure 4-17 AFM images of CIGS thin films prepared with different substrate temperature (a) 45°C (b) 85°C (c) 125°C.

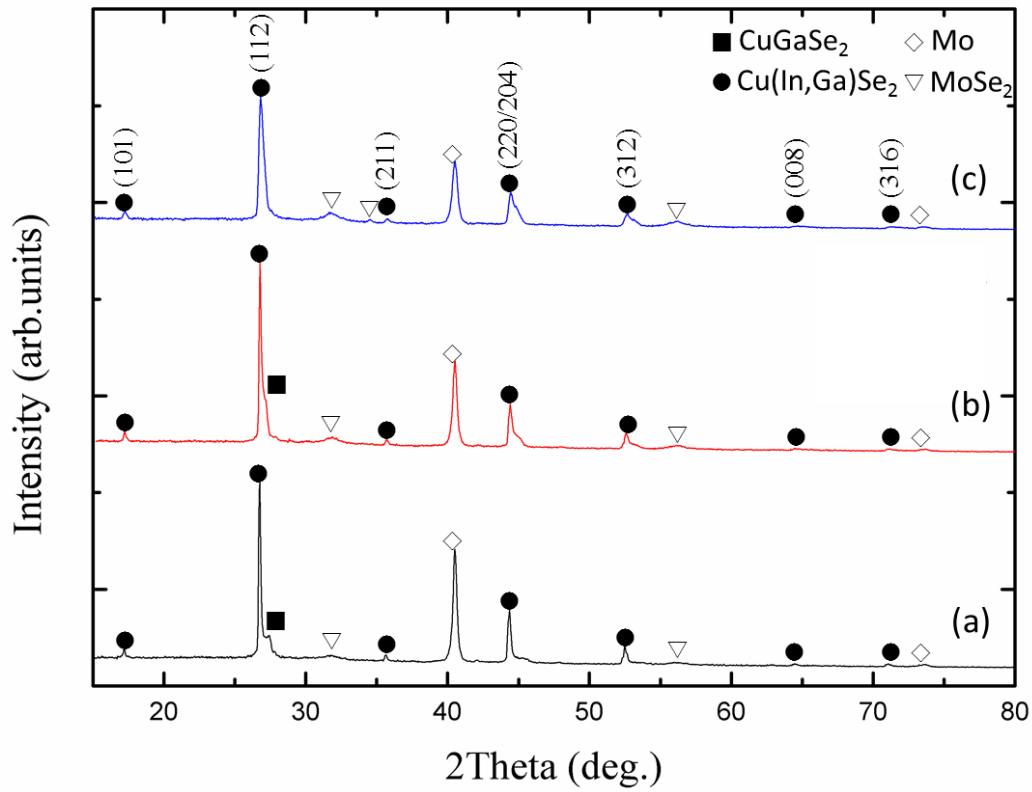


Figure 4-18 GIXRD spectrum of CIGS thin films prepared with different substrate temperature (a) 45°C (b) 85°C (c) 125°C.

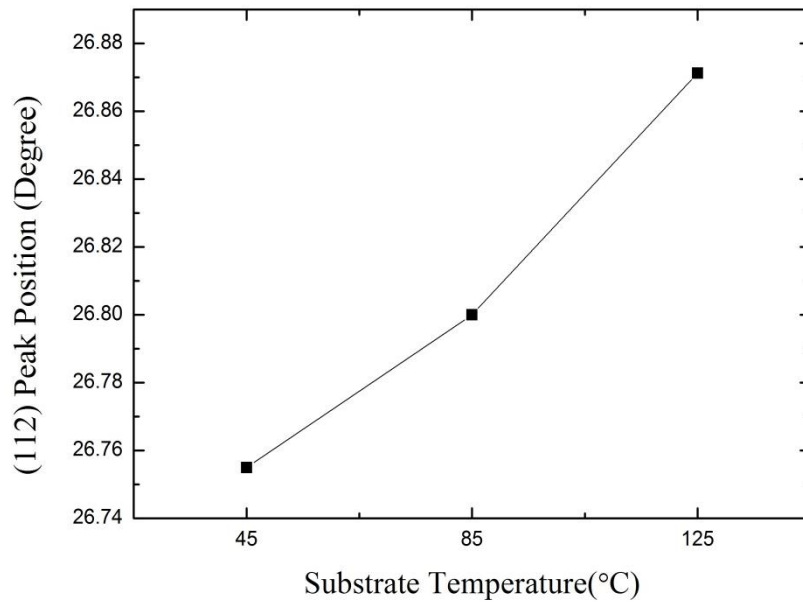


Figure 4-19 Variation of the peak position (2θ) for (112) peak of CIGS thin films with different substrate temperature.

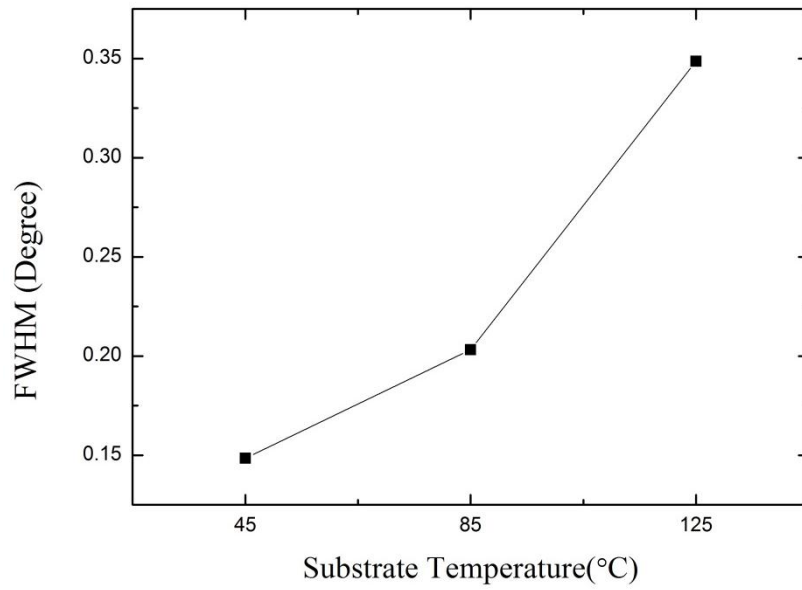
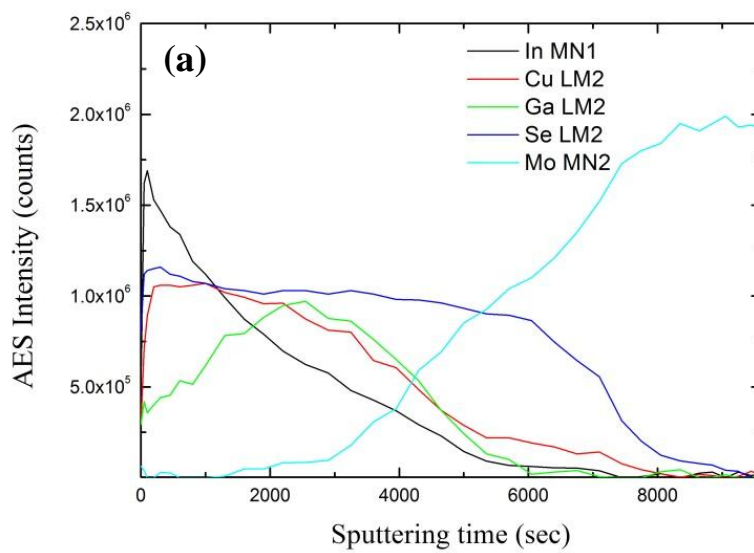
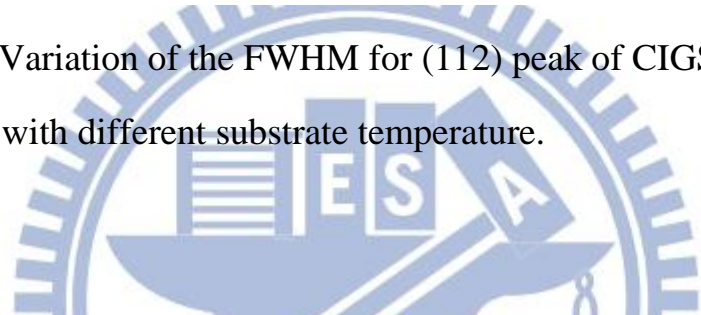


Figure 4-20 Variation of the FWHM for (112) peak of CIGS thin films with different substrate temperature.



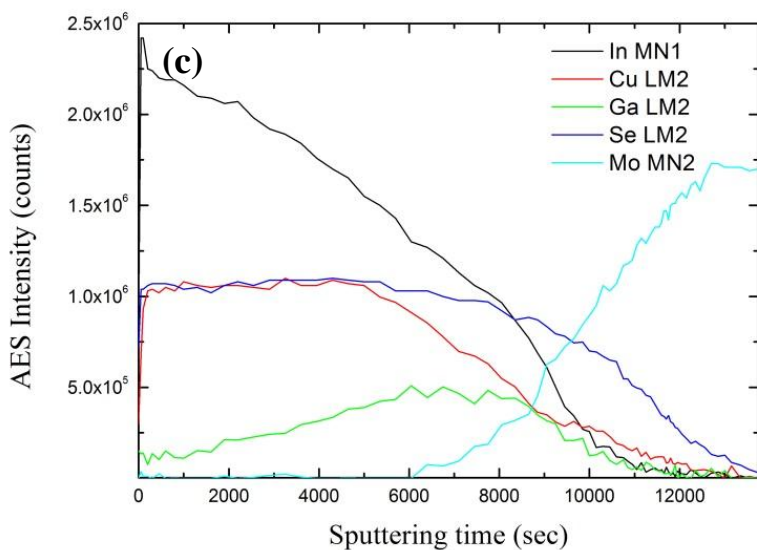
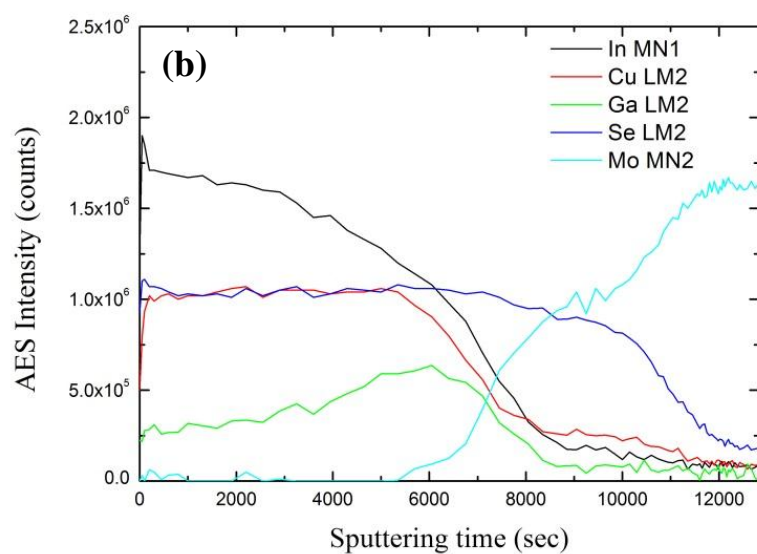


Figure 4-21 Depth analysis of Auger Electron Spectroscopy (AES) prepared with different substrate temperature (a) 45°C (b) 85°C (c) 125°C.

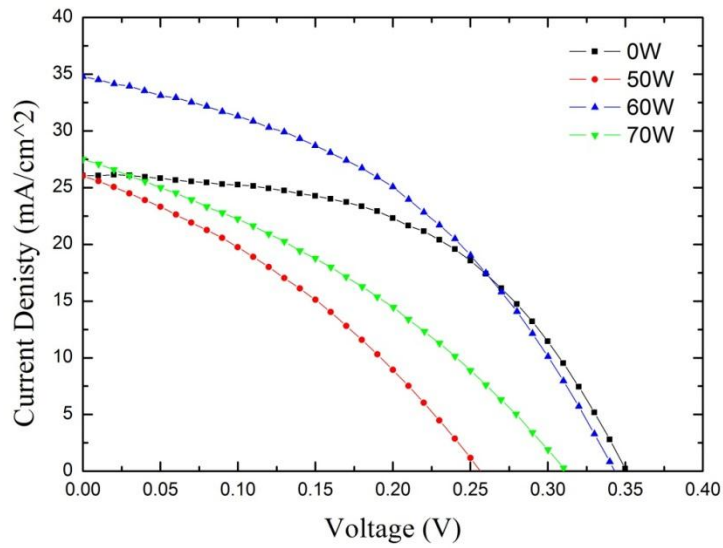


Figure 4-22 I-V curve measurement of the Cu(In,Ga)Se_2 solar cells on the AM1.5G solar simulator prepared with different plasma power (a) without plasma (b) 50W (c) 60W (d) 70W.

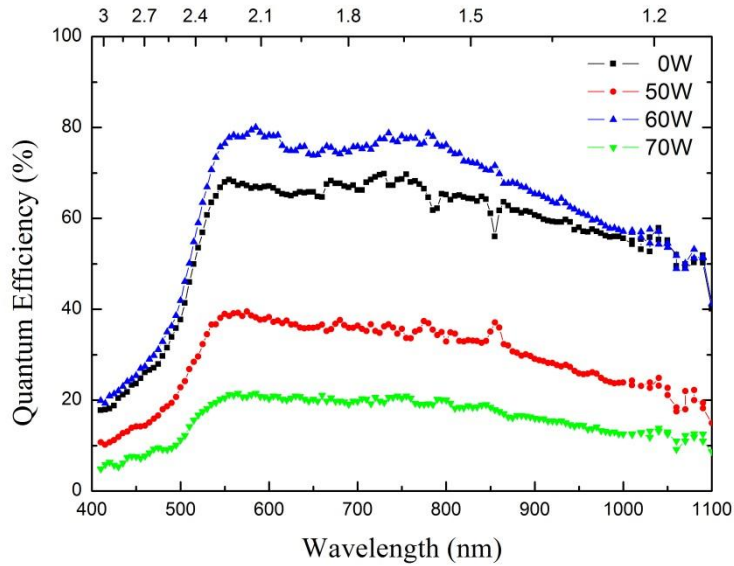


Figure 4-23 Extra quantum efficiency measurement of the Cu(In,Ga)Se_2 solar cells prepared with different plasma power (a) without plasma (b) 50W (c) 60W (d) 70W.

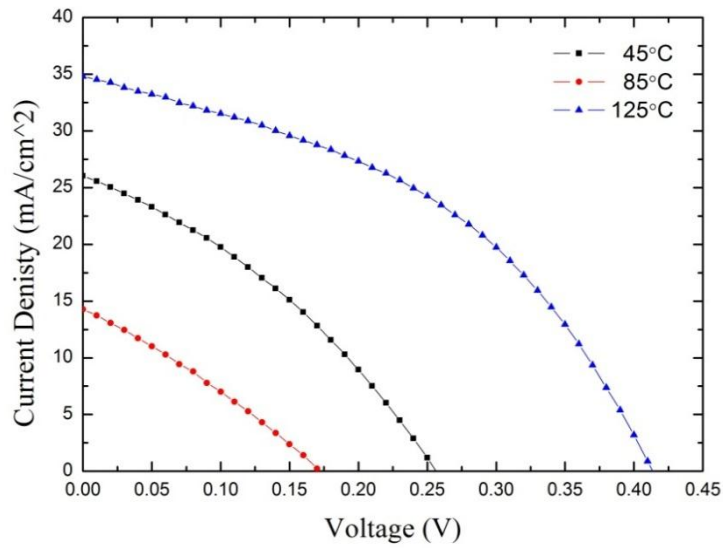


Figure 4-24 I-V curve measurement of the Cu(In,Ga)Se_2 solar cells on the AM1.5G solar simulator prepared with different substrate temperature (a) 45°C (b) 85°C (c) 125°C .

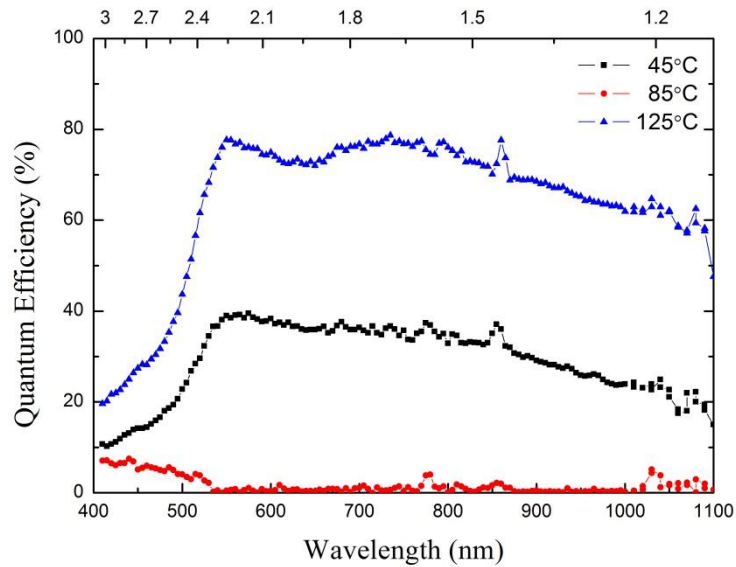


Figure 4-25 Extra quantum efficiency measurement of the Cu(In,Ga)Se_2 solar cells prepared with different substrate temperature (a) 45°C (b) 85°C (c) 125°C .

Table 4-1 Deposition selenium films on the glass without plasma prepared with different Se source temperature (0W 10SLM 550 torr).

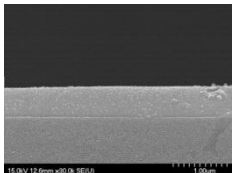
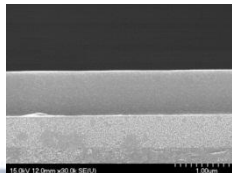
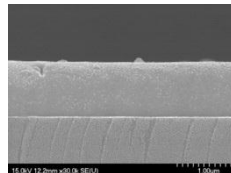
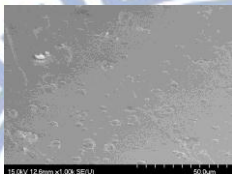
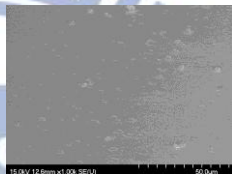
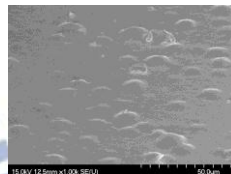
Temperature(°C)	325	335	345
Thickness(nm)	570	840	1030
SEM Cross-section			
SEM Top View			

Table 4-2 Deposition selenium films on the glass without plasma prepared with different main gas flow rate (0W 335°C 550 torr).

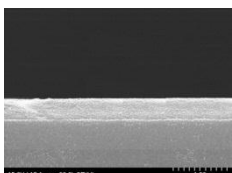
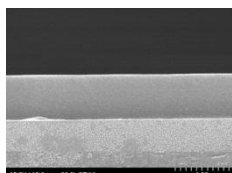
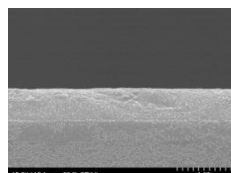
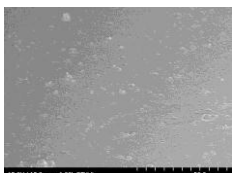
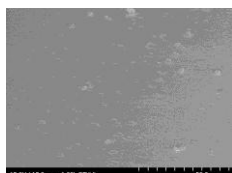

Main gas flow rate (SLM)	5	10	15
Thickness (nm)	510	840	595
SEM Cross-section			
SEM Top View			

Table 4-3 Deposition selenium films on the glass without plasma prepared with different background pressure (0W 335°C 10SLM).

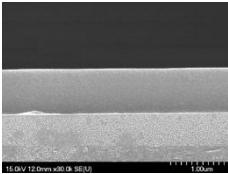
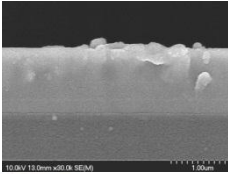
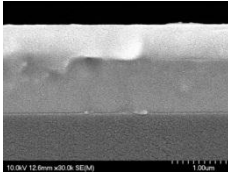
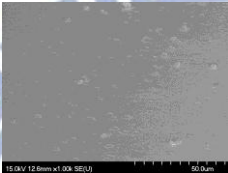
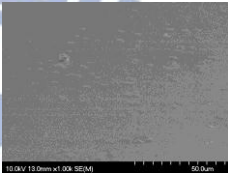
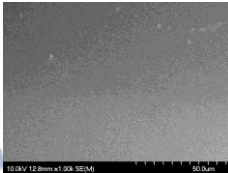
Pressure (torr)	550	350	150
Thickness(nm)	840	1220	1640
SEM Cross-section			
SEM Top View			

Table 4-4 Deposition selenium films on the glass with plasma prepared with different Se source temperature (50W 20SLM 150torr).

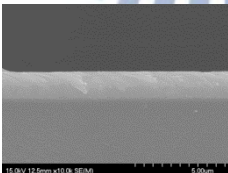
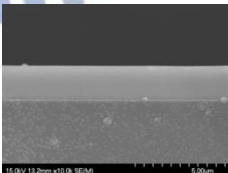
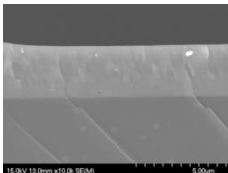
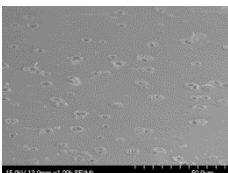
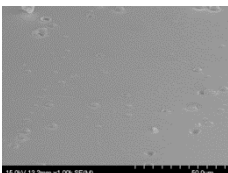
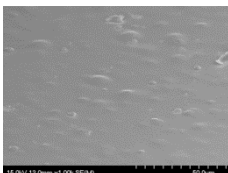
Temperature(°C)	345	355	365
Thickness (μm)	1.55	1.94	2.87
SEM Cross-section			
SEM Top View			

Table 4-5 Deposition selenium films on the glass with plasma prepared with different main gas flow rate (50W 355°C 150torr).

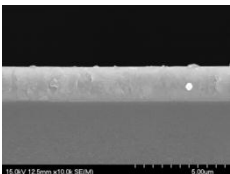
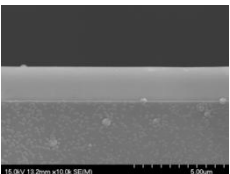
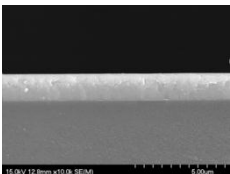
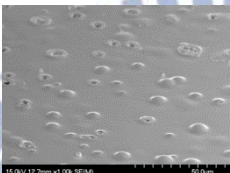
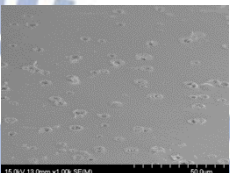
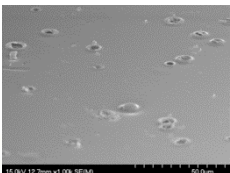
Main gas flow rate (SLM)	15	20	25
Thickness(μm)	1.88	1.94	1.47
SEM Cross-section			
SEM Top View			

Table 4-6 Deposition selenium films on the glass without plasma prepared with different background pressure (50W 355°C 10SLM).

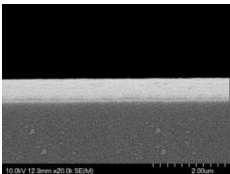
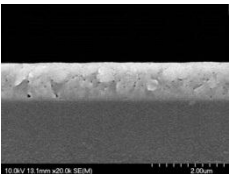
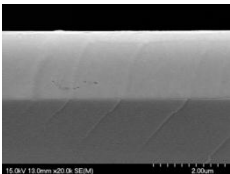

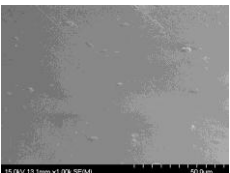
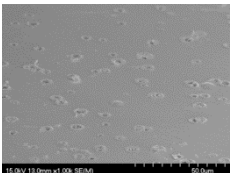
Pressure (torr)	550	350	150
Thickness(μm)	0.58	1.01	1.94
SEM Cross-section			
SEM Top View			

Table 4-7 Deposition selenium films on the glass without plasma prepared with different plasma power (355 °C 10SLM 150torr).

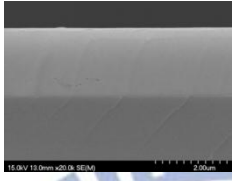
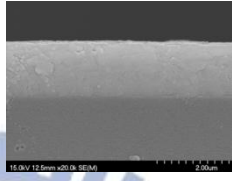
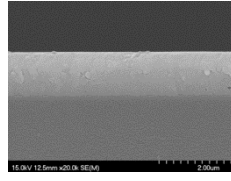
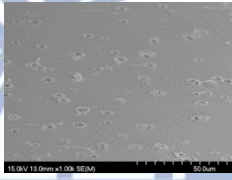
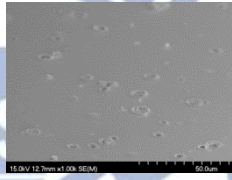
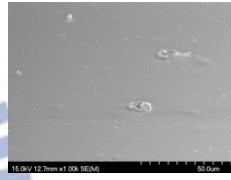
Plasma Power(W)	50W	60W	70W
Thickness(μm)	1.94	1.52	1.22
SEM Cross-section			
SEM Top View			

Table 4-8 Thickness and RMS roughness of deposited selenium on the CIG precursor layer by APPECVD prepared with different plasma power.

Plasma Power	Thickness (nm)	RMS roughness (nm)
0W	2148.89	10.06
50W	2950.00	58.68
60W	3131.26	33.27
70W	2890.91	6.22

Table 4-9 Thickness and RMS roughness of deposited selenium on the CIG precursor layer by APPECVD prepared with different substrate temperature.

Substrate Temperature	Thickness (nm)	RMS roughness (nm)
45°C	2950.00	58.68
85°C	2910.27	244.25
125°C	3181.38	333.28

Table 4-10 Thickness of CIGS/MoSe₂/Mo/Glass sample and RMS roughness of CIGS thin films prepared with different plasma power.

Plasma Power	CIGS absorber layer (nm)	MoSe ₂ (nm)	Mo (nm)	RMS roughness (nm)
0W	1324.27	293.11	229.74	143.26
50W	1491.95	176.92	336.68	209.61
60W	1497.18	303.67	198.05	201.23
70W	1454.81	227.76	231.71	189.59

Table 4-11 EDS results for atomic composition of the selenium thin films prepared with different plasma power.

Plasma Power	Cu	In	Ga	Se	Ga/III	Cu/III
0W	23.87	20.85	6.34	48.94	0.23	0.88
50W	24.25	24.11	5.41	46.23	0.18	0.82
60W	25.30	21.72	5.44	47.54	0.20	0.93
70W	25.25	22.36	5.78	46.61	0.21	0.9

Table 4-12 Thickness of CIGS/MoSe₂/Mo/Glass sample and RMS roughness of CIGS films prepared with different substrate temperature.

Substrate Temperature	CIGS absorber layer (nm)	MoSe ₂ (nm)	Mo (nm)	RMS roughness (nm)
45°C	1491.95	176.92	336.68	209.61
85°C	1383.69	274.63	237.66	130.5
125°C	1263.62	278.51	232.38	120.17

Table 4-13 EDS results for atomic composition of the selenium thin films prepared with different substrate temperature. III: elements of group III.

Substrate Temperature	Cu	In	Ga	Se	Ga/III	Cu/III
45°C	24.25	24.11	5.41	46.23	0.18	0.82
85°C	23.24	23.94	7.33	45.49	0.23	0.74
125°C	25.03	19.01	7.72	48.24	0.29	0.94

Table 4-14 Photovoltaic characteristics of CIGS-based solar cells including six devices fabricated with varied plasma power and substrate temperature. V_{oc} : open-circuit voltage, J_{sc} : short-circuit current, FF: fill factor, R_{shunt} : shunt resistance and R_{series} : series resistance.

Plasma Power	Efficiency (%)	V_{oc} (mV)	J_{sc} (mA/cm ²)	FF (%)	R_{shunt} (Ω/cm^2)	R_{series} (Ω/cm^2)	P_{max} (mW)
0W	4.694	0.35	26.05	51.5	496.79	16.82	2.253
50W	2.266	0.26	26.04	33.5	87.97	26.33	1.088
60W	5.031	0.34	34.8	42.5	162.80	16.92	2.415
70W	2.932	0.31	27.51	34.4	101.16	26.51	1.407
Substrate Temperature	Efficiency (%)	V_{oc} (mV)	J_{sc} (mA/cm ²)	FF (%)	R_{shunt} (Ω/cm^2)	R_{series} (Ω/cm^2)	P_{max} (mW)
45°C	2.266	0.26	26.04	33.5	87.97	26.33	1.088
85°C	0.703	0.17	6.85	30.0	71.55	39.55	1.164
125°C	6.103	0.4	34.82	42.8	163.09	18.23	2.930

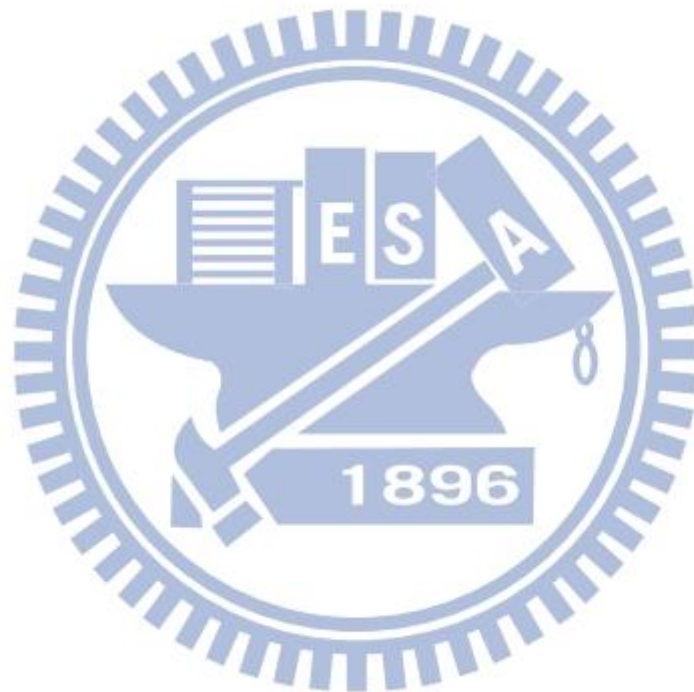
Chapter 5

Conclusions

We have successfully deposited selenium film on the CIG precursor layer by atmospheric pressure plasma, which can enhance chemical vapor deposition.

The selenium films are denser, smoother by APPECVD. The APPECVD contains smaller amount of Se than co-evaporation system. In this thesis, we have used rapid thermal process to selenize the precursor layer, and successfully fabricated the absorber layer of Cu(In,Ga)Se₂ thin films. All films showed a strong preferred (112) orientation and the MoSe₂ layer was found between Cu(In,Ga)Se₂ and Mo. The MoSe₂ not only improved the electric properties but also improved adhesion strength of Cu(In,Ga)Se₂ to Mo. Furthermore, the effect of increased substrate temperature raised band gap of Cu(In,Ga)Se₂ thin films in our research due to different crystallization of selenium thin films. The Ga concentration (Ga/III) of Cu(In,Ga)Se₂ thin film is between 0.2 and 0.3, matching band gap which is between 1.104eV and 1.158eV. The effect of increased plasma power improved the crystallization of chalcopyrite structure of Cu(In,Ga)Se₂ thin films. Those two effects mentioned-above possibly improve the conversion efficiency of solar cell device. Therefore, we complete solar cell, whose structure is Al/ITO/ZnO/CdS/CIGS/Mo/SLG, covering 0.48 cm². The highest conversion efficiencies of solar cell device without plasma and with plasma are respectively 4.694% and 5.031% when the substrate temperature is . The conversion efficiency

of solar cell device with plasma power 50W is 2.266% when the substrate temperature is 45°C. The conversion efficiency of solar cell device with plasma power 50W is 6.103% when the substrate temperature is 125°C, which $FF=0.428$, $V_{oc}=0.41V$ and $J_{sc}=34.815 \text{ mA/cm}^2$. Our study hopefully facilitates to enhance films quality and reduce the costs by APPECVD.



Chapter 6

Future works

In this thesis, some CIGS thin film samples has the CIG separate phase. We can decrease the CIG separate phase result in the region of Ga concentration smaller. Increase the investigation of selenization temperature and time of during process for rapid thermal process. Now, we are limited by the equipment, cannot to sharply increase the plasma power. So the effect of different plasma power is not significant. In the future, we want to do investigation of CIGS thin films by higher plasma power. The scan area will increase to the $10 \cdot 10 \text{cm}^2$ in order to fabricate large area substrate. Additionally, selenium film need to improve the uniform by add the Shower head at the exit of carrier gas. We want to decrease the highest temperature of selenization by APPECVD and in-site selenization because the Se-radical have high chemical potential. But the adjustment of priority is the wire of the equipment, and the wire need to bear high temperature ($>350^\circ\text{C}$) and high voltage. We wish to prepare the CIGS solar cell, which have higher conversion efficiency than this thesis.

References

- [1] W. Shockley, et al., “Detailed Balance Limit of Efficiency of pn Junction Solar Cells,” *Journal of Applied Physics*, vol. 32, pp. 510-519, 1961.
- [2] P. Bermel, et al., “Improving Thin-Film Crystalline Silicon Solar Cell Efficiencies with Photonic,” *Optics express*, vol. 15, pp. 16986-17000, 2007.
- [3] E. Alsema, et al., “Energy Requirements of Thin-Film Solar Cell Modules – a review,” *Renewable and Sustainable Energy Reviews*, vol. 2, pp. 387-415, 1998.
- [4] M. A. Contreras, et al., “Progress Toward 20% Efficiency in Cu(In,Ga)Se₂ Polycrystalline Thin-Film Solar Cells,” *Progress in Photovoltaics: Research and Applications*, vol. 7, pp. 311-316, 1999.
- [5] T. Negami, et al., “Cu(In,Ga)Se₂ Thin-Film Solar Cells with an Efficiency of 18%,” *Solar energy Materials & Solar Cells*, vol. 67, pp. 331-335, 2001.
- [6] H. S. Ullal, et al., “Polycrystalline Thin-Film Photovoltaic: Research, Development, and Technologies,” *Proceedings of the 29th IEEE Photovoltaic Specialists Conference*, pp.472-477, 2002.
- [7] NREL, “Konarka Power Plastic Reaches 8.3% Efficiency,” *pv-tech.org*, 2011.
- [8] F. Kang, et al., “Structure and photovoltaic characteristics of CuInSe₂ thin films prepared by pulse-reverse electro-deposition and

- selenization process,” *Journal of Alloys and Compounds*, vol. 478, pp. L25-L27, 2009.
- [9] Y. Hamakawa, et al., “Thin Film Solar Cells: Next Generation Photovoltaics and Its Applications,” 2004.
- [10] S. Chen, et al., “Band-structure anomalies of the chalcopyrite semiconductors CuGaX_2 versus AgGaX_2 ($\text{X}=\text{S}$ and Se) and their alloys,” *Physical Review B*, vol. 75, pp. 205-209, 2007.
- [11] D. K. Suri, et al., “X-ray study of $\text{CuGa}_x\text{In}_{1-x}\text{Se}_2$ solid solutions,” *Journal of Applied Crystallography*, vol. 22, pp. 578-583, 1989.
- [12] T. F. Ciszek, et al., “Growth and properties of CuInSe_2 crystals produced by chemical vapor transport with iodine,” *Journal of Crystal Growth*, vol. 70, pp. 405-410, 1984.
- [13] H. Neumann, et al., “Optical properties and electronic band structure of CuInSe_2 ,” *Solar Cells*, vol. 16, pp. 317-333, 1986.
- [14] S. M. Wasim, et al., “Transport properties of CuInSe_2 ,” *Solar Cells*, vol. 16, pp. 289-316, 1986.
- [15] R. Herberholz, et al., “Phase segregation, Cu migration and junction formation in $\text{Cu}(\text{In,Ga})\text{Se}_2$,” *The European Physical Journal Applied Physics*, vol. 6, pp. 131-139, 1999.
- [16] D. Schmid, et al., “A comprehensive characterization of the interfaces in Mo/CIS/CdS/ZnO solar cell structures,” *Solar energy materials and solar cells*, vol. 41-42, pp. 281-294, 1996.
- [17] S. H. Wei, et al., “Effects of Na on the electrical and structural properties of CuInSe_2 ,” *Journal of applied physics*, vol. 85, pp. 7214-7218, 1999.

- [18] C. Rincon, et al., "Defect physics of the CuInSe₂ chalcopyrite semiconductor," *Journal of Physics and Chemistry of Solids*, vol. 60, pp. 1865-1873, 1999.
- [19] I. Repins, et al., "19.9%-efficient ZnO/CdS/CuInGaSe₂ Solar Cell with 81.2% Fill Factor," *Progress in Photovoltaics: Research and Applications*, vol. 16, pp. 235-239, 2008.
- [20] N.A.K. Abdul-Hussein, et al., "Electrical Properties of RF Sputtered Thin Films of CuInSe₂ (I)," *Crystal Research and Crystal Technology*, vol. 20, pp. 509-514, 1985.
- [21] F. R. White, et al., "Growth of CuInSe₂ on CdS using Molecular Beam Epitaxy," *Journal of Applied Physics*, vol. 50, pp. 544-545, 1979.
- [22] S. H. Yoon, et al., "Preparation of CuInSe₂ Thin-Films through Metal Organic Chemical Vapor Deposition Method by using Di- μ -Methylselenobis and Bis Copper(II) Precursors," *Thin Solid Films*, vol. 515, pp. 1544-1547, 2006.
- [23] A. A. Akl, et al., "Growth, Microstructure, Optical and Electrical Properties of Sprayed CuInSe₂ Polycrystalline Films," *Materials Research Bulletin*, vol. 43, pp. 1539-1548, 2008.
- [24] J. F. Guillemoles, et al., "Recrystallization of Electrodeposited Copper Indium Di-Selenide Thin-Films in an Atmosphere of Elemental Selenium," *Advanced Materials*, vol. 6, pp. 376-379, 1994.
- [25] M. Kaelin, et al., "Low-cost CIGS solar cells by paste coating and selenization," *Thin Solid Films*, vol. 480, pp. 486-490, 2005.

- [26] M. Kaelin, et al., "CIS and CIGS layers from selenized nanoparticle precursors," *Thin Solid Films*, vol. 432, pp. 58-62, 2003.
- [27] R. A. Mickelsen, et al., "Development of a 9.4% efficient thin-film CuInSe₂/CdS solar cell," *Proceeding of the 15th IEEE Photovoltaic Specialists Conference*, pp. 800-804, 1981.
- [28] A. M. Gabor, et al., "High efficiency CuIn_xGa_{1-x}Se₂ solar cells made from (In_xGa_{1-x})₂Se₃ precursor films," *Applied Physics Letters*, vol. 65, pp. 198-200, 1981.
- [29] M. Kaelin, et al., "Low cost processing of CIGS thin film solar cells," *Solar Energy*, vol. 77, pp. 749-756, 2004.
- [30] R. Gay, et al., "Efficiency and process improvements in CuInSe₂-based modules," *Proceedings of the International Conference on E.C. Photovoltaic Solar Energy*, vol. 12, pp. 749-756, 2004.
- [31] R. Caballero, et al., "CuIn_{1-x}Ga_xSe₂-based thin-film solar cells by the selenization of sequentially evaporated metallic layers," *Progress in Photovoltaics: Research and Applications*, vol. 14, pp. 145-153, 2006.
- [32] S. D. Kim, et al., "Effect of selenization pressure on CuInSe₂ thin films selenized using co-sputtered Cu-In precursors," *Solar Energy Materials and Solar Cells*, vol. 62, pp. 357-368, 2000.
- [33] C. Guillen, et al., "Effect of Semiconductor CuInSe₂ formation by close-spaced selenization processes in vacuum," *Vacuum*, vol. 67, pp. 659-664, 2002.
- [34] R. Caballero, et al., "CuInSe₂ Formation by selenization of

- sequentially evaporated metallic layers,” *Solar Energy Materials and Solar Cells*, vol. 86, pp. 1-10, 2005.
- [35] V. F. Gremenok, et al., “Preparation of Cu(In,Ga)Se₂ thin film solar cells by two-stage selenization processes using N₂ gas,” *Solar Energy Materials and Solar Cells*, vol. 89, pp. 129-137, 2005.
- [36] S. R. Kodigala, et al., “Cu(In_{1-x} Ga_x)Se₂ Based Thin Film Solar Cells”.
- [37] “Selenium and selenium compounds,” Kirk-Othmer Encyclopedia of Chemical Technology.
- [38] S. T. Lakshmikumar, et al., “Plasma assisted two stage selenization process for the preparation of selenide semiconductor thin films using elemental selenium vapor,” *Journal of Applied physics*, vol. 76, pp. 3068-3071, 1994.
- [39] I. Repins, et al., “Plasma-Assisted Co-evaporation of S and Se for Wide Band Gap Chalcopyrite Photovoltaics,” *National Renewable Energy Laboratory*, 2005.
- [40] S. Ishizuka, et al., “Growth of polycrystalline Cu(In,Ga)Se₂ thin films using a radio frequency-cracked Se-radical beam source and application for photovoltaic devices,” *Applied Physics Letters*, vol. 91, 041902-041904, 2007.
- [41] S. Ishizuka, et al., “CIGS thin films, solar cells, and submodules fabricated using a RF-plasma cracked Se-radical beam source,” *Thin Solid Films*, vol. 519, pp. 7216-7220, 2011.
- [42] M. A. Contreras, et al., “Diode Characteristics in State-of-the-Art ZnO/CdS/Cu(In_{1-x}Ga_x)Se₂ Solar Cells,” *Progress in Photovoltaics:*

- Research and Applications*, vol. 13, pp. 209-216, 2005.
- [43] G. S. Chen, et al., "Another route to fabricate single-phase chalcogenides by post-selenization of Cu–In–Ga precursors sputter deposited from a single ternary target," *Solar Energy Materials & Solar Cells*, vol. 93, pp. 1351-1355, 2009.
- [44] H. R. Hsu, et al., "Improvement of Ga distribution and enhancement of grain growth of CuInGaSe₂ by incorporating a thin CuGa layer on the single CuInGa precursor," *Solar Energy*, vol. 8, pp. 48-52, 2012.
- [45] X. Donglin, et al., "Electrodeposited and selenized CIGS thin films for solar cells," *Journal of Non-Crystalline Solids*, vol. 354, pp. 1447-1450, 2008.
- [46] A. Rockett, et al., "Cu(In,Ga)(S,Se)₂ Crystal Growth, Structure, and Properties".
- [47] Speed Tech, Home page, All production, Interface parts, Sputtering Application.
- [48] Wikipedia, Home page, Copper indium gallium selenide solar cells, Electro-deposition followed by selenization.
- [49] D. Kopeliovich, et al., Plasma arc welding, SubsTech, 2009.
- [50] Apjet, Textile Applications, Key Concepts, 2004.
- [51] TFOT, Home, Articles, Computer Technology, Ionic Wind-Chillin' the PC, 2007.
- [52] J. S. Chang, et al., "Corona Discharge Processes," *IEEE Transactions on Plasma Science*, vol. 19, pp. 1152-1166, 1991.
- [53] N. Esser, et al., "Optical Characterization of Epitaxial Semiconductor Layers," *Springer*, Chapter 4, 1996.

- [54] T. Riedel, et al., Technical University, Berlin, Ph.D. Thesis, 1992.
- [55] Northern Arizona University, home page, Planetary Materials Microanalysis Facility, Scanning Electron Microscope Laboratory.
- [56] Paul Hansma Research Group, home page, Instrument, AFM introduction.
- [57] Integration Research and Education, home page, Geochemical Instrumentation and Analysis, X-ray Crystallography, Single-crystal X-ray Diffraction.
- [58] D. W. Hamby, et al., "Investigation of Subsurface Damage of II-VI Semiconductors Using Photoluminescence".
- [59] G. S. Chen, et al., "Another route to fabricate single-phase chalcogenides by post-selenization of Cu-In-Ga precursors sputter deposited from a single ternary target," *Solar Energy Materials & Solar Cells*, vol. 93, pp. 1351-1355, 2009.
- [60] G. M. Hanket, et al., "Incongruent reaction of Cu-(InGa) intermetallic precursors in H₂Se and H₂S," *Journal of Applied Physics*, vol. 102, pp. 074922-074931, 2007.
- [61] R. Kamada, et al., "Control of Composition in Co-evaporated Cu(InGa)(SeS)₂ Thin Films," *Photovoltaic Specialists Conference, 2008. PVSC '08. 33rd IEEE*, pp. 1-4, 2008.
- [62] S.P. Sen Gupta, et al., "Amorphous to crystalline phase transition of vapour grown selenium films," *Journal of Materials Science Letters*, vol. 5, pp. 559-561, 1986.
- [63] T. Wada, et al., "Characterization of the Cu(In,Ga)Se₂/Mo interface in CIGS solar cells," *Thin Solid Films*, vol. 387, pp. 118-122, 2001.

- [64] H. Park, et al., “Effect of precursor structure on Cu(In,Ga)Se_2 formation by reactive annealing,” *Thin Solid Films*, vol. 519, pp. 7245-7249, 2011.

